Project No. 12-3809

Alternative High-Performance Ceramic Waste Forms

Fuel Cycle Research and Development

S.K. Sundaram
Alfred University

Kimberly Gray, Federal POC
John Vienna, Technical POC

NEUP Nuclear Energy University Programs
U.S. Department of Energy

Alternative High-Performance Ceramic Waste Forms - Final Report

M2NU-12-NY-AU # 0202-0410

S. K. Sundaram, B. M. Clark, P. Tumurugoti, and S. T. Misture
Kazuo Inamori School of Engineering
The New York State College of Ceramics
Alfred University, Alfred, NY 14802
J. W. Amoroso and J. C. Marra
Savannah River National Laboratory
Aiken, SC 29808
M. Tang
Los Alamos National Laboratory
Los Alamos, NM 87545

December 15, 2016

Alfred University
Alfred, NY 14802

SUMMARY

This final report (M5NU-12-NY-AU # 0202-0410) summarizes the results of the project titled "Alternative High-Performance Ceramic Waste Forms," funded in FY12 by the Nuclear Energy University Program (NEUP Project # 12-3809) being led by Alfred University in collaboration with Savannah River National Laboratory (SRNL). The overall focus of the project is to advance fundamental understanding of crystalline ceramic waste forms and to demonstrate their viability as alternative waste forms to borosilicate glasses.

We processed single- and multiphase hollandite waste forms based on simulated waste streams compositions provided by SRNL based on the advanced fuel cycle initiative (AFCI) aqueous separation process developed in the Fuel Cycle Research and Development (FCR&D). For multiphase simulated waste forms, oxide and carbonate precursors were mixed together via ball milling with deionized water using zirconia media in a polyethylene jar for 2 h. The slurry was dried overnight and then separated from the media. The blended powders were then subjected to melting or spark plasma sintering (SPS) processes. Microstructural evolution and phase assemblages of these samples were studied using x-ray diffraction (XRD), scanning electron microscopy (SEM), energy dispersion analysis of x-rays (EDAX), wavelength dispersive spectrometry (WDS), transmission electron spectroscopy (TEM), selective area x-ray diffraction (SAXD), and electron backscatter diffraction (EBSD). These results showed that the processing methods have significant effect on the microstructure and thus the performance of these waste forms.

The Ce substitution into zirconolite and pyrochlore materials was investigated using a combination of experimental (in situ XRD and x-ray absorption near edge structure (XANES)) and modeling techniques to study these single phases independently. In zirconolite materials, a transition from the 2M to the 4M polymorph was observed with increasing Ce content. The resulting powders were consolidated via SPS. Ce was reduced to the trivalent oxidation state and the zirconolite was converted into undesirable perovskite. The zirconolite polymorphs found in the synthesized powders were recovered after a post-SPS heat treatment in air. These results demonstrated the potential of processing in controlling the phase assemblage in these waste forms.

Hollandites with Cr^{3+} trivalent cations were identified as potential hosts for Cs immobilization and are being investigated for Cs retention properties. Series of compositions $Ba_{1.15-x}Cs_{2x}Cr_{2.3}Ti_{5.7}O_{16}$, with increasing Cs loadings, were prepared by sol-gel process and characterized for structural parameters. Structural characterization was performed by a combination of powder XRD and neutron powder diffraction. Phase pure hollandite adapting monoclinic symmetry (I2/m) was observed for $0 \leq x \leq 0.55$. These results were used to develop a new structural model to interpret Cs immobilization in these hollandites.

Performance of these waste forms were evaluated for chemical durability and radiation resistance. Product consistency testing (PCT) and vapor hydration testing (VHT) were used for testing of chemical durability. Radiation resistance was tested using He^{+} ions to simulate α particles and heavy ions such as Au^{3+} to simulate α recoil. These results showed that these waste forms were chemically durable. The waste forms also amorphized to various degrees on exposure to simulated radiation.

TABLE OF CONTENTS

LIST OF FIGURES

LIST OF TABLES

ABBREVIATIONS

ADP	Anisotropic Displacement Parameters
AFCI	Advanced Fuel Cycle Initiative
AU	Alfred University
BSE	Backscatter Electron
CS	Cesium/Strontium
CHESS	Cornell High Energy Synchrotron Source
DOE	Department of Energy
DSC	Differential Scanning Calorimetry
DTA	Differential Thermal Analysis
DWF	Designer Waste Forms
EBSD	Electron Backscatter Diffraction
EBSP	Electron Backscatter Pattern
EDAX	Energy Dispersive X-ray Spectroscopy
EDS	Energy Dispersive Spectroscopy
EMSL	Environmental Molecular Sciences Laboratory
EPMA	Electron Probe Microanalysis
EXAFS	Extended X-Ray Absorption Fine Structure
FCR&D	Fuel Cycle Research and Development
FIB	Focused Ion Beam
GIXRD	Grazing Incidence X-ray Diffraction
GULP	General Utility Lattice Program
HDPE	High Density Polyethylene
HHC	Hollandite High Cesium
HLC	Hollandite Low Cesium
HLW	High Level Waste
HTXRD	High Temperature X-ray Diffraction
IBL	Ion Beam Laboratory
IBML	Ion Beam Materials Laboratory
ICP	Inductively Coupled Plasma
LANL	Los Alamos National Laboratory
LN	Lanthanides

MCC	Materials Characterization Center
NEC	National Electrostatics Corporation
NEUP	Nuclear Energy University Program
NM	Noble Metals
NPD	Neutron Powder Diffraction
PNNL	Pacific Northwest National Laboratory
PCT	Product Consistency Test
REE	Rare-earth Elements
SAED	Selected Area Electron Diffraction
SEM	Scanning Electron Microscopy
SPS	Spark Plasma Sintering
SRIM	Stopping and Range of Ions in Matter
SRNL	Savannah River National Laboratory
SYNROC	Titanium based ceramic substance that can incorporate nuclear waste
TEM	Transmission Electron Microscopy
TGA	Thermogravimetric Analysis
TM	Transition Metals
VHT	Vapor Hydration Test
WDS	Wavelength Dispersive Spectroscopy
XANES	X-ray Absorption Near Edge Spectroscopy
XPS	X-ray Photoelectron Spectroscopy
XRD	X-ray Diffraction

ACKNOWLEDGEMENTS

The authors would thank the Department of Energy's Nuclear Energy University Program (NEUP) for supporting this project. We acknowledge guidelines and feedbacks provided by Dr. J. D. Vienna, Pacific Northwest National Laboratory (PNNL), Richland, WA. We also acknowledge the time and support of Drs. V. Shutthanandan and S. Thevuthasan of Environmental Molecular Sciences Laboratory (EMSL) and Drs. D. Edwards and C. Henager, Jr. of PNNL during the summer of 2014. We appreciate time and support of Dr. J. W. Amoroso and Phyllis Workman of Savannah River National Laboratory (SRNL), Aiken, SC during our visit to SRNL in the summer of 2015. We thank Dr. Ming Tang of Los Alamos National Laboratory (LANL), Los Alamos, NM for his inputs on manuscript preparation of irradiated samples and transmission electron microscopy (TEM) interpretation. The time and effort of Dr. R. Huang of the Cornell High Energy Synchrotron Source (CHESS) is greatly appreciated. Professor S. K. Sundaram is grateful to the generous support of Inamori Professorship by Kyocera Corporation. BMC acknowledges the support of the NEUP Graduate Fellowship.

Alternative High-Performance Ceramic Waste Forms

- Final Report M2NU-12-NY-AU # 0202-0410

December 15, 2016

1) Introduction and Selection of Compositional Space (Task 1)

The Department of Energy (DOE)'s Nuclear Energy University Program (NEUP) funded a team led by Alfred University (AU) in collaboration with Savannah River National Laboratory (SRNL) in FY12 to develop multi-phase ceramic waste forms. The overall focus of the project (NEUP Project # 12-3809) is to advance fundamental understanding of crystalline ceramic waste forms and to demonstrate their viability as alternative waste forms to borosilicate glasses. Major scientific and technical objectives of the proposed project are to: 1) Study phase assemblage and equilibrium in select ceramic waste form compositions for combined cesium/strontium/lanthanides/transition metals (CS/LN/TM) with high Mo waste streams, 2) Evaluate melt and sintering processes to produce dense microstructures, which are critical to durability, performance and the phase formation and distribution of phases and dopants, 3) Characterize the structure and chemical durability of the ceramic waste forms, 4) Establish crystallization kinetics and mechanisms in the waste forms, specifically as a function of processing method, and 5) Design and demonstrate a multi-phase ceramic waste form with performance superior to baseline borosilicate glasses. The project is structured around six technical tasks: 1) Selection of the compositional space, 2) Preparation and fabrication of waste forms, 3) Characterization of waste forms, 4) Nucleation and growth studies, 5) Development of structure-property relationships, and 6) Testing and validation of the waste form(s). This final report summarizes the results completed under this project.

The use of nuclear energy to generate electricity or produce weapons necessitates methods to immobilize wastes generated from those processes. Several thermal as well as non-thermal processes have been used for this purpose. These processes consist of, but are not limited to, vitrification [1], hot isostatic pressing [2], melt formation [3] spark plasma sintering (SPS) [2], and cementation [4]. Titanate-based ceramic waste forms specifically SYNROC [5] and derivative materials have been widely studied for their potential to accommodate a large variety of radionuclides. The major phases targeted in SYNROC compositions are zirconolite ($CaZrTi_2O_7$), hollandite ($Ba_xCs_yAl_{2x+y}Ti_{8-2x-y}O_{16}$), perovskite ($CaTiO_3$), and pyrochlore ($A_2B_2O_7$, where A and B are different 3+ or 4+ cations). Zirconolite and perovskite/pyrochlore are targeted to immobilize most actinides, while fission products (Cs and Sr) are immobilized in hollandite phases.

1.1 Past Work

Past work performed at SRNL to develop crystalline ceramic waste forms with the ultimate goal of future melter demonstration testing for the crystalline ceramic waste forms are summarized in FY10, 11, and 12 reports [6]. Successful demonstration of melt processing of ceramic waste forms achieving the targeted phases has been accomplished, however there were additional crystalline phases observed that possessed low durability, specifically the alkali molybdates Cs-Mo type phases. The SRNL team focused on refinements of composition and processing tailored towards Cs incorporation into the hollandite structure and minimization of secondary Cs-Mo phase formation by varying the transition metal elements in the hollandite structure [7] to facilitate Cs incorporation and continued processing in reducing conditions using metal/metal oxide buffers such as Ti/TiO_2 [8]. It was recommended that processing should be performed in a reducing environment to avoid Cs-Mo oxide formation. Table 1-1 shows the reference ceramic composition. Figure 1-1 shows the scanning electron microscopy (SEM) image of the reference waste form (CW-AFHZ) melted at 1500°C for 20 minutes in a 1%H_2 balance argon gas atmosphere. Iron oxide (5.82 wt %) was used as the baseline additive targeting improved hollandite formation. The local

composition of phases determined by x-ray diffraction (XRD) and energy-dispersive x-ray spectroscopy (EDAX) is summarized in Table 1-2. The targeted hollandite, perovskite, and zirconolite phases were observed along with alumina, powellite, and a Cs-Mo phase.

Table 1-1. Reference ceramic composition (wt. %) for CSLNTM-high Mo waste streams. *Fe or multivalent transition metal (Co, Zn, Cr) to assist hollandite formation [7, 9]

Composition	wt. %	Targeted Phase
Waste	23.74	
Al_2O_3	6.62	*Hollandite*
TiO_2	51.03	*Hollandite, Perovskite, Zirconolite*
CaO	1.36	*Zirconolite*
BaO	11.43	*Hollandite*
*Fe_2O_3	5.82	*Hollandite*

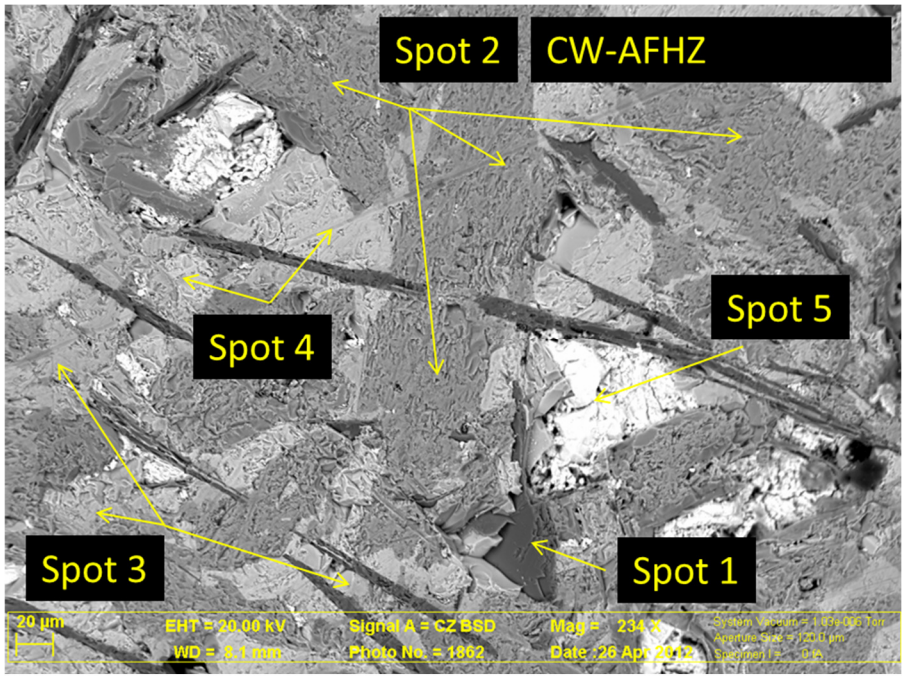

Figure 1-1. CW-AFHZ fabricated by a melting and crystallizing in a 1%H_2 balance Argon- Backscattered Electron Micrograph

Table 1-2. CW-AFHZ fabricated by melting and crystallizing in 1%H2 balance Argon-Summary of elements and crystalline phases (*Crystalline phases determined from XRD measurements and EDAX elemental analysis)

Spot	Elements (Major, Minor)	Crystalline Phases*
1	O, Al	Al_2O_3
2	O, Ti, Al, Ba	Hollandite- $BaAlTi_5O_{14}$
3	O, Ti, Zr, Ca	Zirconolite-$CaZrTi_2O_7$
4	O, Ti, Ca, Nd	Perovskite- Nd doped $CaTiO_3$
5	O, Cs, Mo, Ca, Ba	Cs_2MoO_4 + $(BaCa)MoO_4$

1.2 Hollandites

Original interest in the BaO-TiO_2-Al_2O_3 system emerged out of concern about the harmful effects of Al_2O_3 addition on the dielectric and ferroelectric properties of $BaTiO_3$ [10]. This led to discovery of several new compounds in this system, including barium hollandite, $BaAl_2Ti_5O_{14}$, one of the three major phases in the SYNROC a synthetic rock proposed as a waste form of nuclear waste disposal [5c]. Other phases identified were perovskite ($CaTiO_3$) and zirconolite ($CaZrTi_2O_7$). Figure 1-2 shows the subsolidus phase diagram of the system and Table 1-3, the summary of the structural data of these three phases.

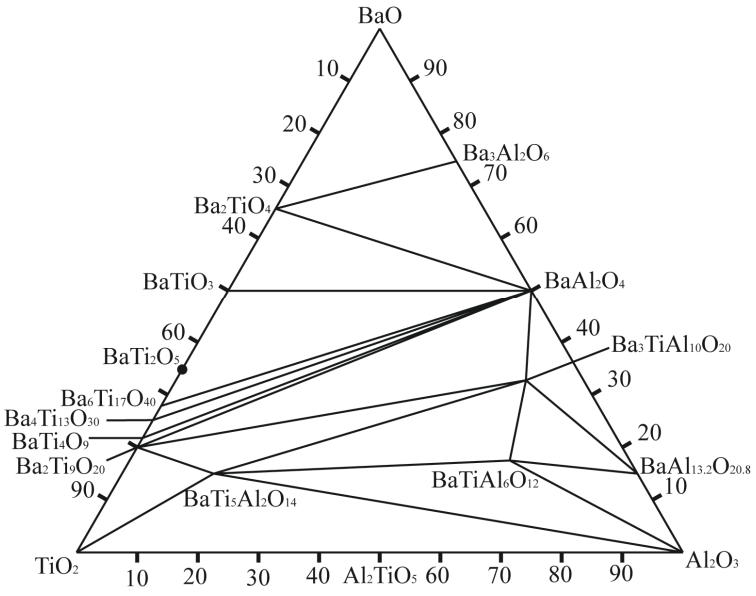

Figure 1-2. Subsolidus equilibria in the system BaO-TiO_2-Al_2O_3 at 1200°C [10]

Table 1-3. X-ray crystallographic data for barium titanium aluminates [10]

	$BaTi_5Al_2O_{14}$	**$BaTiAl_6O_{12}$**	**$Ba_3TiAl_{10}O_{20}$**
Symmetry	Tetragonal	Tetragonal	Orthorhombic
Unit Cell (Å)	a = 7.025	a = 10.070	a = 14.854
	c = 10.156	c = 9.107	b = 11.365
			c = 4.986
Cell content (z)	2	4	2
Density (g/cm^3) Expt.	4.32	3.84	4.13
Calc.	4.34	3.87	4.14

Early nuclear irradiation study of barium hollandite phase showed defect formation and volume expansion [11]. Cesium (Cs) incorporation into SYNROC was studied due to large Cs concentration in the waste streams and high mobility of cesium ions under leaching conditions. XRD data [12] showed that the limit of structural stability of polycrystalline barium hollandite was 0.25 Cs ions per unit cell. Cheary [13] reviewed the Cs incorporation in SYNROC. In $Ba_xCs_y[(Al^{3+}Ti^{3+})_{2x+y}Ti^{4+}_{8-2x-y}]O_{16}$, high concentrations of Al produced superlattices with longer periods. The superperiod was sensitive to Cs/Ba ratio. Three-dimensional order was obtained with Cs and Ba end members containing Ti^{3+}.

Carter [14] reported synchrotron XRD data for the hollandite series $Ba_xFe_{2x}Ti_{8-2x}O_{16}$. This system showed tetragonal to monoclinic transformation at room temperature with increasing Ba-content, demonstrating stabilization of the tetragonal hollandite phase at room temperature. Aubin and coworkers [15] studied incorporation of cesium in the $Ba_xCs_y(Al,Fe)_{2x+y}Ti_{8-2x-y}O_{16}$ in the $(x + y < 2)$ compositional range via solid-state reaction. In this system, the authors selected the Ba-Al hollandite composition, $Ba_{1.16}Al_{2.32}Ti_{5.68}O_{16}$ for exposure to 1.0-2.5 MeV electron irradiation generated by a Van der Graff accelerator. Electron spin resonance (ESR) data on the irradiated sample revealed formation of two Ti^{3+} centers and one superoxide ion (O_2^-). Carter and Withers [16] extended this further to a wide range of barium titanate hollandites covering $Ba_x^{2+}M_x^{2+}Ti_{8-x}^{4+}O_{16}$ (where M = Co, Fe, Mg, Mn, Zn) and $Ba_x^{2+}M_{2x}^{3+}Ti_{8-2x}^{4+}O_{16}$ (where M = Fe) synthesized via alkoxide route followed by solid state sintering and quenching. This study showed that the solid solution ranges differed significantly for a Ba concentration range of x ~ 1.1-1.3. The thermal history (cooling or quenching) dictated the ordering of Ba ions in this system.

Leinekugel-le-Cocq and coworkers [17] studied cesium retention in a hollandite composition ($Ba_1Cs_{0.28}Fe_{0.82}Al_{1.46}Ti_{5.72}O_{16}$), a critical requirement for waste form application, by following two synthesis routes, an alkoxide route and a dry route. While the alkoxide route yielded multiple phases, the dry route yielded a single tetragonal hollandite material. Study of cesium-containing hollandites was extended to include various ions (M = Al, Cr, Fe, Ga, Mg, Sc) [17] as well as to quantify amorphous phase formed in this family of materials [18].

Angeli, McGlinn, and Frugier [19] studied the chemical durability of the Cs-containing hollandite ceramics ($BaCs_{0.28}Fe_{0.82}Al_{1.46}Ti_{5.72}O_{16}$) to assess the effect of the pH on alteration and the effect of the sample-surface-area-to-solution-volume (SA/V) ratio. Cesium and barium releases from the Fe-hollandites were congruent at a pH of 1 but the incongruency increased with pH. These results showed that the SA/V

did not affect the cesium release. Dissolution study of hollandite ceramics under gamma irradiation [18] used radioactive isotopes, ^{137}Cs and ^{133}Ba. In the general testing, cesium and barium releases were incongruent with a correlation slope of about 0.5 at a pH of 2.5, 4.4, and near 0.02 at 95°C. Leaching and isotopic addition experiments showed that cesium release was pH independent, while barium release was strongly pH dependent. Experiments under ^{60}Co gamma radiation did not show any significant effect on leaching. Recently, Montel [20] reviewed the area of different minerals as waste forms including hollandite and zirconolite and suggested some new potential minerals, chrichtonite ($SrTi_{14}Fe_7O_{38}$), kosnarite ($KZr_2(PO_4)_3$), and florencite ((Rare Earth Element)$Al_3(-PO_4)_2(OH)_6$ for this application.

Costa, Xu, and Navrotsky [21] used high-temperature oxide melt solution calorimetry to measure the enthalpy of formation of constituent oxides in the family of barium hollandites for application as waste forms. The authors synthesized these compounds using the metal citrate combustion method and characterized the structure using the Rietveld analysis of the XRD data. Thermodynamic stability increased with decreasing average cation radius in the β sites. While the Al- and Fe-hollandites were found to be stable, the Mg-hollandiate was not stable. Under Fuel Cycle Research and Development (FCR&D) work, this was further explored in detail. Melt fabrication was used to fabricate hollandites into multi-phase waste form with Ti/TiO_2 additions for combined waste stream with Mo content 3% instead of 14%. These compositions were melted in air, Ar and 1%H_2/Argon and characterized in detail. Overall, the composition and process for incorporating combined Cs/Sr, lanthanide and transition metal (Mo, Zr) into crystalline ceramic waste form with promise of higher waste loading and durability as compared to borosilicate glass baseline were demonstrated.

1.3 Pyrochlore

Pyrochlore has a general composition of $A_2B_2X_6X'$, where A is a 2 or 3 + cation, B is a 4 or 5 + cation, and X and X' are anions (O^{2-}). Many studies of pyrochlore materials stemmed from the electrical, dielectric and magnetic properties this structure can provide [22]. Pyrochlore became a phase of interest for this project due to its ability to incorporate actinides and rare-earth elements (REEs) into its structure [23]. The structure of pyrochlore was related to a defect fluorite and could be considered as built up layers of perovskite sheets, a so-called expanded perovskite [24]. Multi-phases of SYNROC include perovskite (see Section 5 for more detail) and pyrochlore phases with the same A to B ratio. Radius ratios dominated when determining if stable structures were formed. Stable structures were formed when R_A/R_B= 1.29-2.30 [23]. The radius ratios also determined the lattice of the pyrochlore. When R_A/R_B= 1.46-1.78, a cubic pyrochlore was formed. Below that ratio, a defect fluorite was formed and above that was a monoclinic lattice [25]. Pyrochlore was synthesized in a number of ways, including solid-state methods [22c], polymerized complex method [22a], steric acid method [26], and sol-gel processing [22d].

Pyrochlore phases were identified as hosts capable of immobilizing excess weapons Pu [27]. The authors determined thermodynamic properties of actinide bearing pyrochlore phases, namely $CaCeTi_2O_7$ and $CaUTi_2O_7$, to optimize processing conditions. The authors concluded that the both pyrochlores were stable with respect to their oxygen phase assemblage (negative ΔH), the U-pyrochlore was stable with respect to perovskite and oxide phase assemblage, and the Ce-pyrochlore was metastable with respect to perovskite and oxide phase assemblage (entropy stabilized). Data was collected using a Tian-Calvet twin

microcalorimeter. In a similar vein, the formation enthalpies of rare earth titanate pyrochlores, $RE_2Ti_2O_7$ (RE = Lu to Sm or Y) were determined in a similar fashion [23]. RE pyrochlores were synthesized growing single crystals by using the high-temperature flux method or by sol-gel. It was determined that these pyrochlores were also stable with respect to their oxides. A trend showing decreasing stability with decreasing R_A/R_B was observed.

The aqueous chemical durability and irradiation resistance of titanate pyrochlores was also studied. Titanate pyrochlores showed low aqueous solubility and form a layer of TiO_2 on the surface of samples after leaching of the surface, which had low aqueous solubility [25]. When irradiated from an external source, samples showed volumetric swelling (< 6%) and amorphization. The dissolution of the samples remained the same in the crystalline and amorphous states [28]. In a separate study, the radiation damage and response to alpha-decay events in U-, Th- and Ce-doped pyrochlores was simulated by 1 MeV Kr^{2+} ions. Critical amorphization was found to increase with increasing Zr content and was connected to the average ionic ration of the atoms on the A and B sites. This allowed for better design of actinide bearing pyrochlores [29].

Titanate pyrochlores were studied because of their structural variability. They allowed for the incorporation of a variety of impurity atoms because of the variable state of Ti [25]. However, titanates had low irradiation resistance. To improve irradiation resistance, Zr was added in place of Ti. This increased the irradiation resistance, but reduced the structural variability and increases the processing temperature. Solid solubility between zirconates and titanates was limited [25].

1.4 Zirconolite

Zirconolite is one of three major phases present in SYNROC. It is a phase of interest because of its ability to incorporate U, tetravalent actinides and to a lesser extent REEs and trivalent actinides [30]. The solubilities of many elements in the zirconolite structure were studied over the past two decades. It was found that about 17 mol % of U was incorporated into zirconolite before a pyrochlore phase was formed, while only 8 mol% of Th^{4+} could be substituted onto the Zr-site. This lower occupancy was attributed to the larger ionic radius of Th^{4+}; however, Th^{4+} strongly partitioned to the Ca-site. Based on ionic radii sizes, smaller REE ions partitioned to the Zr-site and larger REE ions, to the Ca-site [30].

In 1994, Vance and coworkers [31] showed that Nd^{3+} and Ce^{3+} could substitute for 65 mol% of Ca in zirconolite while maintaining a monoclinic lattice as long as Al^{3+} is used for a charge compensator on the Ti^{4+} site. At substitution levels of 65 - 85 mol%, an orthorhombic zirconolite formed and any substitutions at greater levels resulted in additional phases. It was also seen that trivalent Pu and Np enter the Ca-site, while tetravalent Pu and Np enter the Zr-site. Other groups observed that 10 mol % Np and Pu could incorporate without charge compensators [32] and the solid solution of Hf in zirconolite on the Zr-site [33].

Swenson, Nieh, and Fournelle [34] studied the $CaO\text{-}TiO_2\text{-}ZrO_2$ system in more detail. The authors prepared nine compositions from TiO_2 (anatase, 95.5%), fine-grained ZrO_2 (> 95%), and dried CaC_2O_4 (99.9%), pressed them into pellets, heat-treated at 1200°C for 10-14 days in air, and air-cooled. These samples were characterized using XRD and the electron-probe microanalysis (EPMA). The system also showed formation of zirconolite ($CaZrTi_2O_7$) and a second ternary phase, $Ca_2Zr_5Ti_2O_{16}$ (calzirtite, a natural

mineral). Figure 1-3 (a-c) shows a summary of the phase equilibria in this system and Table 1-4 shows the summary of the XRD data.

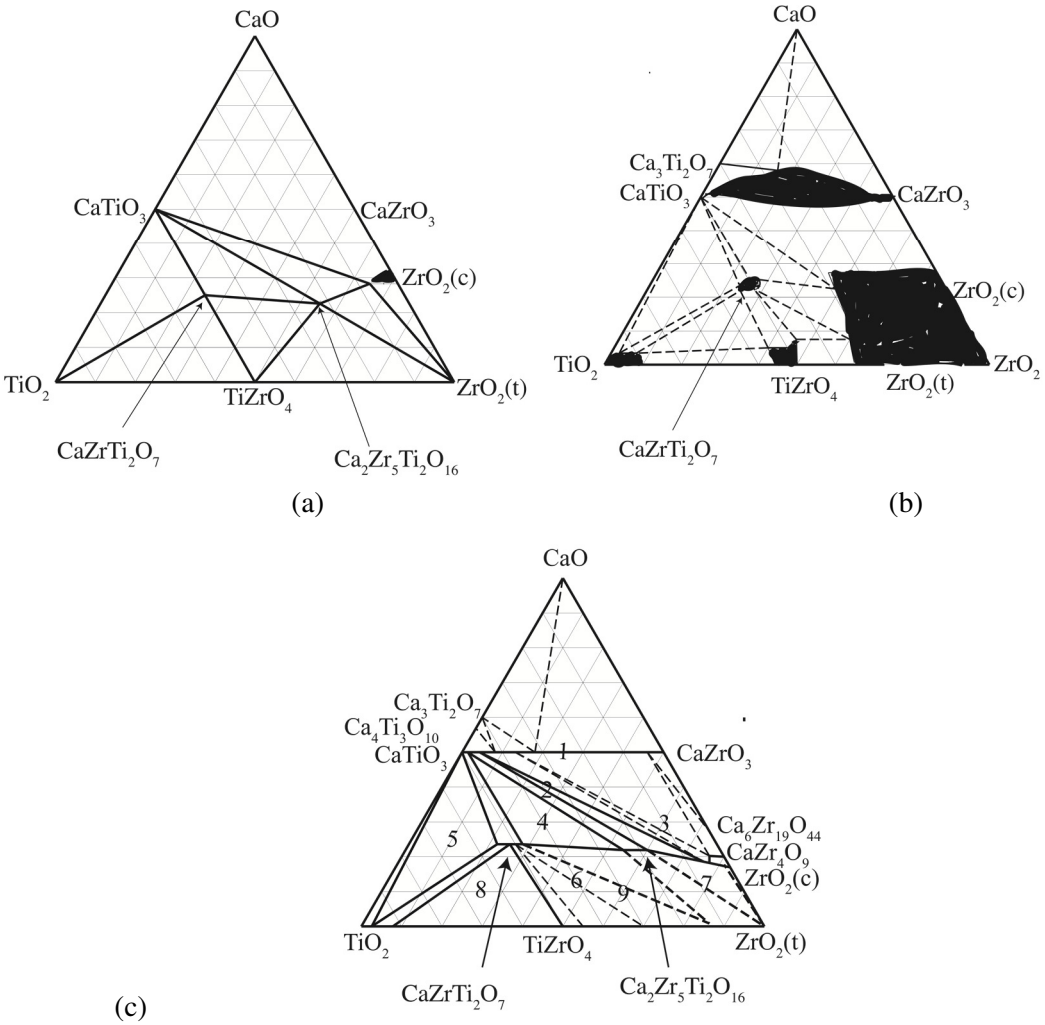

Figure 1-3. Phase equilibria in the CaO-TiO_2-ZrO_2 at (a) 1450-1550°C, (b) 1300°C, and (c) 1200°C [34b]

Table 1-4. XRD and EPMA data summary [34a]

Sample number	Gross composition (mol%)			Phase identified by XRD	Composition of phases (mol%)		
	CaO	TiO_2	ZrO_2		CaO	TiO_2	ZrO_2
1	50.0	25.0	25.0	$CaZrO_3$ $CaTiO_3$	49.7(4)* 49.9(1)	10.8(28) 39.2(1)	39.5(27) 11.0(1)
2	40.0	35.0	25.0	$CaTiO_3$ ZrO_2 (c) $Ca_2Zr_5Ti_2O_{16}$	49.3(6) 18.3(3) 22.1	47.8(13) 3.7(1) 17.4	2.9(13) 78.0(3) 60.5
3	30.0	10.0	60.0	$CaZrO_3$ $CaZr_4O_9$	49.4(4) 19.8(4)	17.0(12) 2.6(4)	33.6(11) 77.6(7)
4	30.0	40.0	30.0	$Ca_2Zr_5Ti_2O_{16}$ $CaZrTi_2O_7$ $CaTiO_3$ m-ZrO_2	22.1(3) 24.9(4) 48.7(5) 0.2	23.5(3) 46.2(6) 50.5(3) 3.4	54.4(4) 29.0(3) 0.8(5) 96.4
5	25.0	65.0	10.0	$CaZrTi_2O_7$ $CaTiO_3$ TiO_2	24.6(2) 49.1(4) 1.1(6)	54.4(4) 50.8(4) 96.0(2)	21.0(3) 0.3(0) 2.6(3)
6	15.0	40.0	45.0	$CaZrTi_2O_7$ m-ZrO_2 TiO_2	24.3(3) 0.4(2) 0.4(1)	49.9(5) 13.8(1) 91.6(0)	25.8(5) 86.0(4) 8.1(0)
7	12.0	8.0	80.0	m-ZrO_2 $Ca_2Zr_5Ti_2O_{16}$	1.9(7) 21.8(1)	1.4(4) 18.0(4)	96.7(11) 60.3(3)
8	10.0	65.0	25.0	$CaZrTi_2O_7$ $TiZrO_4$ TiO_2 m-ZrO_2	23.5(1) 0.2(1) 0.3(1) 0.1	51.1(9) 50.1(12) 91.9(3) 29.2	25.5(8) 49.8(13) 7.8(3) 70.7
9	10.0	30.0	60.0	m-ZrO_2	0.1(1)	13.8(1)	86.1(1)

The thermal expansion of zirconolite was studied by Vance *et al*. [35]. XRD and thermal analysis were performed on the samples at 1200-1500°C. The samples experienced bloating effects from trapped gases. It was also noted that no solid-state transformation was observed up to 1450°C when examined by high-temperature XRD and thermal analysis. Other thermodynamic functions, such as enthalpy and Gibbs free energy of formation, as well as heat capacity, have been studied in detail [36].

Irradiation damage is important when storing actinides due to alpha decay. In 1983, Clinard and coworkers studied zirconolite that was self-irradiated with Pu [37]. After 800 days, samples showed volumetric swelling (5.5%), amorphization and extensive microcracking. The microcracking was due to differences in swelling of the zirconolite and a cubic polymorph that was formed during irradiation. Other interesting behaviors of zirconolite when irradiated include the independence of doping with critical amorphization dose (D_C) [38], the effect of temperature [39] and type of ion on D_C , damaged structures [40] and the influence of Ca on susceptibility of amorphization [39].

Aqueous stability was also a focus of research. In one study, Nd-doped zirconolite was subjected to Materials Characterization Center (MCC)-2 test at 150°C. It was seen that the pH (5) of the leachants stayed constant throughout the test and that elemental releases became steady state after one day of leaching [41]. A comprehensive study of the aqueous stability of Ce- and Pu-doped zirconolite was performed by Poml and coworkers [42]. They used 5 different solutions (HCl, NaCl, NaOH, NH_3 and pure H_2O), a temperature series (100-300°C), a surface area-to-volume ratio series and a series using different reaction vessels. It was determined that only the HCl solution had a dramatic effect on dissolution, the temperature, and SA/V ratio had very little impact and the electrolytes from the reaction vessels had a large impact on solubility.

1.5 Other Phases

Perovskite ($CaTiO_3$) is one of the three major phases present in SYNROC. Perovskite is a phase of interest due to its ability to incorporate REEs and actinides into its structure [43]. Early studies focused on the densification of perovskite via solid state methods [44]. Heat transport properties of specific heat, thermal diffusivity and thermal conductivity were also studied to examine how the material would react on exposure to heat during storage. It was found that perovskite had good thermal properties (e.g., specific heat, thermal diffusivity, and thermal conductivity) of materials that make up SYNROC [45].

Irradiation damage of perovskite was studied using fast neutron doses ($\geq$ 1 MeV) to simulate 6×10^5 years of actinide damage. The perovskite samples exhibited volume expansion between 2 and 6 %, which caused a decrease in bulk density. With this volume expansion and decrease in density, there was very little (0.01%) increase in the open porosity of the sample [43b].

Perovskite showed the lowest aqueous durability when exposed to leachants of the phases present in SYNROC; however, a layer of TiO_2 formed on the surface of leaching perovskite, increasing the aqueous durability over time [43a].

Elemental partitioning studies showed that REE such as Ce and Nd strongly partitioned to perovskite over zirconolite [43a]. In SYNROC, 97% of U and > 90% of REE were incorporated into either zirconolite or perovskite. It was found that the REE choose which Ca lattice site to partition to (zirconolite

or perovskite) based on ionic radii. The polyhedral volumes of the eight-fold coordinated Ca sites of zirconolite and perovskite were 0.021 nm^3 and 0.030 nm^3, respectively. Therefore, larger ions such as Nd^{3+} and Ce^{3+} preferentially partitioned to perovskite. The partitioning coefficients were also affected by the presence of Na [43a]. Pu and Np incorporation into perovskite was explored by Begg [32]. In the case of pervoskites, firing in air yielded tetravalent, while annealing under reducing atmosphere, trivalent Np. In the case of zirconolite, tetravalent Np was found in samples processed under oxidizing as well as reducing conditions.

Powellite ($CaMoO_4$) is a phase of interest because it contains Mo in its structure. Mo is an element found in some high-level waste streams and cannot be easily incorporated into perovskite, pyrochlore or zirconolite. Most studies involving powellite deal with glasses or glass-ceramics. Molybdenum has low solubility in borosilicate glasses used for waste immobilization and can combine with other ions to form a "yellow phase" when the saturation limit has been reached [46]. This yellow phase is formed during the melting process of waste glasses, and contains molybdates, such as Cs-molybdate, which is very soluble in water and lowers the overall chemical durability of the waste glass [46]. Powellite can also incorporate actinides, REEs and Sr into its structure on the Ca-site [47]. In terms of aqueous solubility, powellites are water insoluble [48], improve the durability of glass-ceramic waste forms [49] and can form a film of leached actinides on the surface [50].

Mo had a low solubility in borosilicate waste glasses (< 1 wt.%) [46]. To increase the amount of Mo that could be incorporated in the waste form, excess Ca and Zr have been added to glasses to purposefully form a crystalline powellite phase resulting in up to 12 wt. % Mo in the glass-ceramic [51]. The addition of Nd_2O_3 into the glass has also been shown to increase the Mo incorporation [52]. Calas and coworkers [53] studied the local environment of Mo in glasses using the extended x-ray absorption fine structure (EXAFS). They found that Mo was surrounded by alkali and alkaline-earth element and was not linked to the borosilicate network. This aided in the formation of powellite phases. Additions of excess B_2O_3 resulted in modification of the Na^+ distribution in waste glasses, possibly contributing to the formation of low solubility phases such as Na_2MoO_4 [33].

Hartmann and coworkers [54] investigated incorporation of ^{99}Tc into pyrochlore, $Ln_2Tc_2O_7$, where Ln represents Ln^{3+} cations and Tc, Tc^{4+} cations. The authors used XRD and Rietveld analysis to identify the phases present in the samples and SEM, to study the morphology. Ruddlesten-Popper phase $A_{n+1}B_nO_{3n+1}$ with A^{2+} = (Sr, Ba) and B^{4+} = (Ti, Ru, Tc) was another phase that was recently investigated for waste form application [55]. The authors used hot-forging to prepare samples and grazing incidence XRD (GIXRD) and transmission electron microscopy (TEM) to characterize them. On irradiation with 200 keV He ions, the lattice spacing of the samples increased. Amorphization was observed in some compositions in this family of materials.

1.6 Preliminary Results

The project was started on January 1, 2013 at Alfred University. In this section, our preliminary results are briefly summarized. First, three single-phase compounds were synthesized via solid state sintering.

Constituent oxides and carbonates were mixed and heated to form compounds via solid-state reaction. Additional major phases formed en route during processing. The processing details are summarized below:

- **Pyrochlore ($Nd_2Ti_2O_7$)** – 1250°C for 10 h, 1350°C for 24 h, and 1450°C for 24 h; Pyrochlore phase was present in 1250°C treatment, but formation was slow. Small amount of Nd_2O_3 persisted through prolonged processing at 1350°C, but was eliminated at treatment at 1450°C; however, the grain growth at 1450°C was significant, so a crushing-repelletizing step was implemented after 1350°C for 24 h treatment and calcined a second time at 1350°C for 12 h. This resulted in phase pure powders.
- **Zirconolite ($CaZrTi_2O_7$)** – 1400°C for 72 h followed by crushing, repelletizing, and calcination at 1450°C for 72 h; Processing at 1400°C for 24 hours yielded $CaTiO_3$, which reacted with ZrO_2 to form $CaZrTi_2O_7$; however, after prolonged processing at this temperature for 72 hours, the major phase formed was $CaZrTi_2O_7$, along with ZrO_2 and small amounts of $CaTiO_3$. After the second calcination step, phase pure powders were obtained.
- **Hollandite** – FigureFigure 1-4 1-4 shows the hollandite ($Ba_{0.28}Ti_{1.44}Al_{0.56}O_4$) formation. The processing sequence was: 820°C for 4 h, 1320°C for 96 h, and 1350°C for 10 h. After processing at 820°C, $BaTiO_3$ and $BaAl_2O_4$ formed along with residual Al_2O_3, $BaCO_3$, and TiO_2 from the starting materials. On processing at 1320°C for 96 h, $Ba_{0.28}Ti_{1.44}Al_{0.56}O_4$ started forming with some TiO_2 remaining. After processing at 1350°C for 10 h, TiO_2 was not detected and the sample was phase-pure.

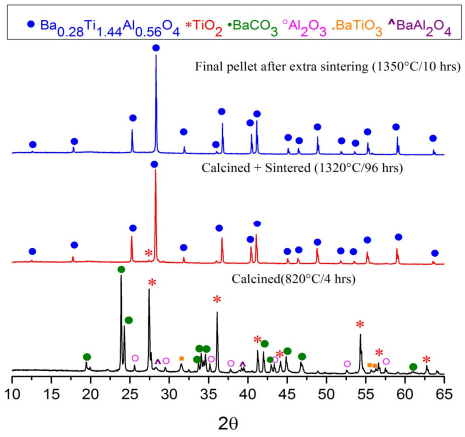

Figure 1-4. XRD data of formation of hollandite

1.6.1 Spark Plasma Sintering

SPS was used to fabricate monoliths of the $Nd_2Ti_2O_7$ pyrochlore single-phase compound. SPS applies pressure and electric current simultaneously, which allows for more homogenous sintering, shorter sintering times (heating rates of up to 400°C/min), and lower sintering temperatures (less grain growth) compared to conventional sintering. Two SPS trials for $Nd_2Ti_2O_7$ were completed. Pyrochlore was sintered

at 1250°C for about 20 minutes. The sample from second trial had a density of 6.026 g/cm^3 (about 98.7% of theoretical density). Figure 1-5 shows the sintering curve for the second trial that demonstrates that the process is reproducible. The sample was heated at 100°C/min to 1250°C at 54 MPa pressure. The black line represents the temperature, while the blue line, the piston speed, which is an indicator of when the material is sintering. Most the sintering occurs at around 1150°C. The smaller shoulder adjacent to the sintering peak is due to thermal expansion, as the sample contracts on cooling. The XRD data shows preferred orientation of the 001 family of planes in this system (Figure 1-6). This is observed by comparing the relative intensities to the 100 % peak at a 2-theta of 31°.

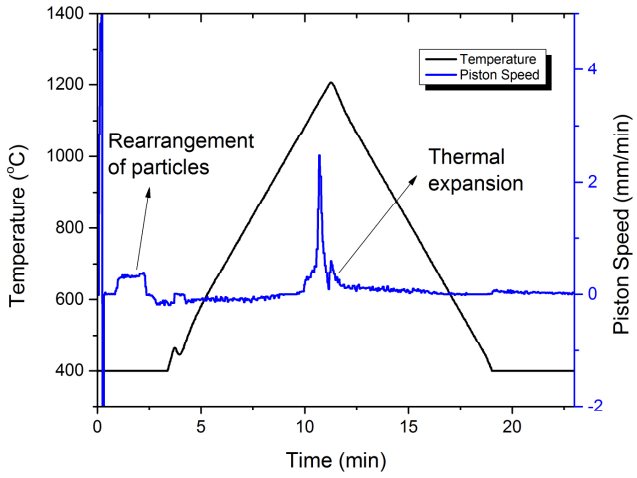

Figure 1-5. SPS process variables – Piston speed and temperature vs. time

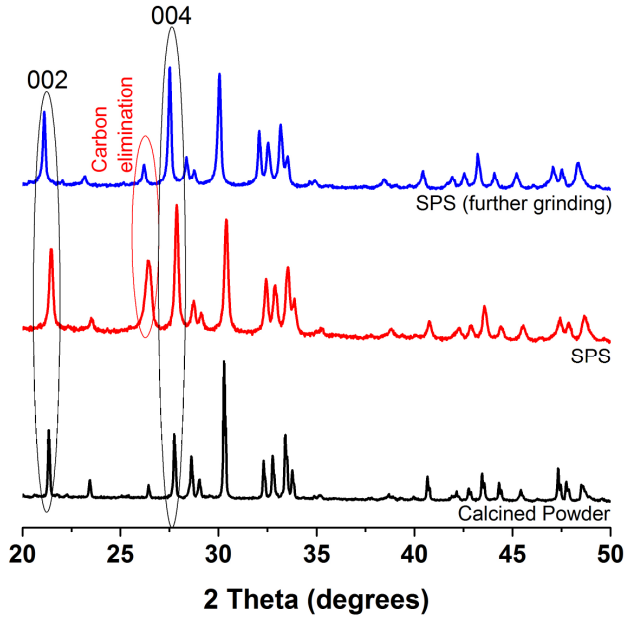

Figure 1-6. XRD data of pyrochlore samples after SPS

SEM revealed large grains as well as pores in the SPS samples (Figure1-7). These microstructures were obtained with the thermally etched samples. The average grain size was measured by the line intercept method and is about 5µm. There is a wide distribution of grain sizes ranging from about 1 to 10 µm. The densities of SPS samples sintered are about 99% theoretical density. Density was measured using ASTM Standard C20, which involves boiling the sample in water. Large grains are indicative of agglomeration of the particles, which was attributed to the pre-reacted (solid-state) powder from pellets used for reaction. No attempt was made to grind the powder to any target particle size or distribution before the SPS trials. Energy dispersive spectroscopy (EDS) results suggested some oxygen deficiency, which was attributed to reducing conditions likely present within the graphite die used in the SPS.

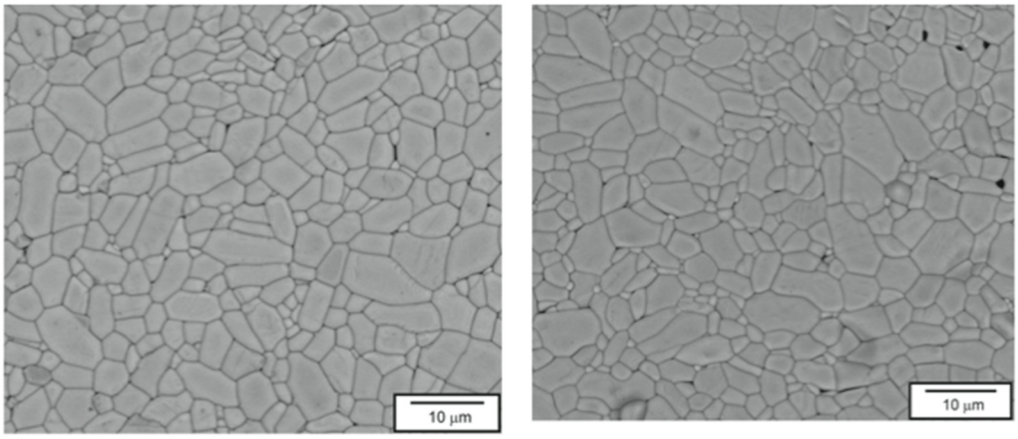

Figure 1-7. SEM of selected areas of SPS pyrochlore

(Average grain size: 4.85 ± 0.58 µm; Density: 6.045 ± 0.027 g/cm^3, 98.98% Theoretical Density)

SPS process was extended to other compounds and hollandite batches received from SRNL. In parallel, reactive sintering via SPS of pyrochlore was explored. Reactive sintering is a one-step process, which requires less processing time, resulting in lower volatilization loss. In the case of reactive sintering, we started with the mixed oxide precursors instead of single-phase compound. Figure 1-8, left shows the sintering curve of a run in which the precursors were heated to 1050°C at 50°C/min, held at that temperature for 30 minutes, and then ramped up to 1250°C to sinter the material, like the simple SPS run on single-phase pyrochlore. The sintering peak was observed around the same temperature as that of the previous run with the single-phase compound. XRD data (Figure 1-8, right) showed that most the phase was Nd_2TiO_5 with some pyrochlore and unreacted neodymium oxide. When this run was repeated at a higher temperature of 1200°C, the sintering peak position did not change, but the XRD data showed almost exclusively Nd_2TiO_5 and no pyrochlore. Hydroxide phase was due to the presence of Nd_2O_3, which had absorbed water over time during processing. These results suggested that selecting the right starting materials, increasing their activity, and sintering at a suitable temperature to get the desired phase can help to optimize the process.

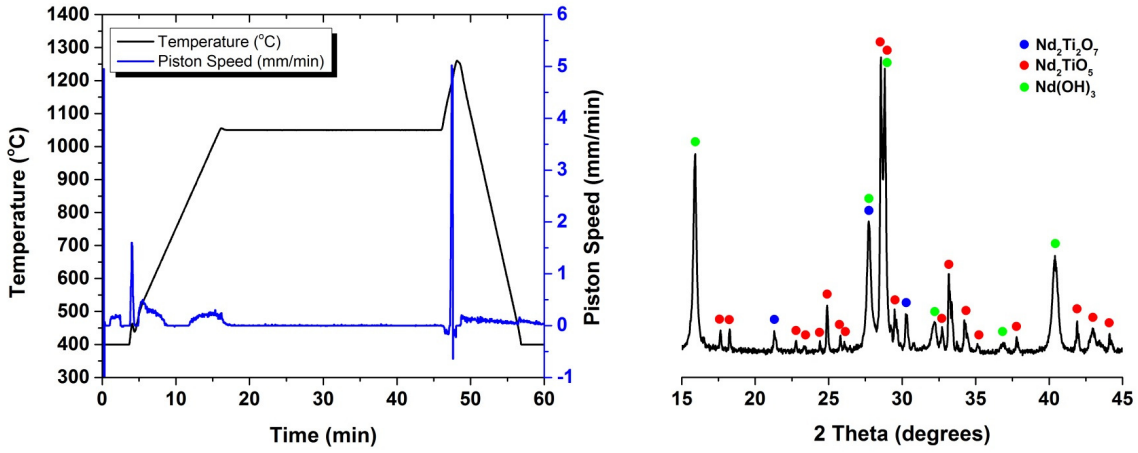

Figure 1-8. Left: SPS reactive sintering curve; Right: XRD of the reaction-sintered sample

1.6.2 Melt-Processing

Three different single-phase hollandite ($Ba_{0.28}Ti_{1.44}Al_{0.56}O_4$) samples were initially prepared to determine appropriate heat treatment schedules for melt processing of hollandite. Detailed thermal histories of these samples were as follows:

- Try_2: Sample was heated from room temperature to 1550°C at a heating rate of 5°C/min, maintained at that temperature for 1 hour, and cooled inside a tube furnace
- Try_3: Sample was placed in a drop bottom furnace at 600°C, heated to 1550°C at a maximum heating rate allowed by the furnace, maintained at that temperature for 1 hour, and air-quenched allowing cooling in air.
- Try_4: Sample was placed in a drop bottom furnace at 1050°C, heated to 1550°C at a maximum heating rate allowed by the furnace, maintained at that temperature for 2 hours, and air-quenched allowing cooling in air.
- Figure 1-9 shows XRD results of these samples. The XRD patterns were identical consisting mostly of single-phase hollandite with a second phase of Al_2TiO_5. Based on these results, the processing steps used for Try_3 sample were applied to the following batches received from SRNL for melt processing:
- Fe-SP-HOL – Single-phase hollandite (Fe)
- Cr-SP-HOL – Single-phase hollandite (Cr)
- CAF-SP-HOL – Single-phase hollandite (Cr/Al/Fe)
- Cr-MPB1 – Multi-phase simulant (Cr)
- CAF-MPB1 – Multi-phase simulant (Cr/Al/Fe)

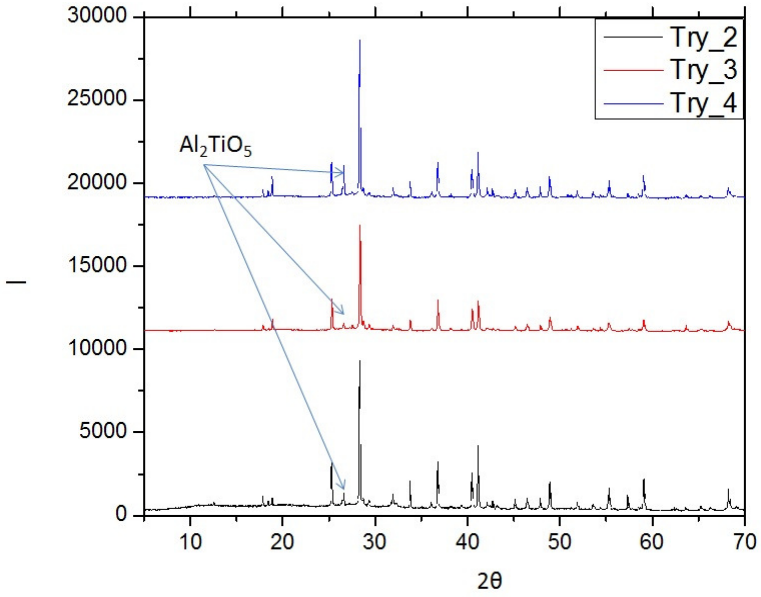

Figure 1-9. XRD data of melt-processed hollandites

These batches were milled in water and dried in an oven. Batch materials were ground and calcined at 800°C for 4 h. The melt-processed samples were characterized using XRD and scanning electron microscopy-wavelength dispersion spectrometry (SEM-WDS). The XRD data showed appropriate single-phase and multi-phase compounds in these samples, as expected. Selected results are shown in Figure 1-10, which shows that TiO_2 was the only minor second phase detected in the case of single-phase hollandites. Multi-phase ceramic samples contained hollandite, perovskite, and pyrochlore.

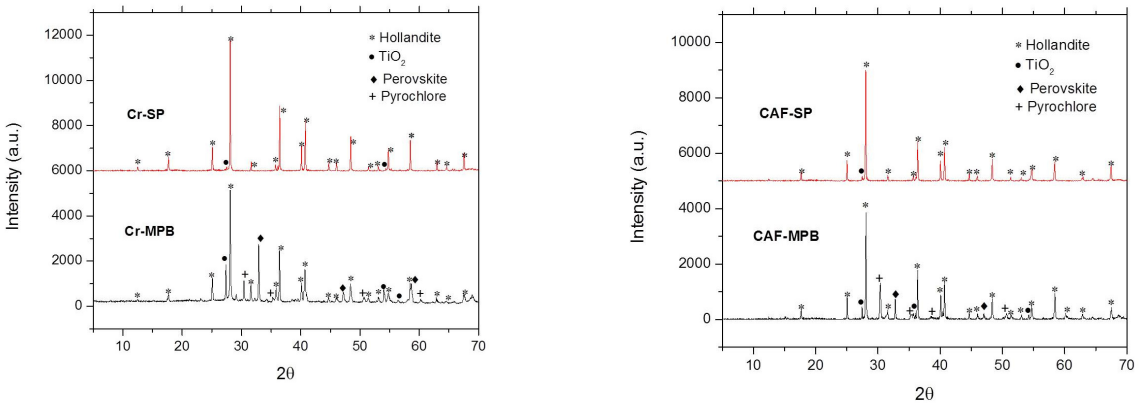

Figure 1-10. Left: Single-phase vs. Multi-phase hollandites (Cr); Right: Single-phase vs. Multi-phase hollandites (Cr/Al/Fe)

Soblev and coworkers [56] compared the SYNROC ceramic samples processed via hot-pressing and inductive melting. These samples had similar mineral compositions with hollandite, zirconolite, perovskite, and rutile as major phases. Cesium incorporation was lower in the melt-processed SYNROC, compared to hot-pressed SYNROC. Reducing conditions will be needed to avoid molybdate formation in these samples. Morphology and waste form properties of samples prepared via melt-processing is expected to be significantly different from the morphology of samples processed via SPS. Another issue observed in SRNL work is that the melt-processed phases are highly substituted with various REE in a single phase that might vary across the grain, whereas solid-state sintering methods produce discrete phases, which are not as highly substituted. These microstructural changes will affect the waste form performance (e.g., radiation stability, chemical durability).

1.7 Conclusion

Based on the status of the literature, research progress at SRNL and other researchers in this field, and our preliminary results generated at AU, the selection of the compositional space is complete. The project will focus on three families of compounds, pyrochlores, zirconolites, and hollandites. Besides the SPS, reactive SPS, and melt-processing to optimize multi-phases in the waste forms, the project will advance the fundamental understanding in this compositional space via modeling phase equilibria, developing experimental phase diagrams under the processing conditions, and studying the kinetics of multi-phase formation in these families of compounds. Single-phase and multi-phase compounds and simple doping schemes will be used in this project. Cesium incorporation into the hollandites and cerium, samarium, and prasedium into the pyrochlores and zirconolites will be studied to determine the limits of the compositional space. High-temperature *in situ* quantitative XRD will be used in determining the evolution of multi-phase waste forms. SEM, EDS, and WDS will be used to study the morphology and phase boundaries and determine the dopant incorporation into the phases and their distribution across the microstructure.

This final report summarizes the results of the project and details our results on the characterization and testing of both single and multiphase materials for use as nuclear waste forms. Ce incorporation into single phases of zirconolite and pyrochlore as well as Cs incorporation into hollandite is presented. The microstructure, chemical durability, and radiation damage of multiphase ceramic waste forms prepared at AU via two different processes, melt-processing and SPS are also presented in this report.

2) Multiphase Waste Form Compositions and Processing (Tasks 2 & 3)

Processing methods used to fabricate ceramic waste forms affect the final performance of these waste forms in terms of chemical durability and radiation resistance. Table 2-1 shows specific multiphase hollandite compositions prepared under the task 2 of our project.

In melt processing, combined carbonate and oxide precursors are heated to melting (above the liquidus temperature) followed by cooling to room temperature during which crystalline phases precipitate as the melt forms a solidified multiphase ceramic. Since melters are already being used for the vitrification of high-level waste (HLW) in the United States as well as in many countries, melt processing allows for

high throughput of waste forms with minimum airborne contamination due to the processing of fine powders. Extensive reported literature and knowledge in melting and solidification of materials in general help prediction of phase assemblage and performance of the waste form. In addition, crystallization kinetics can be used to tailor a structure with maximum actinide concentration at the core and minimum at the rim, thus reducing the leachability [57] of the actinides from the waste form. Disadvantages of melt formation are the potential volatilization of waste elements at the elevated temperatures needed for melting to occur and difficulty in controlling the cooling rate and microstructural features.

SPS is of interest as an alternative fabrication technique because of the comparatively short processing time (a total of about 20 min) that is required to achieve a dense ceramic material. The short processing times (along with self-contained sample inside the die) can reduce the volatilization of waste elements. Uniaxial pressure and a DC current are simultaneously applied to a graphite die containing the powder sample. The current generates resistive heating of the graphite die (and the sample if electrically conductive), which creates fast heating rates of up to 1000°C/min [58]. As shown in Figure 2-1, the current flows through the graphite punches, across and into the cylindrical die, and back to the punch located below the sample. This is the typical current flow during SPS experiments, assuming the resistance of the sample is much greater than that of the graphite hardware. The SPS processing environment is inherently reducing, as it utilizes a graphite die, and can produce high-density samples compared to melt processing. SPS is limited by the throughput that can be obtained with current instrument configurations and carbon diffusion from the die into the sample occurs at elevated temperatures [58]. But, the carbon diffusion can be minimized or even possibly eliminated by designing and incorporating suitable sacrificial barrier coating of the die. In addition, post-SPS heat treatment in air or oxygen can burn off the carbon from the sample.

Compositions of multi-phase hollandite waste forms based on simulated waste streams compositions were provided by SRNL based on the advanced fuel cycle initiative (AFCI) aqueous separation process developed in the FCR&D. In the case of target compositions, oxide and carbonate precursors were mixed together via ball milling with deionized water using zirconia media in a polyethylene jar for 2 h. The slurry was dried overnight and then separated from the media. The blended powders were then subjected to melt or SPS processing.

Table 2-1. Multi-phase simulated waste form compositions

Oxide	CAF-MP (wt.%)	Cr-MP (wt.%)
Al_2O_3	1.27	0
BaO	12.76	12.72
CaO	1.39	1.38
Cr_2O_3	6.33	14.5
CdO	0.11	0.11
Ce_2O_3	3.10	3.09
Cs_2O	2.88	2.87
Eu_2O_3	0.17	0.17
Fe_2O_3	6.65	0
Gd_2O_3	0.16	0.16
La_2O_3	1.58	1.58
MoO_3	0.85	0.84
Nd_2O_3	5.23	5.22
Pr_2O_3	1.45	1.44
Rb_2O	0.42	0.42
SeO_2	0.08	0.08
Sm_2O_3	1.08	1.07
SnO_2	0.07	0.07
SrO	0.98	0.98
TeO_2	0.66	0.65
TiO_2	49.16	49.01
Y_2O_3	0.63	0.63
ZrO_2	2.99	2.98

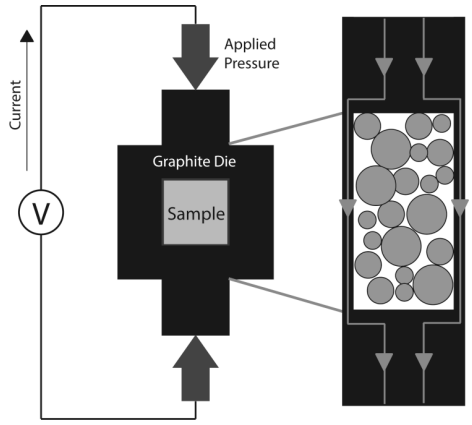

Figure 2-1. Schematic of the graphite die set up in SPS

Reaction via SPS was carried out using a FCT HP D 25 (FCT Systeme GmbH, Rauenstein, Germany) furnace with graphite dies and punches. The unreacted powder was placed inside of the graphite die with a thin layer of graphite paper between the die and sample. The reaction schedule was as follows: a heating rate of 100 °C /min for both compositions to a maximum temperature of 1000°C or 1125°C for CAF-MP and Cr-MP respectively, a hold time for 3 min, and a cooling rate of 100 °C/min. The samples were subjected to 54 MPa pressure throughout the reaction.

XRD patterns of the two compositions fabricated by SPS and melt-processing are shown in Figure 2-2. Similar phase assemblage is seen in all samples, with hollandite as the major phase, perovskite and a zirconium-rich phase. The melt-processed samples contain some unreacted TiO_2, while the CAF-MP sample processed by SPS contains some CeO_2.

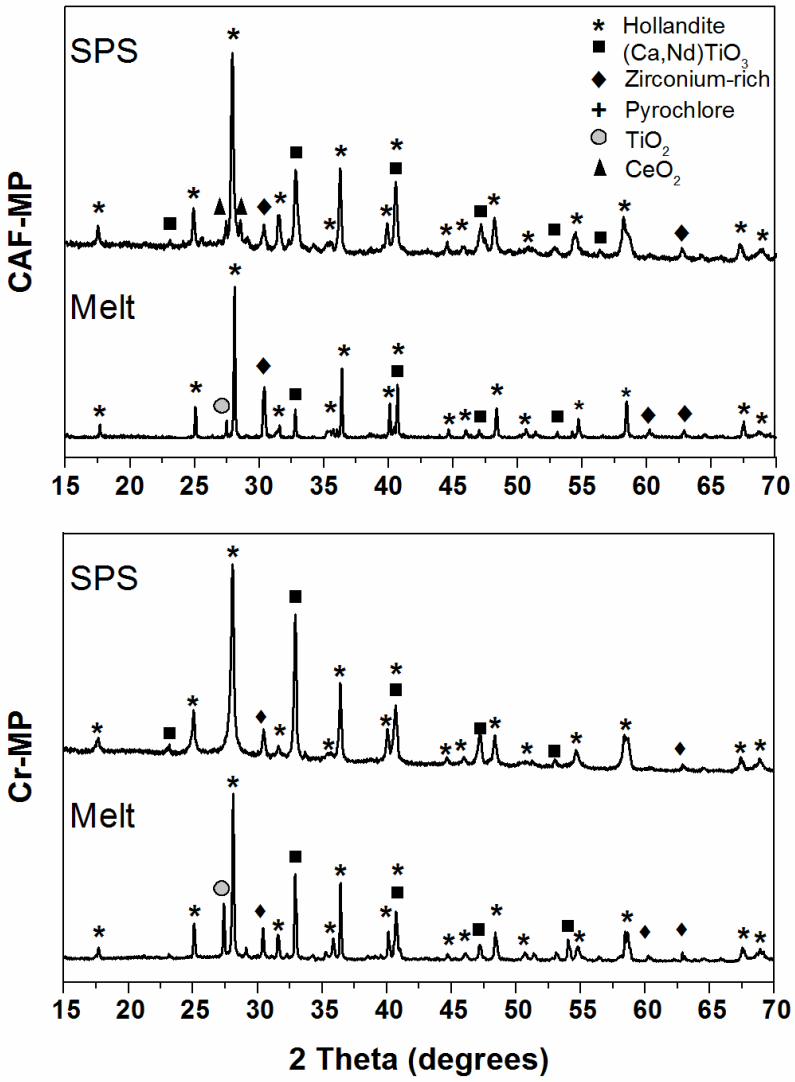

Figure 2-2. XRD patterns of CAF- and Cr-MP samples produced by SPS and melt-processing

Contrary to the phase formation results, the microstructures of the samples using the two processes were dissimilar. Figure 2-3 compares the two microstructures. The sample processed by SPS shows a fine grain structure with highly dispersed phases amongst the matrix (hollandite). In contrast, the melt-processed sample contains larger islands of the different phases that are aggregated to each other.

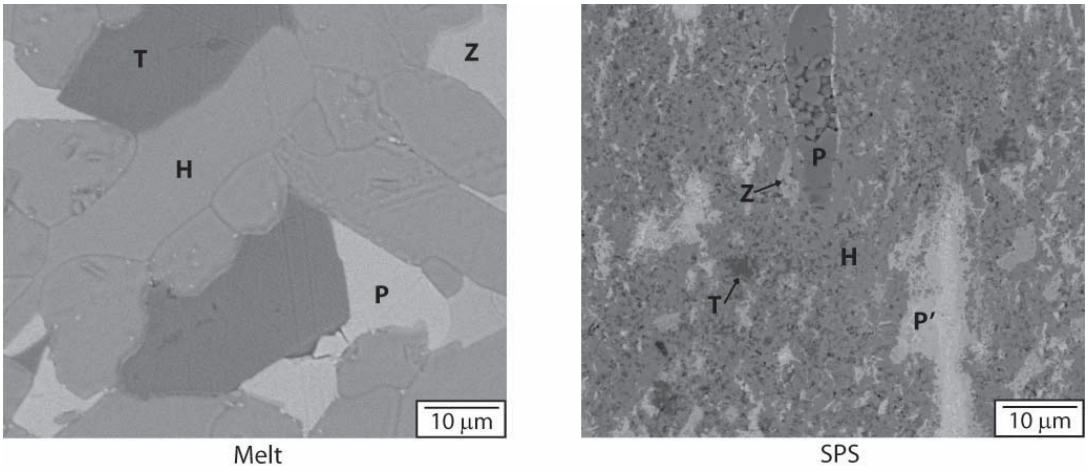

Figure 2-3. Microstructures of SPS and melt-processed CAF-MPB samples with phase fields indicated. H = hollandite, P and P′ = perovskite, Z = zirconium-rich, and T = TiO_2

The phases seen in the microstructures were identified using a combination of EDS maps and XRD patterns. The appropriate phase fields are indicated in the images. Hollandite phase is represented with H, perovskite with P and P′, a zirconium-rich phase with Z, and TiO_2 with T. It should be noted that the identification of the zirconium-rich phase (Z) is inconclusive from a combination of EDS and XRD analysis. This phase may also belong to a zirconolite. Figure 2-4 and Figure 2-5 compare the WDS maps of selected elements in these multiphase samples.

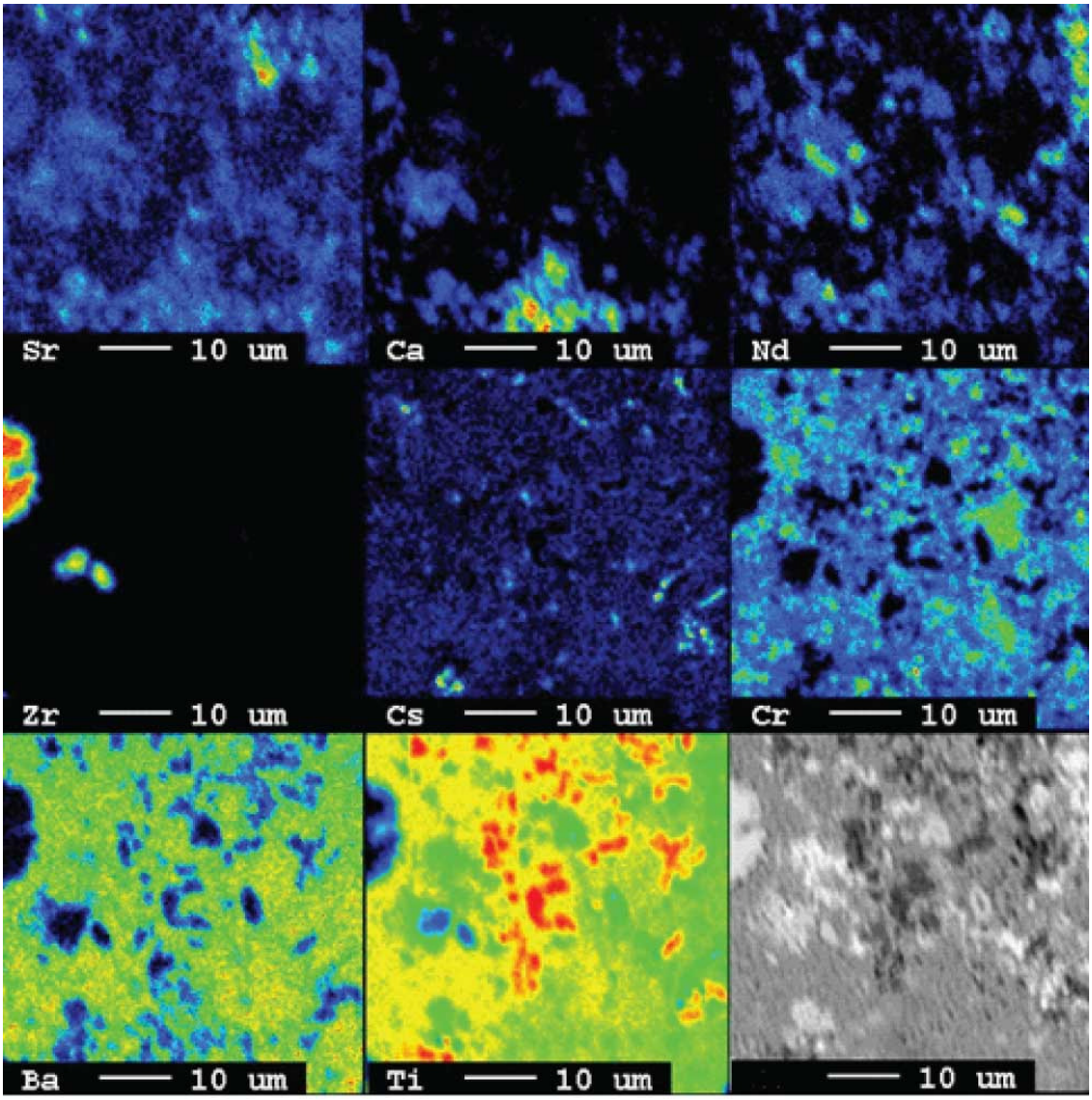

Figure 2-4. Selected elemental maps by WDS in CAF-MP prepared by SPS

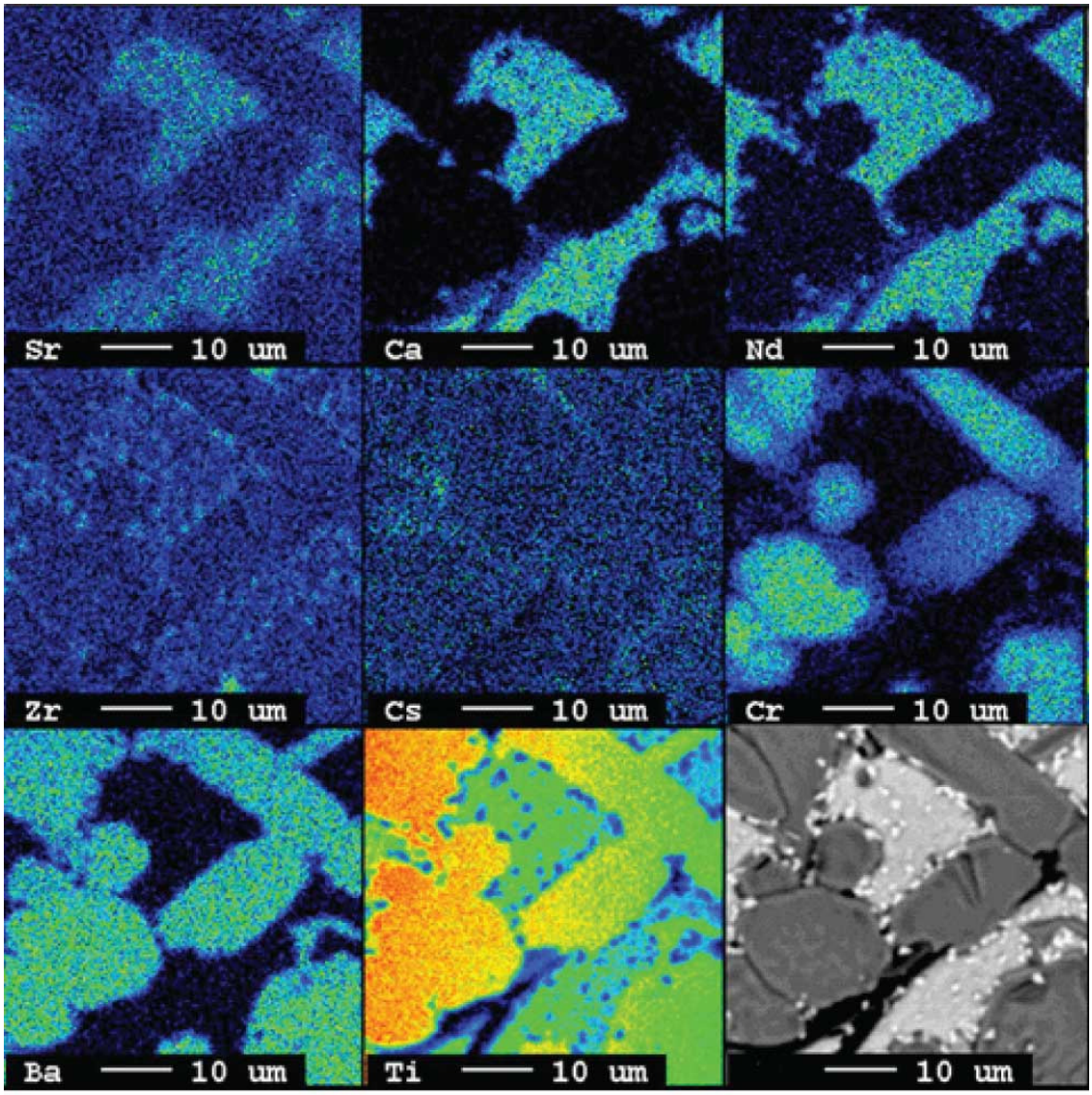

Figure 2-5. Selected elemental maps by WDS in CAF-MP prepared by melt processing

In the SPS sample, hollandite formed the matrix of the sample and the remaining phases were dispersed throughout. The inter-dispersed phases ranged in size from < 1 µm to ~10 µm. EDS measurements revealed two separate perovskite phases present, a gray colored phase and a brighter phase, denoted P and P′ respectively in Figure 2-3. The gray phase was rich in Fe, while the bright phase was rich in REEs such as Nd, in agreement with expected atomic mass ratios. A small amount of a cerium and titanium rich phase was seen in EDS, corresponding to the CeO_2 observed in the XRD pattern. The WDS results corroborate that hollandite makes up the matrix and that multiple perovskite phases are present, some high in alkaline

earth elements (Sr and Ca) and other high in REE such as Nd. The zirconium-rich phase consists mainly of Zr and very little Sr (of the elements that were observed in WDS), indicating that this phase may be a solid solution of ZrO_2.

Initial visual observation of the melt-processed samples indicated that the samples were fully melted. Different phases were crystallized from the melt, with retention of some unreacted TiO_2. Significant porosity was observed in the microstructure. Small amounts of Cs were detected in WDS mapping (Figure 2-5) that appeared to be segregated towards the grain boundaries of hollandite phase. From all the WDS maps in Figure 2-5, it could be observed that hollandite phase has elements predominantly Ba, Cr, Ti, O and Cs as per the target composition. All other elements like Ca, Sr, Nd, Ti partitioned together into the bright perovskite phase, suggesting that different perovskite and pyrochlore phases could be formed in the process hosting different elements, actinides, REEs etc. in their lattices. This phase assemblage and microstructure work was published in a paper titled 'Microstructures of Melt-Processed and Spark Plasma Sintered Ceramic Waste Forms' in the *Metallurgical and Materials Transactions E* [59].

This microstructure work was extended in a recent publication in the *Journal of Solid State Chemistry* titled 'Cesium Incorporation in Hollandite-rich Multiphasic Ceramic Waste Forms' [60]. As-prepared CAF-MP-Melt had a characteristic melt-solidified structure as evident from the wetting of Pt foil. There was no chemical reaction with Pt and the sample could easily be removed off from the foil. CAF-MP-SPS sample was relatively strong and dense, as typical of SPS processed material. The measured bulk density was relatively high (4.64 g/cm^3) compared to that of CAF-MP-Melt (4.07g/cm^3).

As mentioned in our previous work (details in Nucleation and Growth Study section), initial phase identification of these materials showed that hollandite was the major phase followed by perovskite and pyrochlore/zirconolite along with small amounts of TiO_2. Although it was initially presumed that this could be the excess or unreacted TiO_2 [59], our recent study showed that during melt-processing, rutile is one of the final phases recrystallized during solidification of CAF-MP [61]. However, in case of SPS, it could either be recrystallized or unreacted TiO_2. CAF-MP-Melt has the typical melt-solidified structure – with large grains of different phases and large pores trapped between growing phases – while CAF-MP-SPS has less porosity and fine-grain structure. The SPS microstructure is a matrix of hollandite phase with small islands of other phases distributed at random. To confirm the phase identification and to study the microstructural phase distribution, electron backscatter diffraction (EBSD) analysis was done. Electron back-scattered patterns (EBSP) or Kikuchi bands collected from different phases matched with the phases identified from XRD.

Figure 2-6 shows the band contrast maps and phase maps for SPS and melt-processing samples. In addition to hollandite and perovskite in CAF-MP-SPS, unreacted CeO_2 was seen segregated and coexisting with pyrochlore or zirconolite phase. In SYNROC-based formulations, Ce^{4+} or Pu^{4+} partitions into Nd-rich pyrochlore or zirconolite phases. This SPS microstructure can thus be interpreted as an ongoing transformation of CeO_2 and provided enough time, total Ce^{4+} in the composition would have substituted into the pyrochlore lattice. EBSD maps together with backscatter electron (BSE) images reveal the microstructural development of SPS samples. Although the visual and microstructural examination indicated no bulk melting, there is a clear implication of long-range mass transport occurring within the samples during the sintering process. Phase distribution map of CAF-MP-SPS shows that the zones of perovskite and pyrochlore phases are randomly distributed in hollandite-rich microstructure and each zone in turn is multi-crystalline.

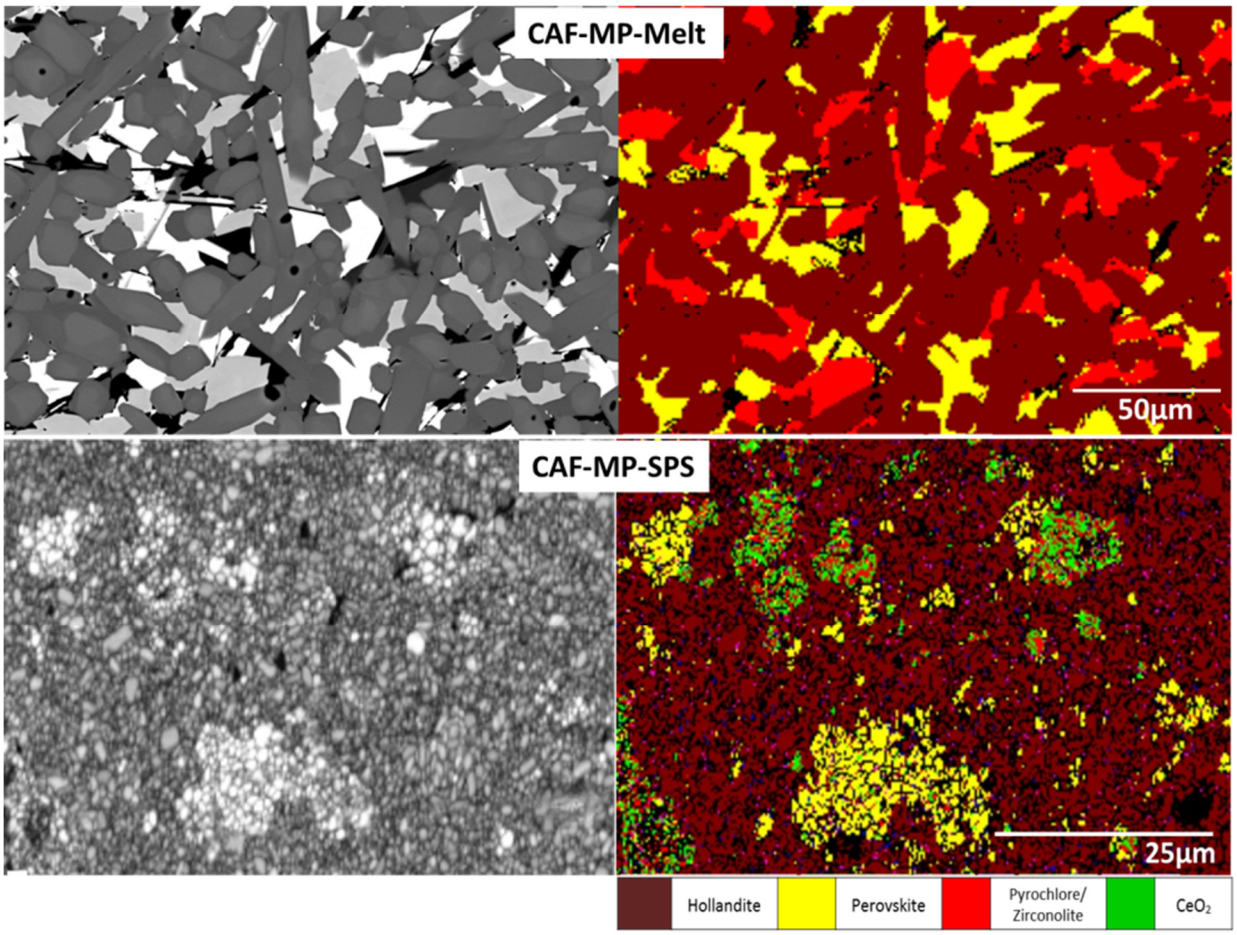

Figure 2-6. Phase maps obtained from EBSD

Figure 2-7 shows the WDS maps of selected elements in CAF-MP-Melt. Hollandite, the major phase, consisted of mainly Ba, Cr, Fe, Ti and Cs. While Ba and Cs are homogeneously distributed, Cr and Fe have compositional gradients across individual grains, as seen in Figure 2-7. Cr content is the highest at the core and diminishes towards the edges of the grains, whereas Fe has the exact opposite trend. The cause of this Cr and Fe segregation is not well understood yet. We attribute this to the competition between Fe and Cr for the oxygen within the grains. Ca is seen in both perovskite and pyrochlore phases but Zr is partitioned preferentially into pyrochlore phase.

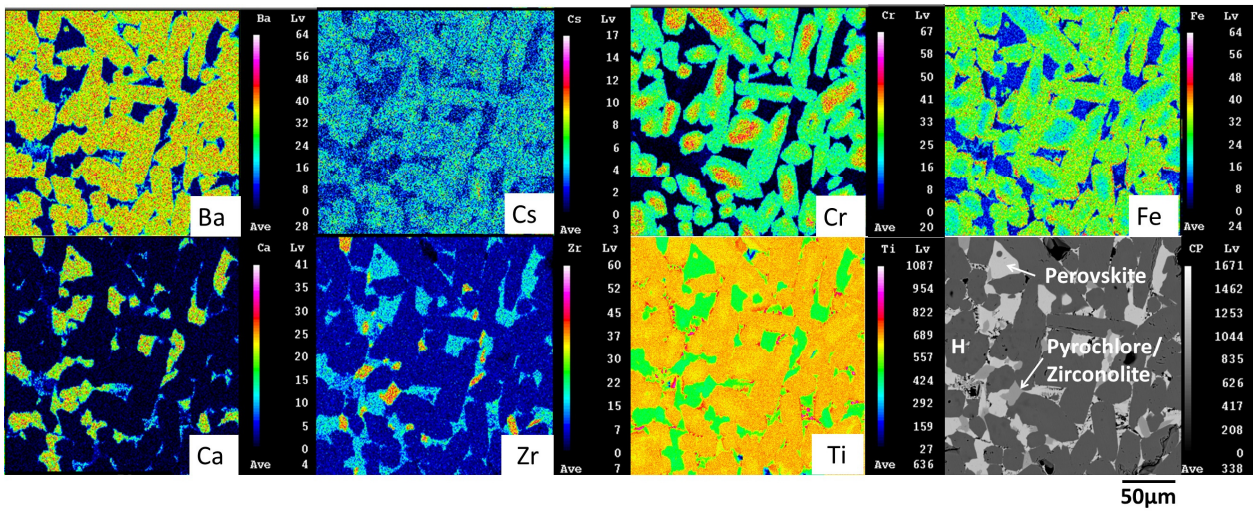

Figure 2-7. WDS maps of selected elements of CAF-MP-Melt

The boundaries elemental maps of SPS sample shown in Figure 2-8 are not as distinct as for melt-processed sample but provide key information. Ba and Cr are distributed throughout hollandite phase, whereas Cs-rich regions are observed in the WDS map. Although the exact chemistry and crystal structure of these Cs-rich phases are not known, they are considered undesirable for waste form application due to higher propensity to Cs attack by water on exposure. The maps confirm that the perovskite (Ca- and Nd-rich regions) and pyrochlore (Zr-rich) phases have appropriate targeted elements in the samples.

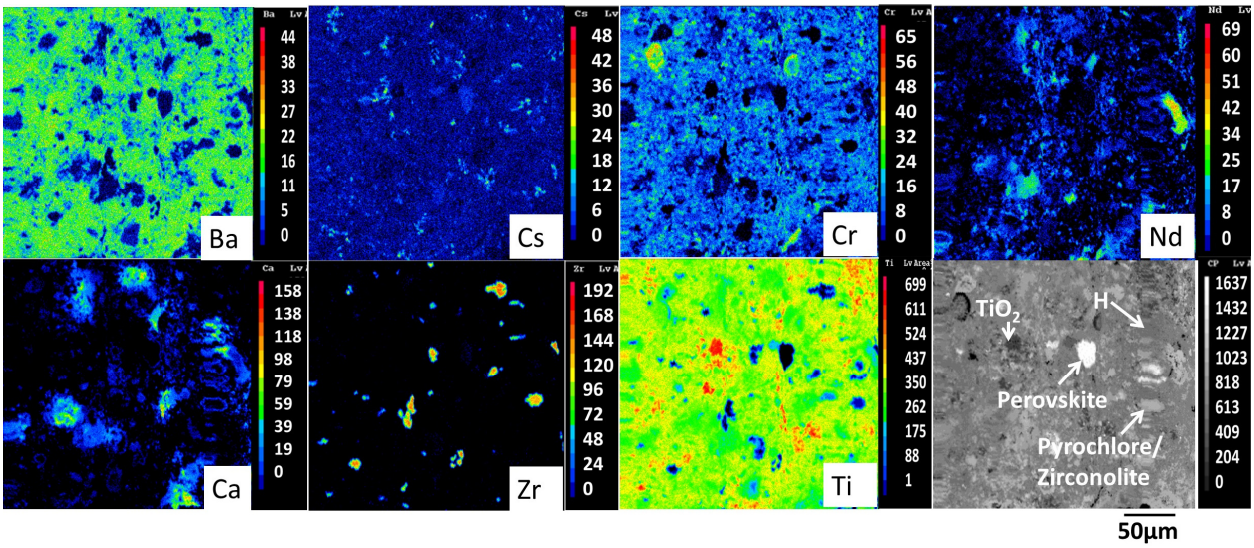

Figure 2-8. WDS maps of selected elements of CAF-MP-SPS

TEM observation of focused ion beam (FIB) milled sample was done to investigate hollandite phase. Since SPS samples were found not to have Cs incorporated into the hollandite lattice, TEM of CAF-

MP-SPS was not performed in this study. Selected area electron diffraction (SAED) patterns collected from hollandite lattice region of CAF-MP-Melt could be indexed using monoclinic (I2/m) unit cell structural model [62]. Figure 2-9 shows the FIB milled fragment, hollandite lattice, and the corresponding electron diffraction pattern along [011] zone axis in Figure 2-9 (a), (b), and (c) respectively. In addition to the strong Bragg reflections resulting from the octahedral framework shown in Figure 2-9 (c), diffuse spots and streaks of low-intensity reflections can be seen. These additional satellite reflections are common in modulated structures and, in general, result from planar defects like stacking faults, twinning or compositional modulations [63]. In case of barium hollandites, the presence of these reflections is generally attributed to compositional modulations.

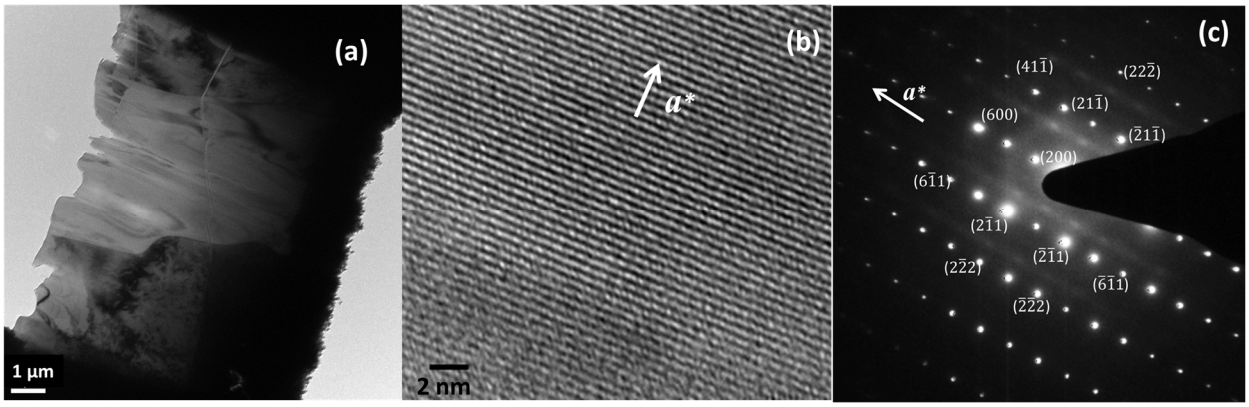

Figure 2-9. (a) FIB-milled CAF-MP-Melt sample used for TEM observation, (b) Hollandite lattice as viewed form [011] zone axis, and (c) the corresponding SAED pattern

The hollandite compositions for waste forms are typically designed in such a way that only a fraction of tunnel sites is occupied by Ba/Cs. It has been widely reported that the cations/vacancies adopt an ordered arrangement within the tunnels forming superlattice structures [64]. Along with this intratunnel ordering, in many cases, intertunnel correlation also exists resulting in three-dimensional modulated structures. This was demonstrated by comprehensive electron diffraction analysis as reported in several works [9, 65]. While the Bragg spots can be indexed by integral multiples of reciprocal lattice vectors ***a****, ***b**** and ***c****, satellite reflections are described by the nature of modulation [63a, 66]. In the SAED pattern shown in Figure 2-9 (c), the satellite reflections and diffuse streaks run parallel to ***a**** as indicated and lie in the plane of ***a**** and ***b****-***c****. Comparing it to the similar reported SAEDs [67] it can be understood that there is presence of compositional modulation in three-dimensions that is, ordering of cations along the tunnels together with intertunnel correlation in hollandite lattice. Due to the limited degree of rotation of the FIB sample, SAED patterns along the principal axes could not be collected and hence, modulations or multiplicities along different directions could not be analyzed. Nevertheless, our data suggests that the hollandite lattice in melt-processed multiphase waste form has three-dimensional ordering of Ba, Cs and/or vacancies. It is to be noted that the location of satellite reflections or the distribution of modulation vectors is sensitive to the local composition. Different crystallites can have different degrees of ordering of tunnel ions resulting in different multiplicities [68].

It is also important to consider the implications on the performance as a waste form. Ba and Cs sites are typically enclosed in a box-shaped network of eight oxygen atoms. When Ba ions along the tunnels are replaced by larger Cs ions, local deformation occurs that must be compensated by the surrounding tunnel sites to maintain lattice stability. Hence, Cs ions tend to occupy isolated sites rather than sites next to occupied Ba/Cs sites and adapt an ordered arrangement with Ba ions resulting in superstructures [69]. These superstructures can result in an increased activation barrier for Cs ions migrating to the adjacent tunnel sites [64c].

3) Nucleation and Growth in Multiphase Ceramic Waste Forms (Task 4)

3.1. Approach for Present Study

The overall objective of this part of the present project is to study and understand nucleation and growth of multi-phase ceramic waste forms during melt-solidification. Since detailed kinetic analyses of different phases with 20+ elements are challenging, this study is focused on mainly determining crystallization sequence during melt processing, phase transformations at different temperatures, and elemental partitioning. Crystallization peaks were identified from differential scanning calorimetry (DSC) runs (as discussed in section 3.3) and multiple annealing/quenching experiments were done followed by extensive XRD and electron microscopy characterization.

3.2 Materials and Methodology

The composition designated CAF-MP (Table 2-1) was used for this study. To study the nucleation and growth of different phases, partitioning of elements during melt processing, a combination of different techniques was used. Crystallization events were identified from DSC curves. Melting and quenching experiments were done to identify the phases present at the corresponding DSC peaks. Phases were identified by XRD, microstructures were observed using SEM, elemental distribution by EDS and WDS. The experimental methods, data and results are discussed in the following sections.

3.3 DSC Measurements

Heat flow at a specific temperature on a DSC curve, during heating and cooling, indicate any exothermic or endothermic events occurring during the process. An exothermic peak during solidification can correspond to a crystallization or nucleation event.

Batches of 10 – 20 mg of starting material (stoichiometric batch) were taken in Pt crucibles to obtain the DSC curves from the following heat cycle. As can be observed in Figure 3-1, the heat cycle was chosen so that phase transformation behavior of CAF-MP, starting from unreacted stoichiometric mixture or as-formed compound, can be studied. Different heating and cooling rates used for this study are 20°C/min, 5°C/min, and 2°C/min. As there was significant background noise observed in 2°C/min cycle data, it was not used for further analysis.

Exothermic peaks were observed in the cooling cycles. In Figure 3-2, cooling paths and crystallization peaks are indicated. Different peaks, which might correspond to nucleation of different phases, are located closely between 1250 and 1350°C (Figure 3-2(a)). At higher cooling rates, single broad peak was observed (Figure 3-2(b)), as expected in case of rapidly cooled samples. The temperatures of the peaks are indicated in Figure 3-2.

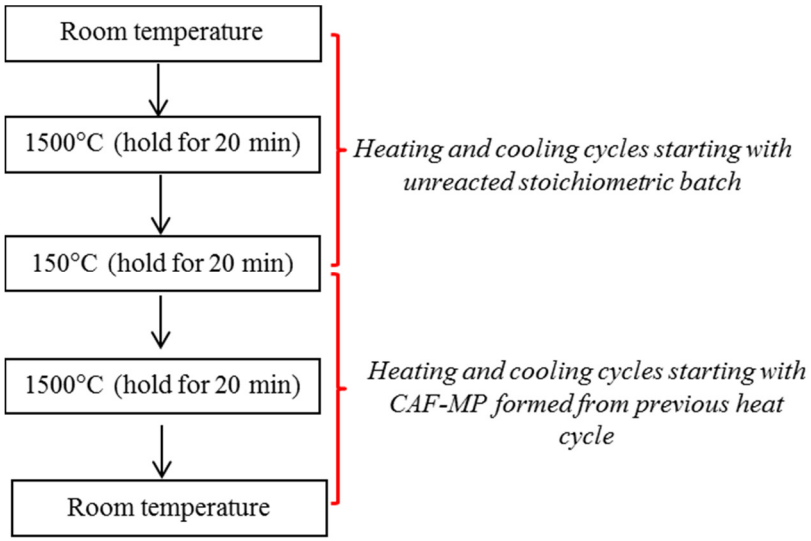

Figure 3-1. Flow chart showing the heat cycle used for DSC measurements

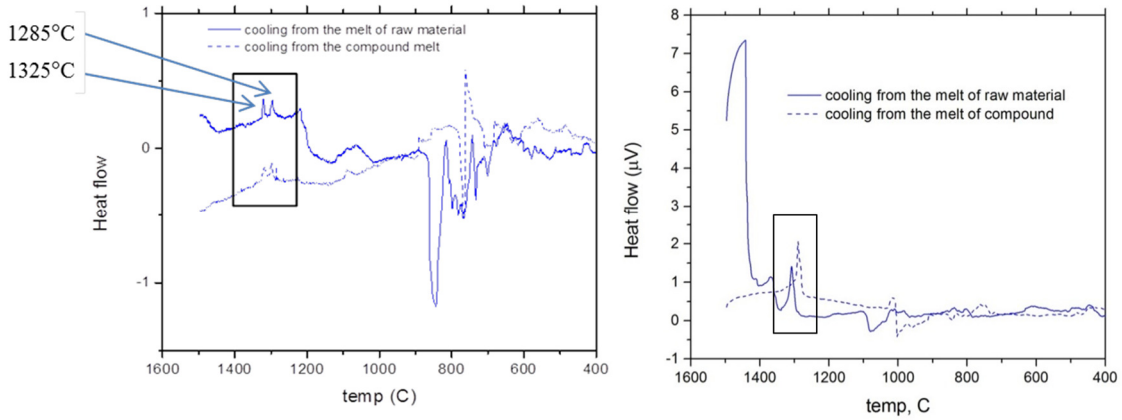

(a) (b)

Figure 3-2. DSC cooling curves for Cr/Al/Fe-MP (a) 5C/min (b) 20C/min

3.4 Nucleation and Growth of Different Phases

To identify nucleation and crystallization/nucleation of phases corresponding to these peaks, melting and quenching experiments were done. Small amount (4 - 5 g) of stoichiometric mixture of raw materials was enclosed in Pt foil. It was melted at 1500°C, held for 20 min, and cooled down to a temperature '*T*' where it was equilibrated for a time 't_{eq}'. The sample was then quenched in water. The temperatures '*T*', where different samples were quenched from, are the temperatures corresponding to the exothermic peaks in DSC curves. One additional sample was quenched directly from melting temperature, 1500°C, to determine whether there were any crystalline phases existed at melting temperatures. Nucleation and growth of different phases can be observed by annealing the sample at the desired for temperature for varying times. Hence, different samples were annealed for different times, quenched and characterized. Figure 3-3 summarizes temperature – time cycle used for these experiments. Table 3-1 shows the temperatures '*T*' and corresponding holding times 't_{eq}'.

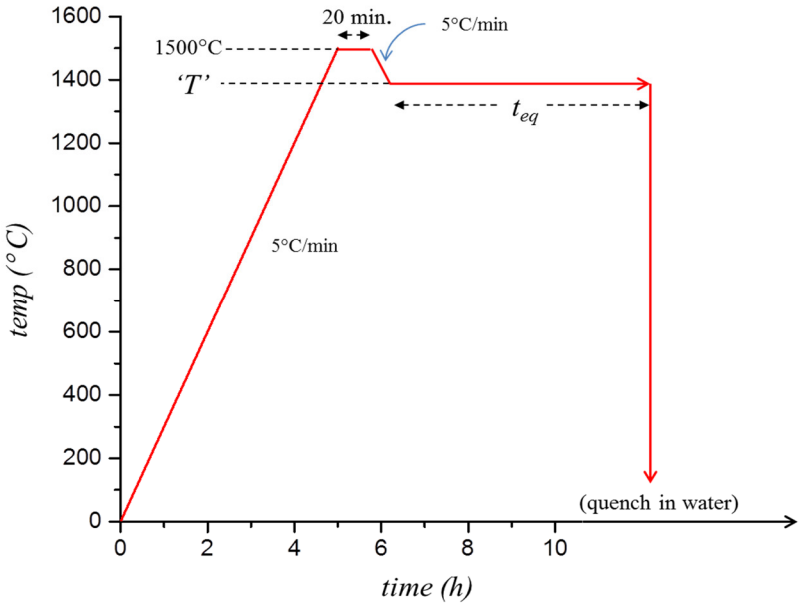

Figure 3-3. Heating/cooling cycle used for melting/quenching experiments

Table 3-1. Temperatures and corresponding holding times from where different samples are quenched

T (°C)	t_{eq} (h)		
1500	1	-	-
1325	1	12	24
1285	1	12	24

Powder XRD patterns were obtained for these samples. Different phases were identified and quantitative analysis was performed using Rietveld refinement of the patterns with TOPAS software. Refinement was done keeping the mismatch between measured pattern and calculated pattern as low as possible. For all the plots shown below in this section, Rietveld weighted parameter (R_{wp}), was observed to be less than 8. Mounted and polished samples were observed for phase and elemental distribution. Quantitative XRD data, corresponding SEM microstructures and WDS maps are presented and discussed in this section.

3.4.1 Phase Assemblage at 1500°C

Sample quenched from 1500°C was crystalline, as observed from XRD pattern (Figure 3-4(a)) and back-scattered images (Figure 3-4(b)). TiO_2 was observed to the major phase followed by hollandite. Peaks corresponding to another phase that would match with $(Ca,Zr,Ti)O_2$ were also identified. The microstructure reveals large rutile grains and fine, long hollandite grains in a bright matrix. Different phases are indicated in Figure 3-4. The microstructure suggests the ongoing transformation from TiO_2 to hollandite phase at 1500°C – nucleation of hollandite phase within TiO_2 grain can be seen in BSE images. EDS of bright colored matrix, indicated as $(Ca,Zr,Ti)O_2$, was found to have all possible elements in the composition. WDS maps of selected elements are shown in Figure 3-5. These maps also support XRD findings about the presence of hollandite, unreacted TiO_2, and some third phase rich in Ca and Zr. Here after this phase would be represented by $(Ca,Zr,Ti)O_2$.

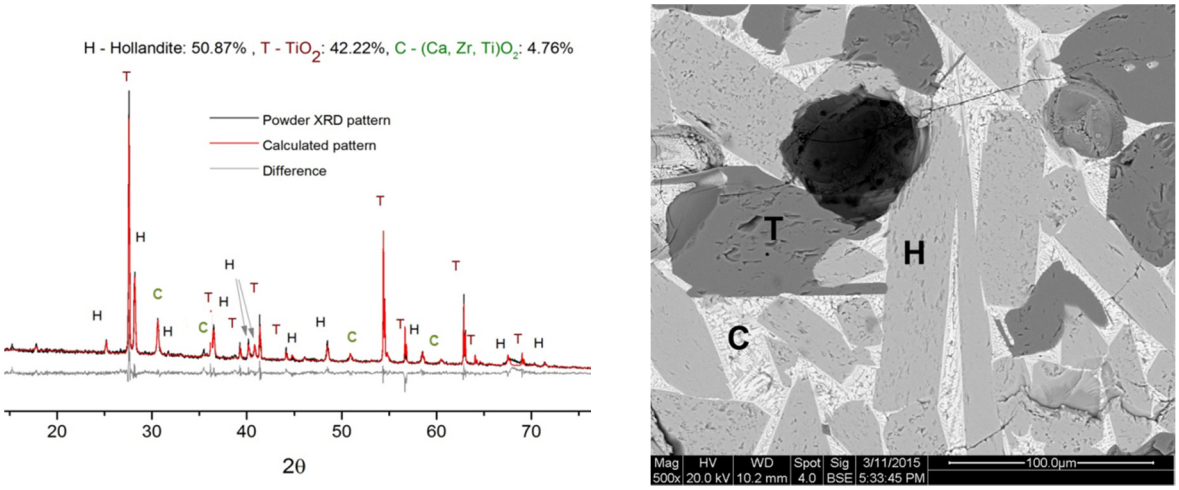

(a) (b)

Figure 3-4. (a) Rietveld quantitative XRD analysis and (b) Back-scattered image of CAF-MP at 1500°C/1h

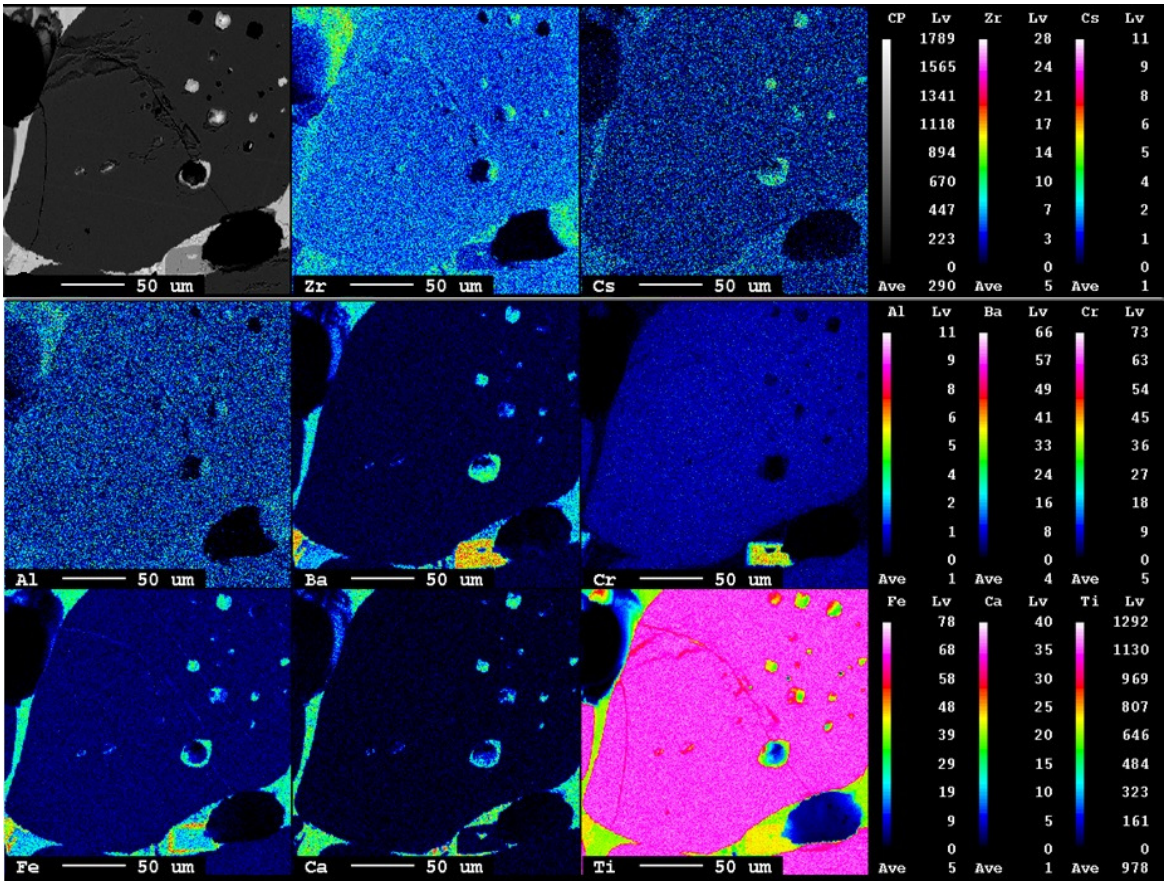

Figure 3-5. WDS maps of selected elements of CAF-MP at 1500°C/1h

3.4.2 Phase Assemblage at 1325°C

Figure 3-6, 3-7, and 3-8 show Rietveld quantitative phase analyses and SEM images of samples annealed at 1325°C for 1h, 10h, and 24h, respectively. Perovskite group peaks are present in all these plots and the relative amount of the phase increased with holding time. It can be understood that nucleation and growth of perovskite phase occurs at lower temperatures (~1325°C). Figure 3-9 shows the WDS maps of selected elements.

Hollandite was the major phase observed when held for 1h at 1325°C, followed by TiO_2 (15.7%) and Zr-rich phase (8%). With time, the amount of unreacted TiO_2 decreased due to the simultaneous growth of perovskite and hollandite phases. Large grains of TiO_2 disappeared and the number of nucleation sites of hollandite appeared to have increased (Figure 3-7). However even after 24h of annealing at 1325°C, unreacted TiO_2 was observed. Perovskite and Zr-rich phase could not be differentiated from the BSE images although the bright colored matrix can be clearly seen to have two phases.

It was not possible to identify the Zr rich phase from the present data since both zirconolite and (Ca, Zr, Ti)O_2 have similar positions for the diffraction peaks. However, the calculated XRD pattern for

1325°C/24h fits better with the presence of both phases zirconolite and (Ca, Zr, Ti)O_2. Holding for longer times would have resulted in transformation of (Ca, Zr, Ti)O_2 lattice to zirconolite lattice.

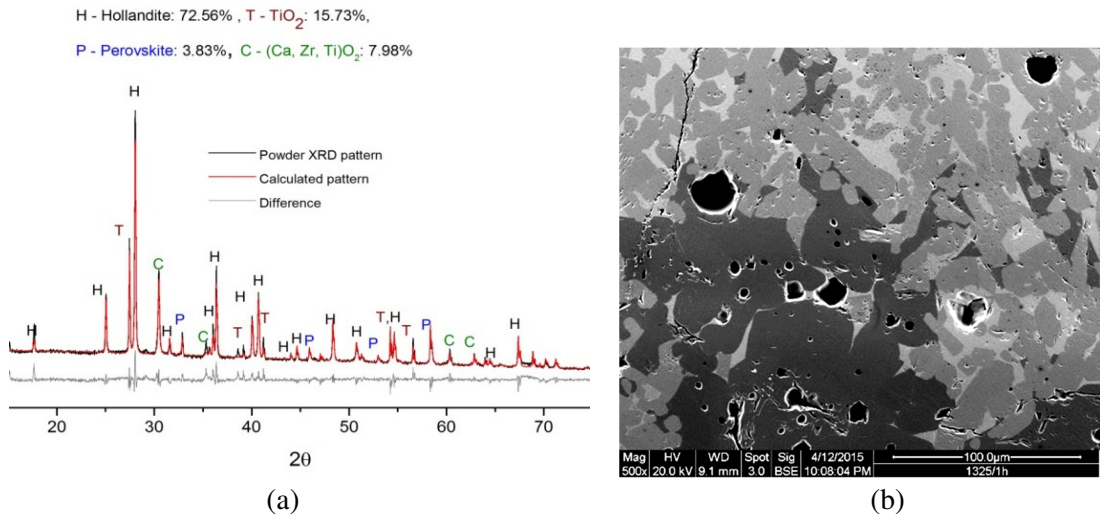

(a) (b)

Figure 3-6. (a) Rietveld quantitative XRD analysis and (b) Back-scattered image of CAF-MP at 1325°C/1h

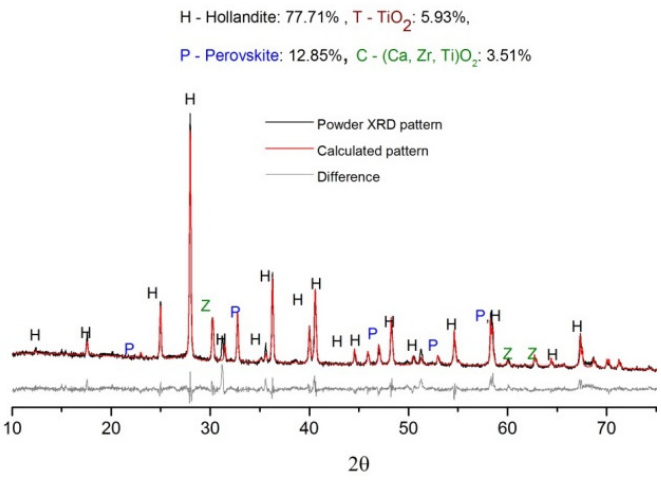

Figure 3-7. Rietveld quantitative XRD analysis and CAF-MP at 1325°C/12h

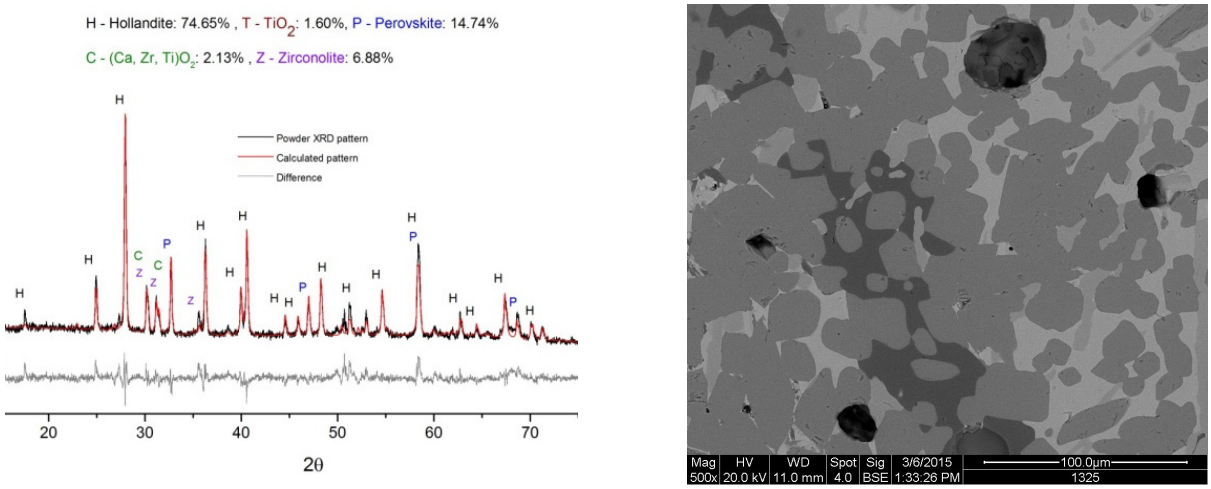

(a) (b)

Figure 3-8. (a) Rietveld quantitative XRD analysis and (b) Back-scattered image of CAF-MP at 1325°C/24h

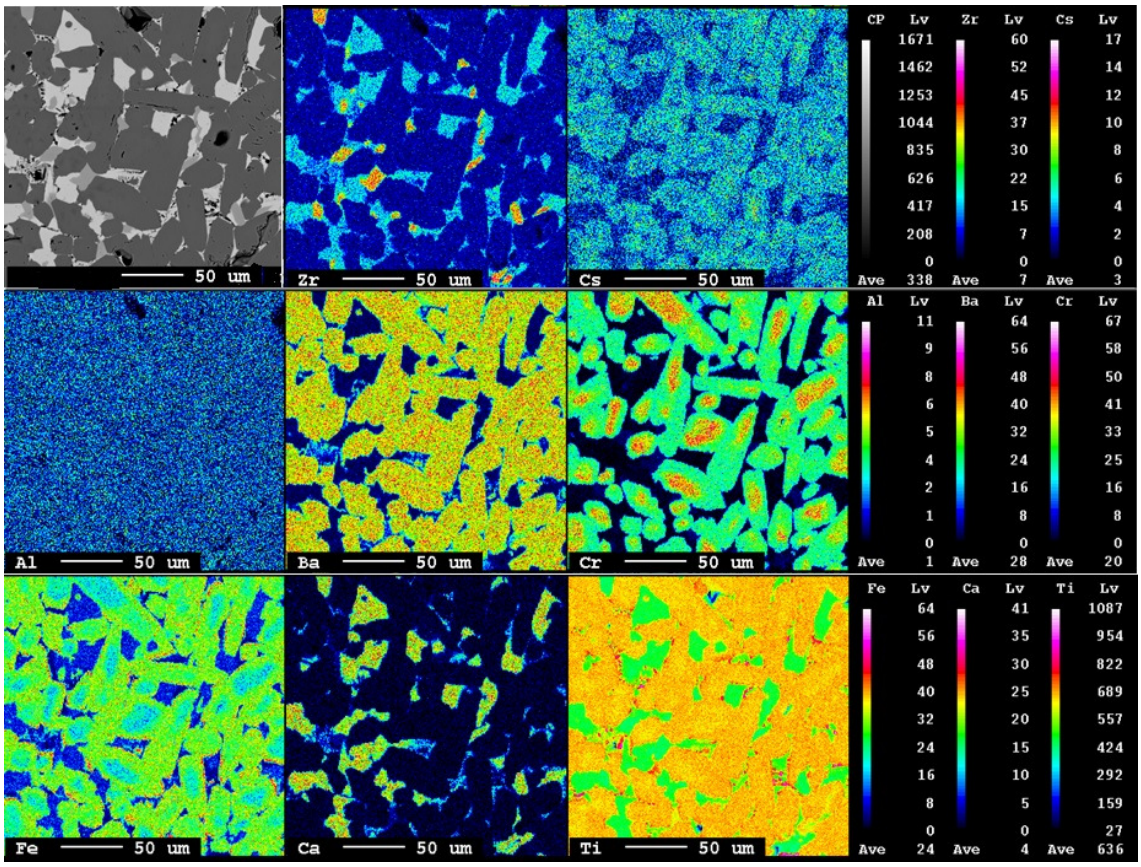

Figure 3-9. WDS maps of selected elements of CAF-MP at 1325°C/24h

3.4.3 Phase Assemblage at 1285°C

XRD phase analysis (Figure 3-10, 3-11, and 3-12) of different samples, annealed at 1285°C for different holding times and quenched, show similar changes in phase assemblage as observed at 1325°C. Figure 3-13 shows the WDS maps of selected elements. Hollandite and perovskite phases grow at the expense of unreacted TiO_2 and Zr-rich phases. Quantitative data are presented in respective XRD plots.

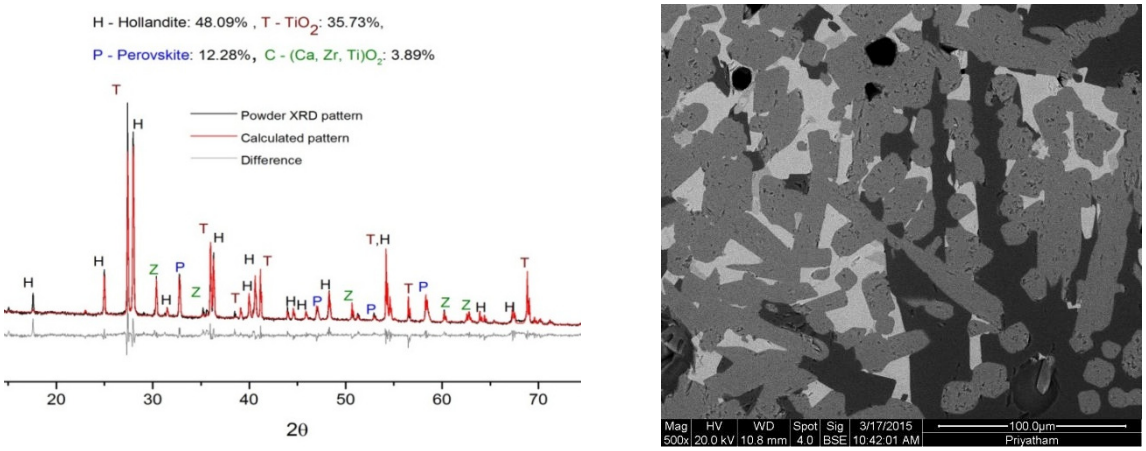

(a) (b)

Figure 3-10. (a) Rietveld quantitative XRD analysis and (b) BSE image of CAF-MP at 1285°C/1h

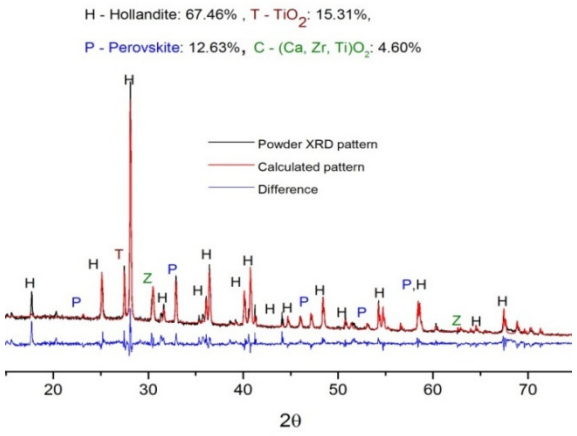

Figure 3-11. Rietveld quantitative XRD analysis of CAF-MP at 1285°C/12h

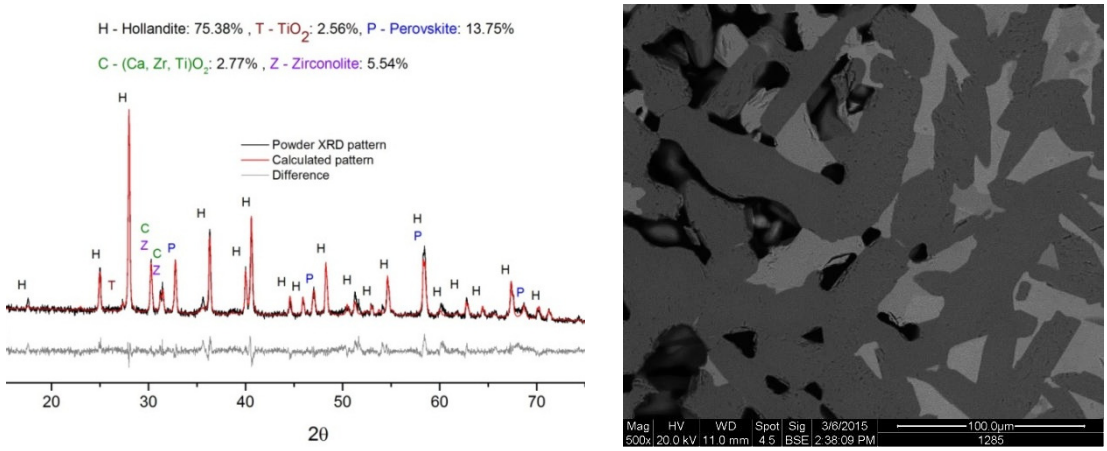

(a) (b)

Figure 3-12. (a) Rietveld quantitative XRD analysis and (b) BSE of CAF-MP at 1285°C/24h

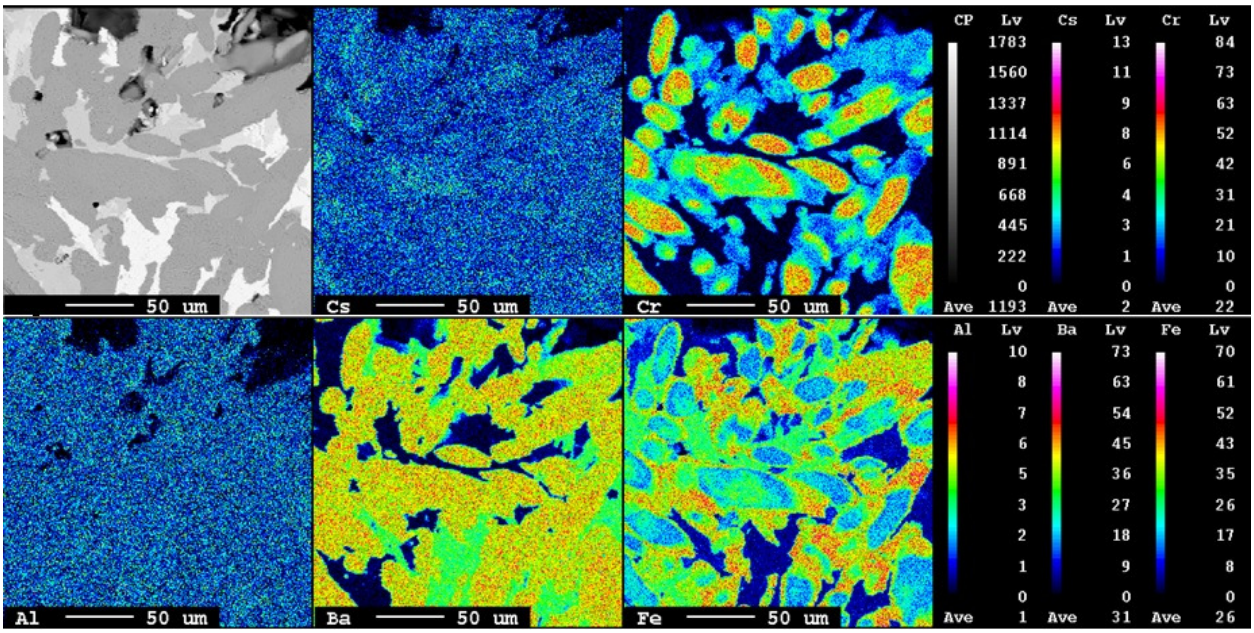

Figure 3-13. WDS maps of selected elements of CAF-MP at 1285°C/24h

3.5 Discussions on Microstructure Evolution

Multiple trials of quenching experiments and XRD characterization indicated that CAF-MP, when quenched from 1500°C has TiO_2, hollandite, and $(Ca,Zr,Ti)O_2$ as major phases with little to none amorphous phase. This suggests that hollandite phase could have formed during the heating cycle, remained in

crystalline form at melting temperatures, and on cooling, other phases nucleated from the liquid. An earlier study [70] under the same project has reported the nucleation of (Ba,Cr)-hollandite at temperatures as low as 900°C during the heating cycle. WDS elemental maps (Figure 3-5 and Figure 3-9) corresponding to hollandite grains show that the center of the grain is rich in 'Cr' compared to the edges. It can be inferred that, during melt processing of CAF-MP, nucleation of (Ba,Cr)-hollandite occurs during heating cycle and then continues to grow.

An interesting feature in the growth of hollandite grains is the compositional gradient of the trivalent cations (Cr, Al and Fe) across the grains. The main reason of adding Fe_2O_3 and Al_2O_3 to multiphase waste form composition is to lower its melting point by forming low melting hollandites like (Ba,Fe)-hollandite and/or (Ba,Al)-hollandite. As can be seen by comparing Cr and Fe elemental maps in Figure 3-9 and Figure 3-13, hollandite rich in Fe is stabilized only at lower temperature (1285°C). High concentration rings of Fe along the edges of different hollandite grains and drop in Cr intensity towards the edges can be seen. No significant trend is observed in Al distribution. In other words, it can be said that (Ba,Fe)-hollandite grows on the existing (Ba,Cr)-hollandite nuclei (grains) at lower temperatures during the cooling cycle. However, no significant changes in Cs distribution with hollandite growth can be seen from these WDS maps.

Nucleation of perovskite at 1325°C is evident from XRD data (Figure 3-7). BSE images in Figure 3-6, 3-7, and 3-8 are labeled indicating perovskite and $(Ca,Zr,Ti)O_2$ phases. These phases are indexed as such based on WDS elemental maps. Zr rich areas can be seen distinctively in Figure 3-9. Ca can be observed to have similar distribution in areas other than TiO_2 and hollandite. Hence, the bright phase, depleted in Zr is thought to be perovskite. It is not conclusive whether the Ca and Zr rich phase, $(Ca,Zr,Ti)O_2$, at 1500°C and lower temperatures has similar structure or chemistry. The ambiguity arises from the challenge in identifying this phase is also due to the possibility of presence of multiple phases for the same chemistry (Ca, Zr, Ti and O) at similar 2θ positions during XRD analysis.

The samples quenched from different temperatures with holding times of 1h had significantly higher amount of TiO_2. This is unreacted TiO_2 that would transform and grow into any of the existing phases at that temperature. Given enough time, the reaction would be complete, as evident from XRD data presented in Figure 3-6 to 3-8 and Figure 3-10 to 3-12. Corresponding BSE images also show the significant grain growth of hollandite phase.

To advance a better understanding of this nucleation and growth process with time, BSE images of CAF-MP quenched from 1285°C with different holding times are compared in Figure 3-14. Lower magnification images show 'grouping' TiO_2 grains that would coalesce with time and simultaneously transform to other phases.

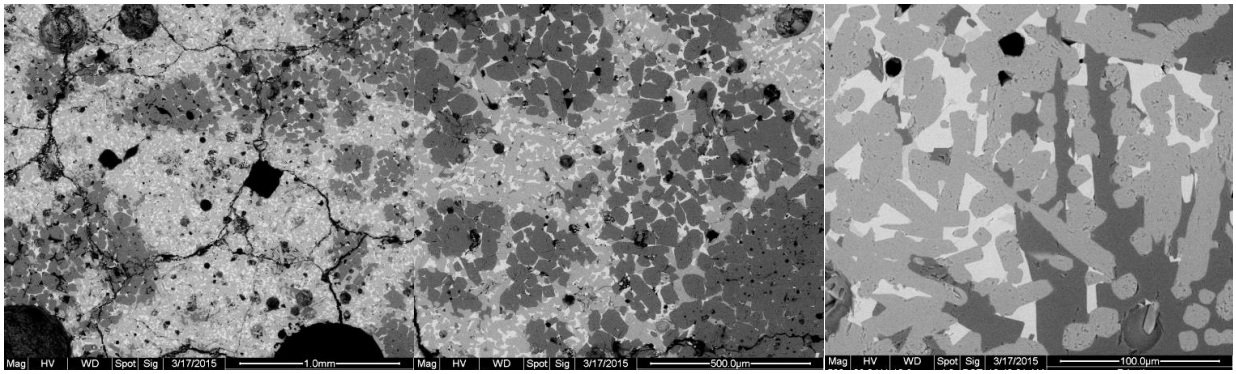

(a) (b) (c)

Figure 3-14. BSE images of CAF-MP held at 1285°C/1h (a) 50× (b) 100× (c) 500× (Dark gray phase corresponds to TiO_2, medium gray phase is hollandite and the bright colored matrix has perovskite and other Zr rich phases)

3.6 Sequence of Phase Transformations

Figure 3-15 shows the variation in relative amounts of different phases with annealing time/temperature is plotted. It could be seen that similar phase equilibrium attained at either temperature 1325°C or 1285°C: 70-75% hollandite, 12-15% perovskite and 10-15% (Ca,Zr,Ti)O_2/zirconolite. WDS elemental maps support our interpretations. Elemental maps corresponding to Cr and Fe show the non-uniform growth of hollandite as a function of temperature. (Ba, Fe)-hollandite stabilized at lower temperatures (1285°C). Figure 3-16 shows a flow chart that explains the phase transformation behavior during the melt processing of CAF-MP.

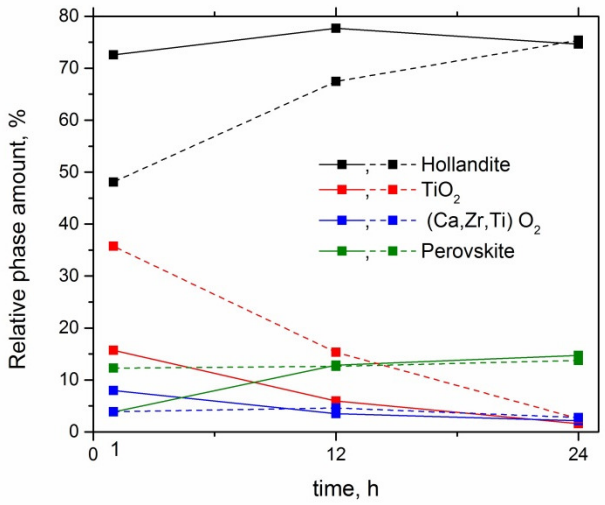

Figure 3-15. Variation of relative phase amounts with annealing time. Thick lines correspond to 1325°C and dotted lines to 1285°C.

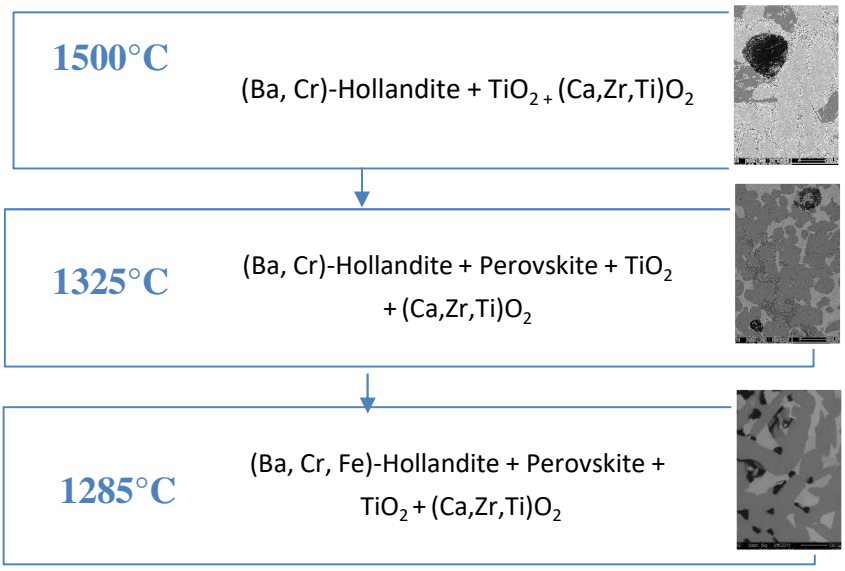

Figure 3-16. Sequence of phase transformations in CAF-MP while cooling from melting temperature

3.7 Conclusions

Our results show that the hollandite phase nucleates during the heating cycle before the maximum temperature is reached and then continues to grow. The structure of (Ca, Zr)-rich phase, indicated as $(Ca,Zr,Ti)O_2$, could not be identified within the limitations of the present dataset. Perovskite phase nucleate at 1325°C during cooling part of the processing cycle. Quantitative XRD data show that all unreacted TiO_2 transform into existing stable phases like hollandite or perovskite with prolonged heat treatment through the melt processing.

4) Simulated Radiation Damage of Titanate Multiphase Ceramic Waste Forms (Task 6)

Major sources of radiation during storage of waste forms are α- and β-decay of waste ions. Atomic displacements are mainly generated during α-decay events, which occur during the decay of actinides. These displacements can cause atomic-scale rearrangements, which lead to both physical and chemical property alteration, making the analysis of these events of critical importance. An α-decay event consists of the release of an α-particle (light particle) and an α-recoil nucleus (heavy particle). Actinides and their daughter products have long half-lives and therefore α-decay becomes dominant over long time scales. This necessitates the need to use ion implantation techniques to study the effects of α-decay on a laboratory time scale.

The α-particles and recoil nuclei interact with materials in different ways. The α-particles transfer their energy to electrons through ionization and electronic excitations and deposit their remaining energy

by engaging in ballistic processes at the end of their track (16 to 22 µm). In contrast, α-recoil nuclei lose nearly all their energy in ballistic processes over a considerably shorter range of 30 to 40 nm. The α-recoils produce several thousand displacements in a localized area while α-particles generate several hundred displacements during their longer travel [71]. It is important to study these differing damage mechanisms. This is accomplished by using He^+ ions to simulate α-particles and heavy ions, such as Au^{3+}, to simulate α-recoils.

The use of charged particle implantation has been widely utilized to study single phase crystalline ceramic waste forms [39-40, 72]. The amorphization of zirconolite, pyrochlore, and Nd-doped perovskite has been studied using of GIXRD and TEM. Few studies have been performed on multiphase crystalline ceramics for nuclear waste immobilization applications [73]. One study irradiated multiphase ceramic samples consisting of perovskite, zirconolite, and powellite with He and Kr ions to test their radiation stability. Little change to the material was seen via GIXRD after He irradiation, but amorphization occurs after heavy ion irradiation. TEM revealed amorphization of the perovskite phase, while the remaining phases remained crystalline. In the present paper, we report our results on the effects of radiation damage of multiphase titanate-based simulated waste forms (containing hollandite, perovskite, and zirconium-rich phases) produced by SPS and melt-processing and compare the radiation resistance of these samples on irradiation with light (He^+) as well as heavy (Au^{3+}) ions using GIXRD and TEM.

Samples for ion irradiation experiments were polished down to 1 µm using a diamond suspension. The experiments were carried out at room temperature at the Environmental Molecular Sciences Laboratory (EMSL), Pacific Northwest National Laboratory (PNNL) and at the Ion Beam Materials Lab (IBML), Los Alamos National Laboratory (LANL). 7 MeV Au^{3+} implantations were performed at EMSL on a National Electrostatics Corporation (NEC) model 9SDH-2 3.4 MV tandem accelerator [74] simulating three damage levels in SPS samples: 0.05, 0.5 and 5 displacements per atom (dpa) and 5 dpa in melt-processed samples. These levels were chosen to simulate varying levels of storage times, from roughly 10^2-10^6 years [75]. The implanted area was 6 × 6 mm for both melt-processed and SPS samples. A 200 kV Danfysik high current ion implanter was used to generate 200 keV He^+ ions at IBML.

The radiation dose in these materials was estimated using the Stopping and Range of Ions in Matter (SRIM) program [76]. The dpa as a function of depth for CAF-MP (similar results are obtained for Cr-MP) using 7 MeV Au^{3+} and 200 keV He^+ is shown in Figure 4-1. The peak in dpa (5, 0.5 or 0.05) is located at 870 nm (Au^{3+}) and 700 nm (He^+), while the Au^{3+} ions damage up to 1.5 µm into the material. The dpa is adjusted by changing the fluence of the incoming gold ions (ions/cm^2).

GIXRD was performed on the implanted samples using a grazing angle of 2° on the EMSL samples and 1° for the LANL (He^+) samples with a Bruker AXS D8 Advance (Bruker, Massachusetts, USA) instrument using Cu Kα radiation in theta – 2 theta geometry. The unirradiated areas of the Au^{3+} samples were ground off prior to measurement. Damaged cross-section specimens were prepared for TEM by using the lift-out method with a FIB. The damaged areas were examined using a FEI Tecnai F20 TEM operating at 200 kV.

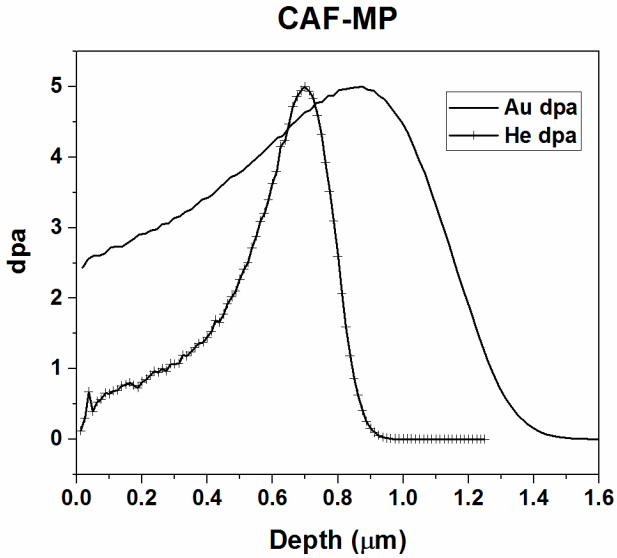

Figure 4-1. Damage profile in CAF-MP using 7 MeV Au^{3+} and 200 keV He^{+} ions

Figure 4-2 shows the GIXRD patterns of CAF- and Cr-MP samples prepared using SPS and melt-processing subjected to 7 MeV Au^{3+} at a fluence corresponding to 5 dpa. All samples show amorphization evidenced by a decrease in intensity of the peaks and the presence of diffuse scattering between 26 and 35 °2θ. CAF-MP samples produced by both processing routes show complete amorphization at 5 dpa, as demonstrated by the disappearance of all diffraction peaks. There is no new phase formation identified within the detectable limits of the technique. The highest intensity peaks of the major phases in Cr-MP samples are labeled in Figure 4-2. By comparing the intensity of these peaks, the TiO_2 and perovskite phases in the Cr-MP melt-processed are the least affected by the damage, indicating that the hollandite phase is more prone to heavy ion radiation damage [77].

Bright field TEM images of damaged cross-sections of both melt-processed and SPS CAF-MP samples irradiated with 7 MeV Au^{3+} to 5 dpa are shown in Figure 4-3. The corresponding selected area diffraction (SAD) patterns confirm that amorphization occurs in samples fabricated by both methods. Due to the large grain sizes in the melt-processed samples, only a hollandite grain was extracted with FIB, confirmed through indexing of the SAED pattern (space group C2/m, grain oriented in the [010] direction) and EDS (Figure 4-3). Cu is picked up by the EDS from the sample grid holder. The amorphized region in the hollandite grain is approximately 2.08 μm in depth.

In contrast, multiple grains are contained within the FIB sample of CAF-MP SPS. This is confirmed by examining the SAED pattern in the crystalline region. The pattern is unable to be indexed properly due to the interaction of the beam with multiple grains. The amorphized region of the SPS sample extends about 1.83 μm from the surface. The penetration depth of the Au^{3+} ions is greater in the melt-processed than that in the SPS fabricated sample. This is attributed to the interaction of the ions with multiple phases of various grain sizes and with the pores present in melt-processed samples. This can also be seen by looking at the interface between the crystalline and amorphous regions; the interface in the SPS sample is jagged, while

it is smooth in the melt-processed sample. The ion penetration depth in both samples is greater than that predicted by SRIM. The underestimation of Au ion penetration by SRIM has been investigated in SiC [78]. The difference in experimental vs simulated penetration depth when using 7 MeV Au ions was about 0.4 µm, due to overestimation of the stopping power of Au in the material.

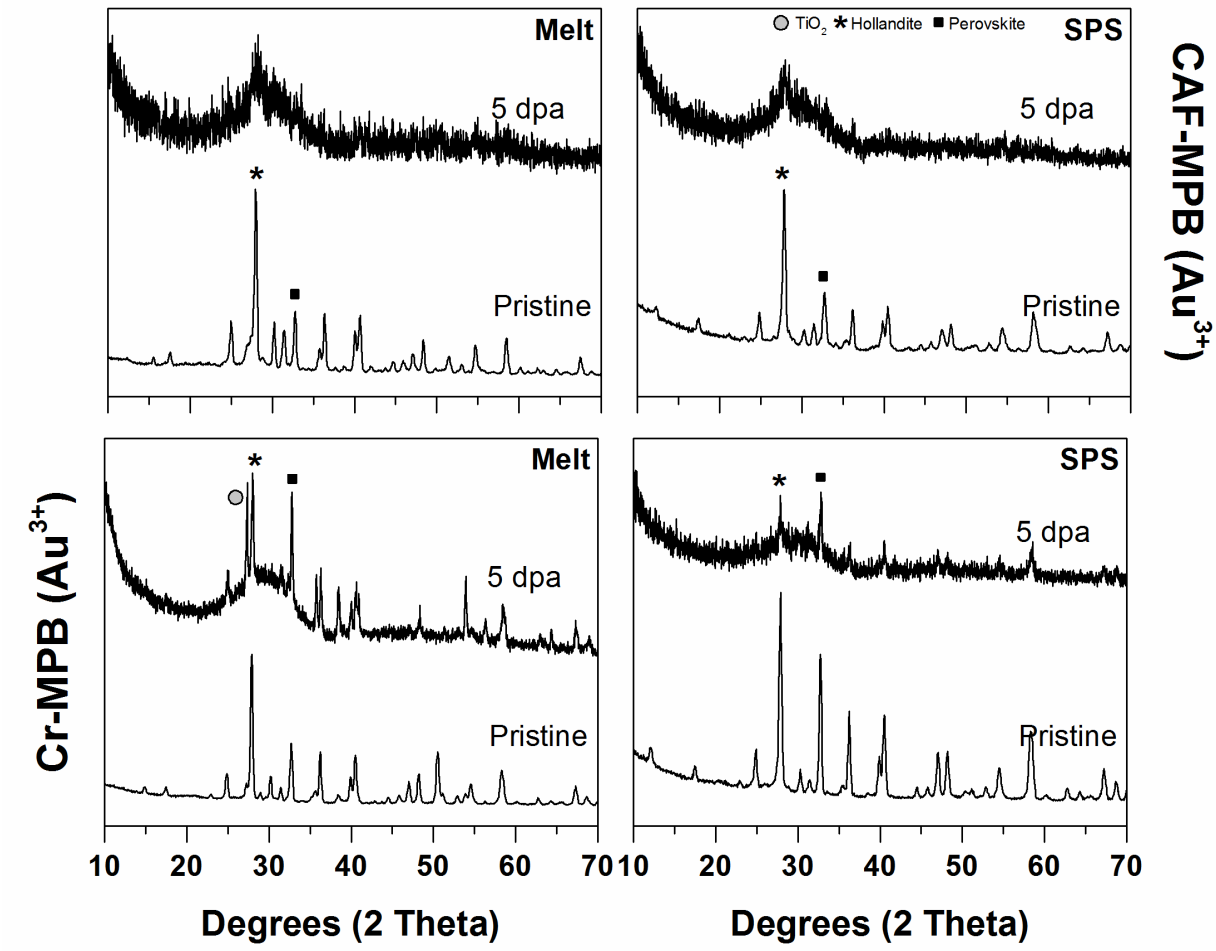

Figure 4-2. GIXRD of CAF- and Cr-MP samples fabricated by SPS and melt-processing exposed to 5 dpa of heavy ions

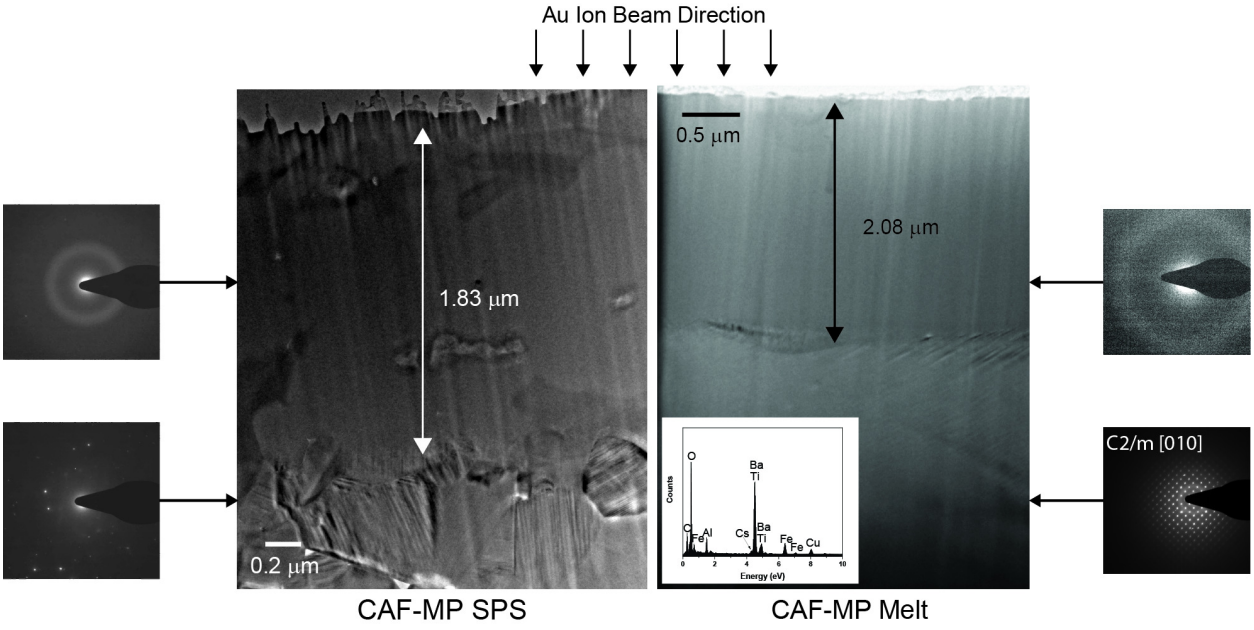

Figure 4-3. TEM images and corresponding SAD patterns of the damage cross-sections in CAF-MP materials prepared by melt-processing and SPS after exposure to 5 dpa of heavy ions

Samples fabricated by SPS were also subjected to 3 different fluences of 7 MeV Au^{3+} ions corresponding to 0.05, 0.5, and 5 dpa. Figure 4-4 shows the GIXRD patterns for CAF- and Cr-MP samples. An increase in the amorphization of the samples is seen with the increase in dpa. Little change is seen in the samples exposed to a fluence corresponding to 0.05 dpa, suggesting a threshold fluence that lies above this level. At 0.5 dpa a marked decrease in peak intensity and diffuse scattering can be seen. Complete amorphization is observed in CAF-MP compositions at 5 dpa, while Cr-MP display an increase in diffuse scattering.

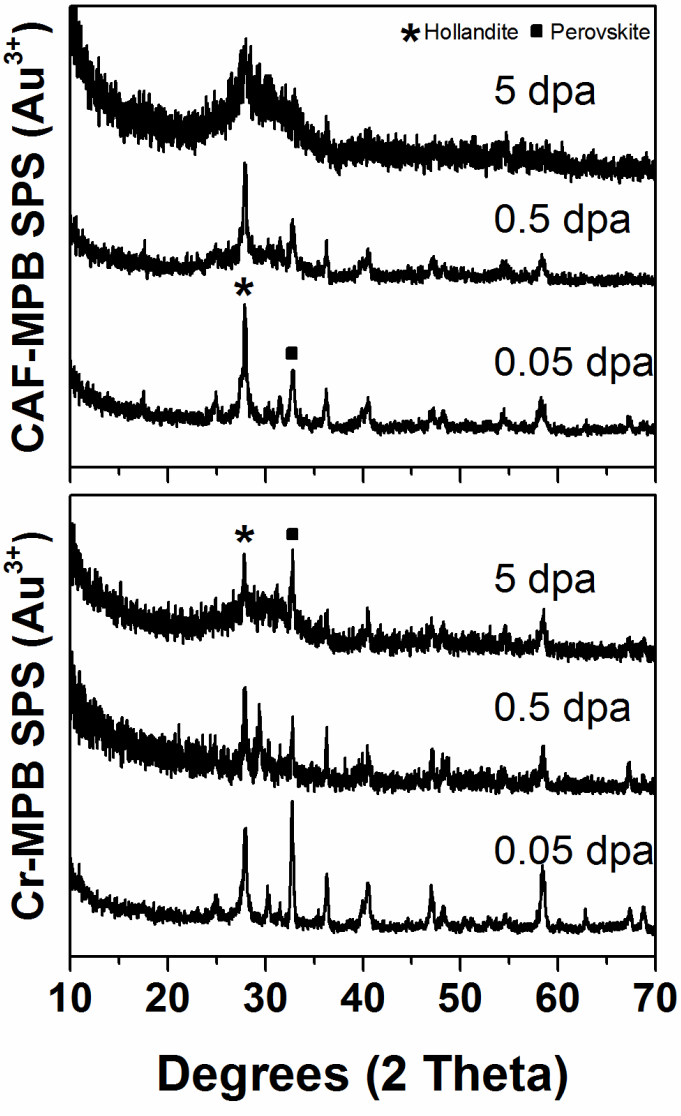

Figure 4-4. GIXRD of CAF- and Cr-MP SPS samples irradiated with 3 different damage levels

Samples of Cr- and CAF-MP consolidated by SPS were exposed to 200 keV He^+ ions. The dose of ions was equivalent to 5 dpa. Figure 4-5 compares the GIXRD results of the pristine and damaged samples. There is a large hump of diffuse scattering seen from 26 and 35 °2θ and the presence of new peaks. Some of these new peaks can be indexed to $2BaO/9TiO_2$. This, along with the disappearance of the peaks belonging to the hollandite phase, suggests that structural breakdown of the hollandite phase occurs along with amorphization under these irradiation conditions. The perovskite phase does not amorphize as severely as the hollandite phase when irradiated with He^+ ions, indicating radiation stability under light ion irradiation up to 5 dpa.

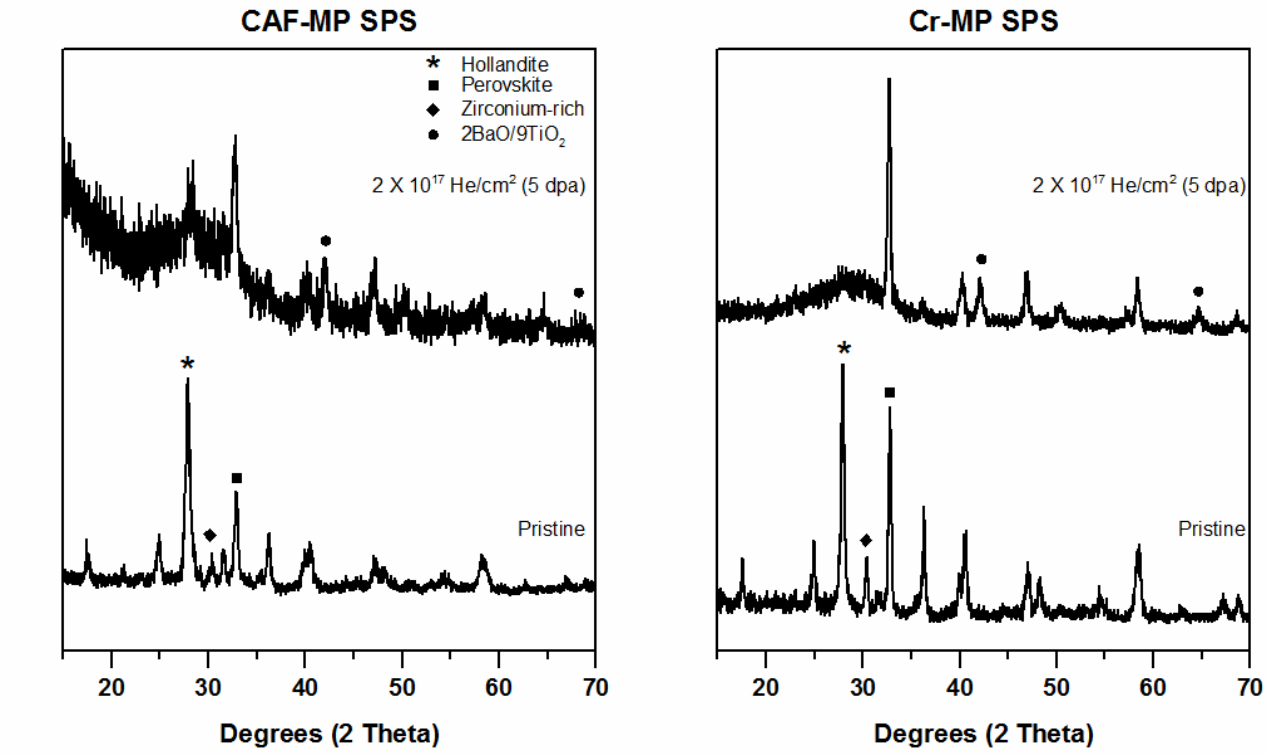

Figure 4-5. GIXRD of CAF- and Cr-MP SPS samples irradiated with He ions

In conclusion, different damage mechanisms are evident when simulating radiation damage with light and heavy ions in multiphase titanate ceramics. Heavy ions (Au^{3+}) produce amorphization through atomic displacements and is characterized by a decrease in peak intensity as well as diffuse scattering in GIXRD. Light ions (He^{+}) cause the hollandite phase in these simulated multiphase waste forms to break down. Samples fabricated by both melt-processing and SPS exhibit similar amorphization behavior when irradiated with Au^{3+} ions. The penetration depth of Au^{3+} ions is less in the CAF-MP material fabricated by SPS than those prepared by melt-processing due to a denser fine-grained microstructure and hence more grain boundary interaction.

5) Chemical Durability of Multiphase Ceramic Waste Forms (Task 6)

The chemical durability of nuclear waste form materials is of critical importance in defining the storage performance. Various test methods have been proposed for studying the leaching behavior including the Product Consistency Test (PCT) [79], the MCC standard [80], and the vapor hydration test (VHT) [81]. The leaching behavior of Cs is important to the chemical durability of multiphase waste forms due to its ability to form non-durable phases [82]. Leaching of Cs and Ba in hollandites is rapid upon initiation of the tests and then the release rate drops due to a thin passivating layer of Ti oxide [83]. Long-term leach tests have

been performed using a wide range of pH solutions and determined that pH was not a factor except at very low values (1) [84]. The leach resistance of Cr-hollandites has been shown to be superior to that of alternate hollandite compositions [85] due to the lack of secondary phase formation.

Designer waste forms (DWFs) are presented herein as a novel way to test the effect of different phase composition on the chemical durability of Cs-containing hollandite. A schematic of a DWF sample is shown in Figure 5-1. The PCT was chosen to evaluate the Cs leaching from the hollandite phase and the VHT was chosen to determine any effect a saturated, high temperature environment would have on a monolithic sample. These two tests will aid in the determination of the effects of additional phases, which contain no simulated waste ions, on the leach durability.

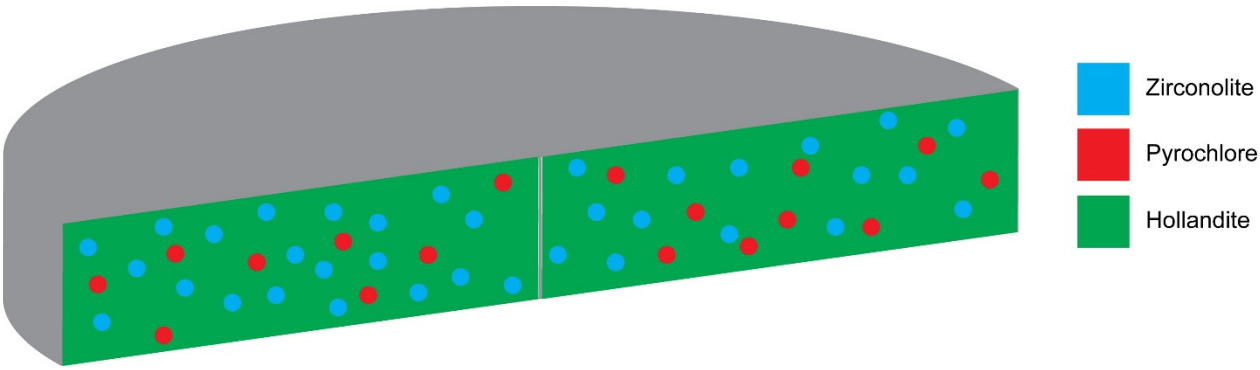

Figure 5-1. Schematic of a 'designer waste form'

Multi- and single-phase hollandite samples with metal oxide additions of Cr, Al, and Fe (designated CAF-MP, SP) and metal oxide additions of Cr (designated Cr-MP, SP) were prepared by melt-processing and SPS as described above. The microstructure and phase assemblage of CAF-MP and Cr-SP has been described previously [59]. The phase assemblage of Cr-MP is similar. The microstructures of Cr-MP samples processed by melting and SPS are displayed in Figure 5-2. For SPS samples, hollandite (H) phase forms the matrix while two perovskite (P and P') phases and zirconium-rich (Z) phases are dispersed throughout. Melt-processed samples contain dendritic hollandite (H) grains dispersed throughout TiO_2 (T), pyrochlore/zirconolite (Py/Z), and perovskite (P) phases.

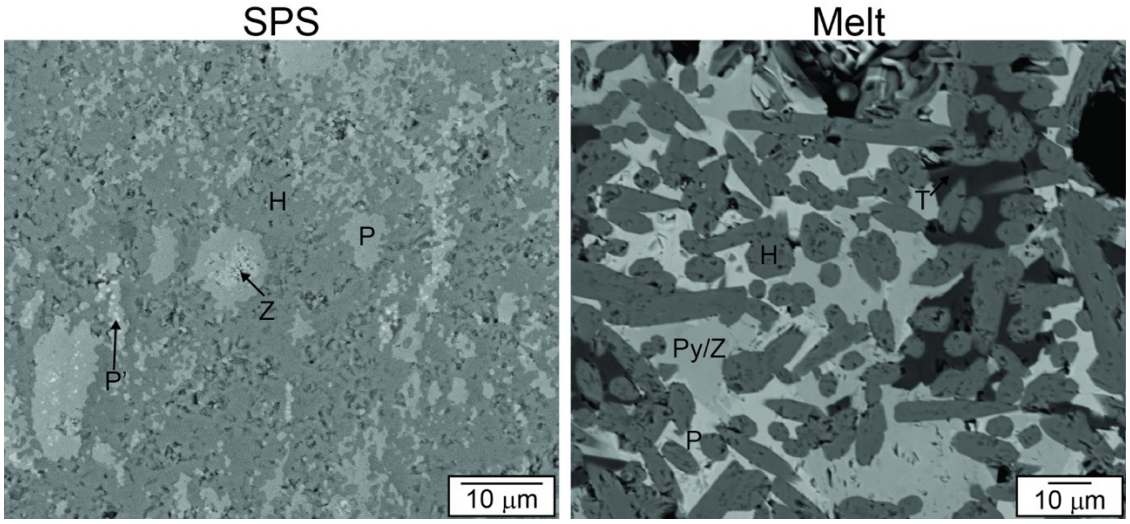

Figure 5-2. Microstructures of SPS and melt-processed simulated ceramic waste forms.

Leaching tests (using the PCT) were performed to assess the comparative Cs and Mo retention between melt-processing and SPS fabrication methods. To calculate the normalized Cs release from the DWF samples, the following equation was used:

$$NC_i = \frac{c_i(sample)}{f_i} \times \frac{5}{3} \quad (1)$$

where NC_i is the normalized release of element i, c_i is the concentration of element i in the leachate, f_i is the fraction of the element in the unleached sample and 5/3 is a dilution factor. Elemental release values of Cs and Mo from CAF-MP, SP and Cr-MP, SP is shown in Figure 5-3.

Although the material was sieved and size fractioned, the surface area affects the PCT response and the magnitude of the release rates should be carefully considered as the measurements are based on the geometric surface area of the particles tested and not the actual material surface area (e.g. porosity, voids, etc. that would increase surface area were not considered). Therefore, it is desirable to systematically study the Cs release using a highly dense multiphase ceramic. This is accomplished by using SPS to consolidate known amounts of phases into dense compacts.

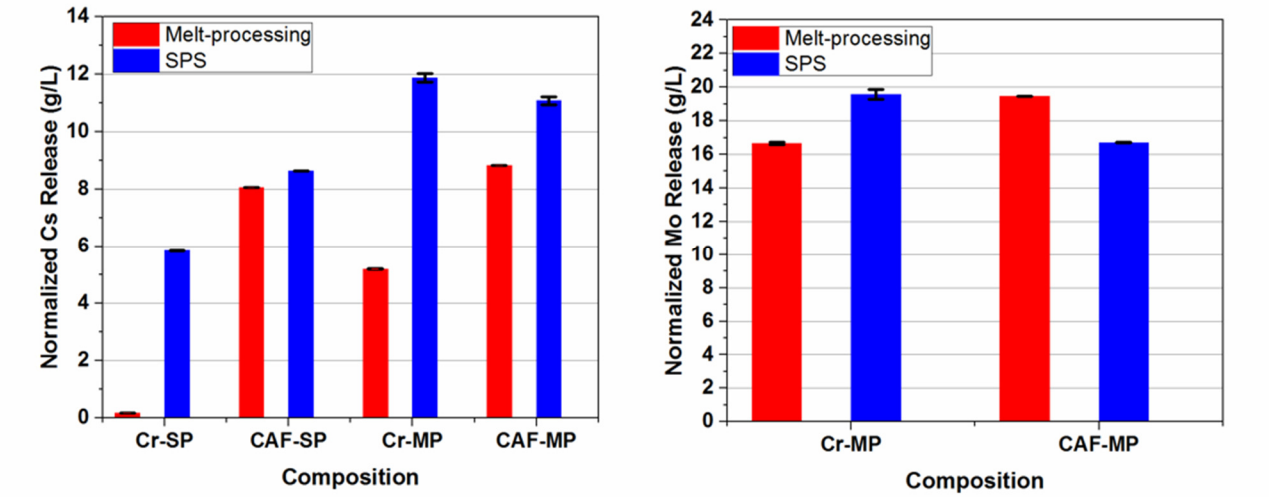

Figure 5-3. Comparison of Cs and Mo release across single phase and multiphase ceramics prepared via melt-processing and SPS

To prepare the DWF samples, varying amounts of hollandite ($Ba_{1.1}Cs_{0.1}Cr_{2.3}Ti_{5.7}O_{16}$ or $Ba_{0.9}Cs_{0.5}Cr_{2.3}Ti_{5.7}O_{16}$), zirconolite ($CaZrTi_2O_7$), and pyrochlore ($Nd_2Ti_2O_7$) produced via solid-state synthesis were consolidated by SPS. The DWF compositions are listed in Table 5-1 in volume percent. The designations 'HHC' and HLC' stand for 'hollandite high cesium' and 'hollandite low cesium' respectively corresponding to high or low cesium content in the hollandite phase. The zirconolite to pyrochlore ratio is like that found in SYNROC compositions.

Table 5-1. DWF compositions

Sample ID	**$Ba_{1.1}Cs_{0.1}Cr_{2.3}Ti_{5.7}O_{16}$**	**$CaZrTi_2O_7$**	**$Nd_2Ti_2O_7$**
80%-HLC	80	11.75	8.25
60%-HLC	60	23.5	16.5
40%-HLC	40	35	25
20%-HLC	20	47	33
	$Ba_{0.9}Cs_{0.5}Cr_{2.3}Ti_{5.7}O_{16}$	**$CaZrTi_2O_7$**	**$Nd_2Ti_2O_7$**
80%-HHC	80	11.75	8.25
60%-HHC	60	23.5	16.5
40%-HHC	40	35	25
20%-HHC	20	47	33

The sintering curves displaying the temperature and piston speed as a function of time of the HHC compositions are shown in Figure 5-4. The HLC curves are similar and are not shown. Consolidation of the materials occurs immediately prior reaching maximum temperature. The maximum temperature was slightly reduced with increasing hollandite content.

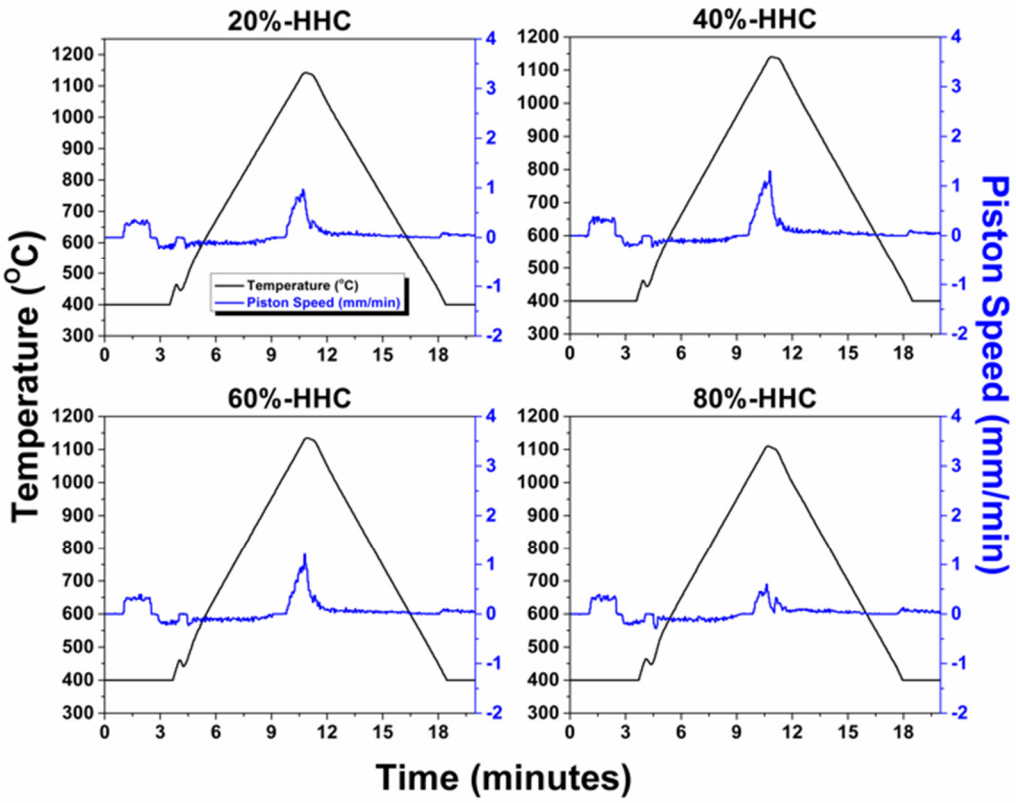

Figure 5-4. SPS densification curves of HHC DWF compositions

XRD was performed on powdered samples to determine if any interaction occurs between the phases during SPS. The patterns of HLC DWF samples are shown in Figure 5-5. Like the sintering curves, the HLC and HHC XRD patterns are nearly identical, so the additional patterns are not shown. All the peaks correspond to hollandite, zirconolite, or pyrochlore phases. The microstructure of 60%-HLC is also shown in Figure 5-5. The matrix is hollandite with islands of varying sizes of zirconolite and pyrochlore.

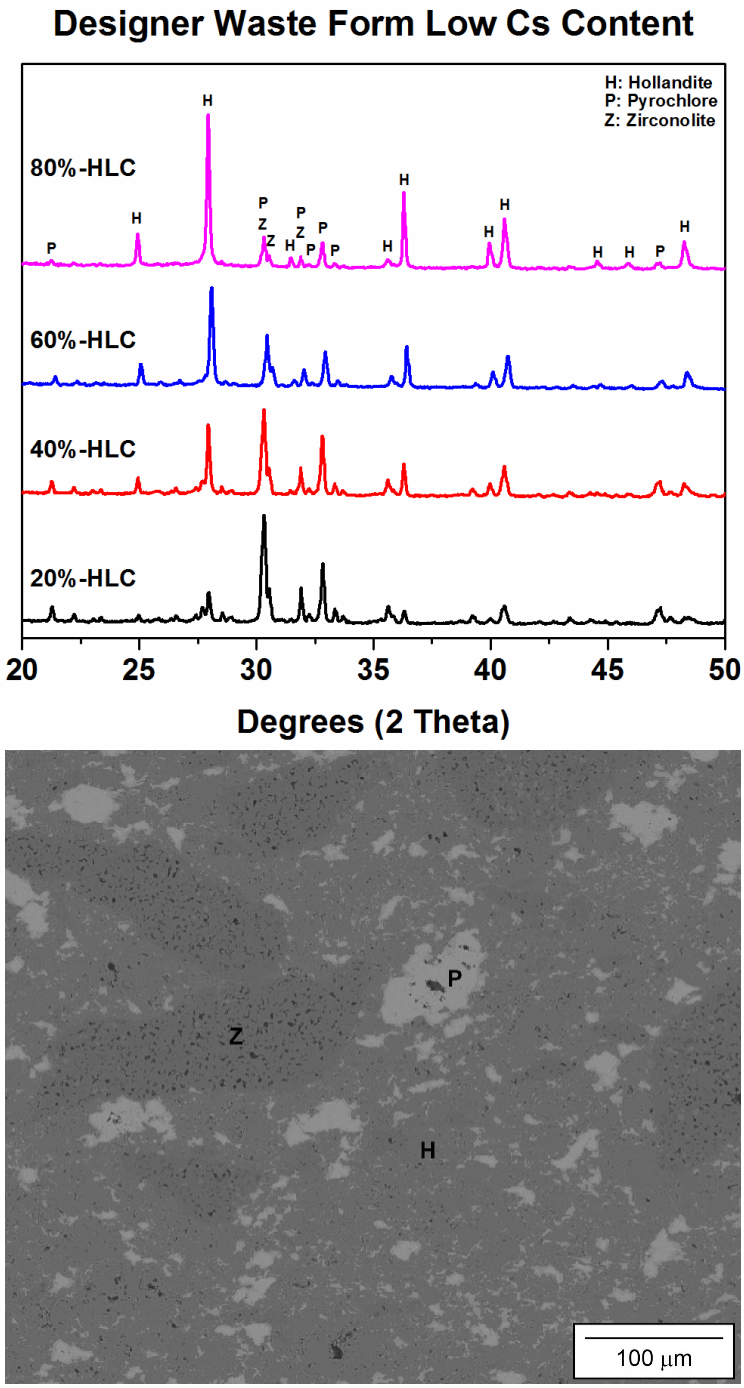

Figure 5-5. XRD patterns of HLC DWF samples and the microstructure of 60%-HLC

The PCT of these samples was performed to reveal the effect of the phase composition of a material on the Cs leaching from the hollandite phase. As in the case of the simulated multiphase waste forms, the

Cs release was normalized to the amount of Cs present in the samples prior to testing. Normalized Cs release from the samples is presented in Figure 5-6 as a function of hollandite content. The normalized release decreases as the amount of hollandite increases.

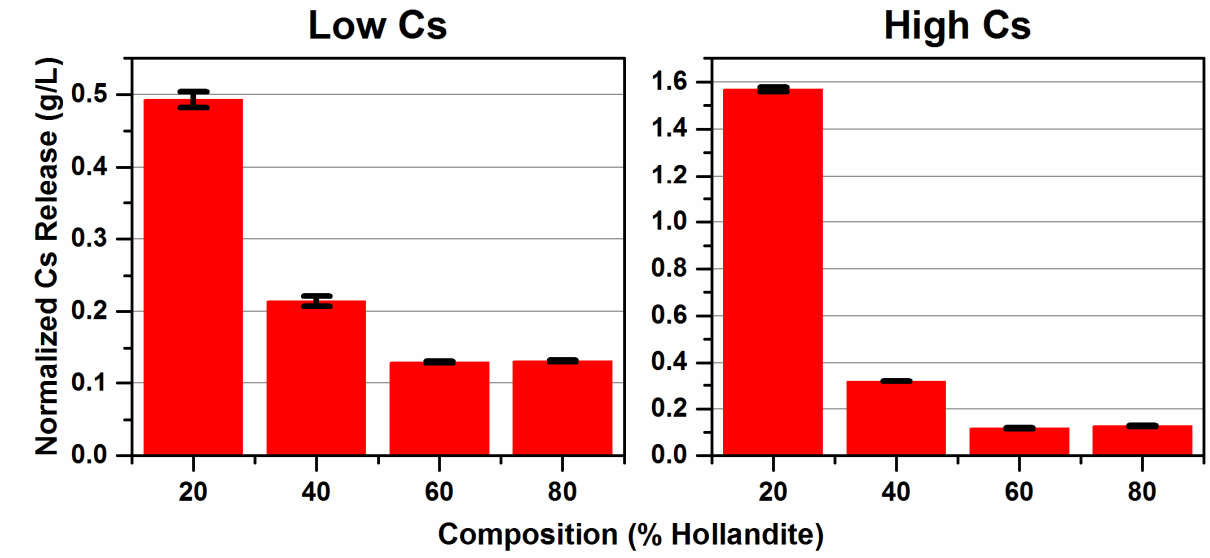

Figure 5-6. Normalized Cs realease from both low and high Cs containing hollandite DWF compositions

VHT was also conducted on HLC compositions to determine waste form behavior at elevated temperature in a saturated atmosphere. After 1500 h at 200°C, the sample surfaces appeared to be visually unaffected. XRD data show one peak belonging to Pt developed during testing. SEM along with EDS line scans were used to determine if any damage had been done to and if any elemental diffusion had occurred. An EDS line scan through the hollandite phase in the 80%-HLC sample and the corresponding SEM image are shown in Figure 5-7. No damage to the sample surface could be seen by SEM. EDS line scans were performed ~12-15 μm from the surface into the sample. No elemental diffusion was detected.

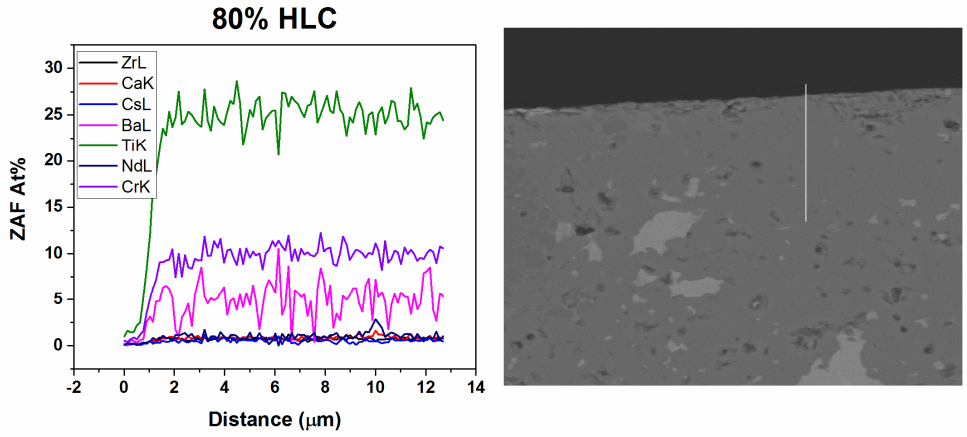

Figure 5-7. EDS line scans results from the hollandite phase of the 80%-HLC DWF sample

Of significance is the trend that SPS samples exhibit a greater Cs release compared to the melt processed samples, indicating that melt processing results in a more chemically durable product. It should be noted that the Cs and Mo releases are normalized to the measured composition, so volatilization of species would not affect the results. The Mo release rates were comparable for the two multiphase samples, suggesting that Cs-Mo contacting compounds were suppressed supporting previous results. However, the relative high release of Mo also indicates the Mo partitions to a relatively non-durable phase of the waste form.

The XRD and SEM reveal that little to no interaction occurs between the three phases during SPS of DWF compositions. This demonstrates the practicality of SPS to consolidate multiple phases into a monolithic sample with limited interaction among different phases and practically no change in morphology or phase assemblage.

The normalized Cs release decreases as the amount of hollandite in the DWF increases. We attribute this trend to high chemical resistance of the hollandite phase. The Cs release remains low and about the same in all these samples. Therefore, the Cs release appears to be decreasing with increasing hollandite content. Our data suggests that other phases in a multiphase ceramic waste form have little effect on the leaching of a specific phase.

The stability of these materials under saturated atmospheres at elevated temperatures has been demonstrated by VHT. The surfaces of each sample were examined with SEM. No alterations were detected. Each of the three phases were scanned with EDS to determine if elemental diffusion had occurred. No changes to any of the phases were detected in any of the four samples subjected to VHT. It should be noted that both C and O are removed from the EDS results. Attempts were made to detect Cs with EDS, however, The Cs peak partially overlaps with that of Ti, making it difficult to detect.

6) Cerium Substitution in Zirconolite and Pyrochlore Materials (Task 5)

Zirconolite ($CaZrTi_2O_7$) materials are potential crystalline phase host materials for both tri- and tetravalent actinides, either as single phase waste forms or as part of a multiphase assemblage [5c, 30, 32, 86]. The valence state of the substituting actinide will affect the site of substitution as well as the quantity of the ion (waste loading) that can be incorporated. Therefore, this information is critical for the informed design of waste forms.

Cerium oxide is used as a surrogate material for plutonium oxide (and other actinide elements) in simulated nuclear waste forms due to the similar electronic structure, ionic size and multiple valence states of both Ce and Pu. Both Ce and Pu can form tetravalent oxides with a fluorite structure and a trivalent phosphate with a monazite structure when heated in air between temperatures of 1000-1400°C [87], demonstrating similar reduction potential of the two elements even in an oxidizing atmosphere; however, it should be noted that the propensity to reduce is higher for Ce. Cerium oxide has been deemed as a 'suitable' surrogate for plutonium oxide by researchers based on the similar sintering behavior and phase assemblages during reaction [88].

The incorporation of Ce into zirconolite materials has been studied previously. Vance and coworkers [31] synthesized zirconolite materials in a reducing atmosphere and found that Ce could be successfully substituted onto the calcium site as a trivalent ion in small quantities, $Ca_{0.8}Ce_{0.2}ZrTi_{1.8}Al_{0.2}O_7$, when using aluminum as a compensating ion. When tetravalent Ce was targeted on the zirconium site

($CaZr_{0.8}Ce_{0.2}Ti_2O_7$), two zirconolites were reported to be formed, with one polymorph containing most the Ce. No valence data was reported.

In 1997, Begg [89] reported formation of two zirconolites when targeting tetravalent Ce on the zirconium site ($CaZr_{0.8}Ce_{0.2}Ti_2O_7$). The synthesis of these materials was performed in air as opposed to the reducing atmosphere used in Vance's experiments. The new zirconolite phase that was formed belonged to the 4M (monoclinic) polymorph as opposed to the 2M polymorph.

2M-ziconolite has been described by Rossel [90] as having an anion deficient fluorite structure with layers of corner sharing TiO_6 octahedra that are separated by layers containing ZrO_7 and CaO_8 polyhedra. This polymorph forms with compositions of $CaZr_xTi_{3-x}O_7$ with $0.8 < x < 1.37$. The 4M-zirconolite is described by Coelho [91] as having an enlarged unit cell (~22Å compared to ~11Å of 2M) due to the cation occupancy. There are two full occupancy Ti sites in the 2M structure, opposed to only one full occupancy Ti site in the 4M structure, requiring a doubling of the c axis to accommodate. The 4M zirconolite is formed when cations (such as Nd used by Coelho) substitutes on both the calcium and zirconium sites simultaneously with 0.5-0.8 formula units creating an alternate layering of the structure. The structures are compared in Figure 6-1.

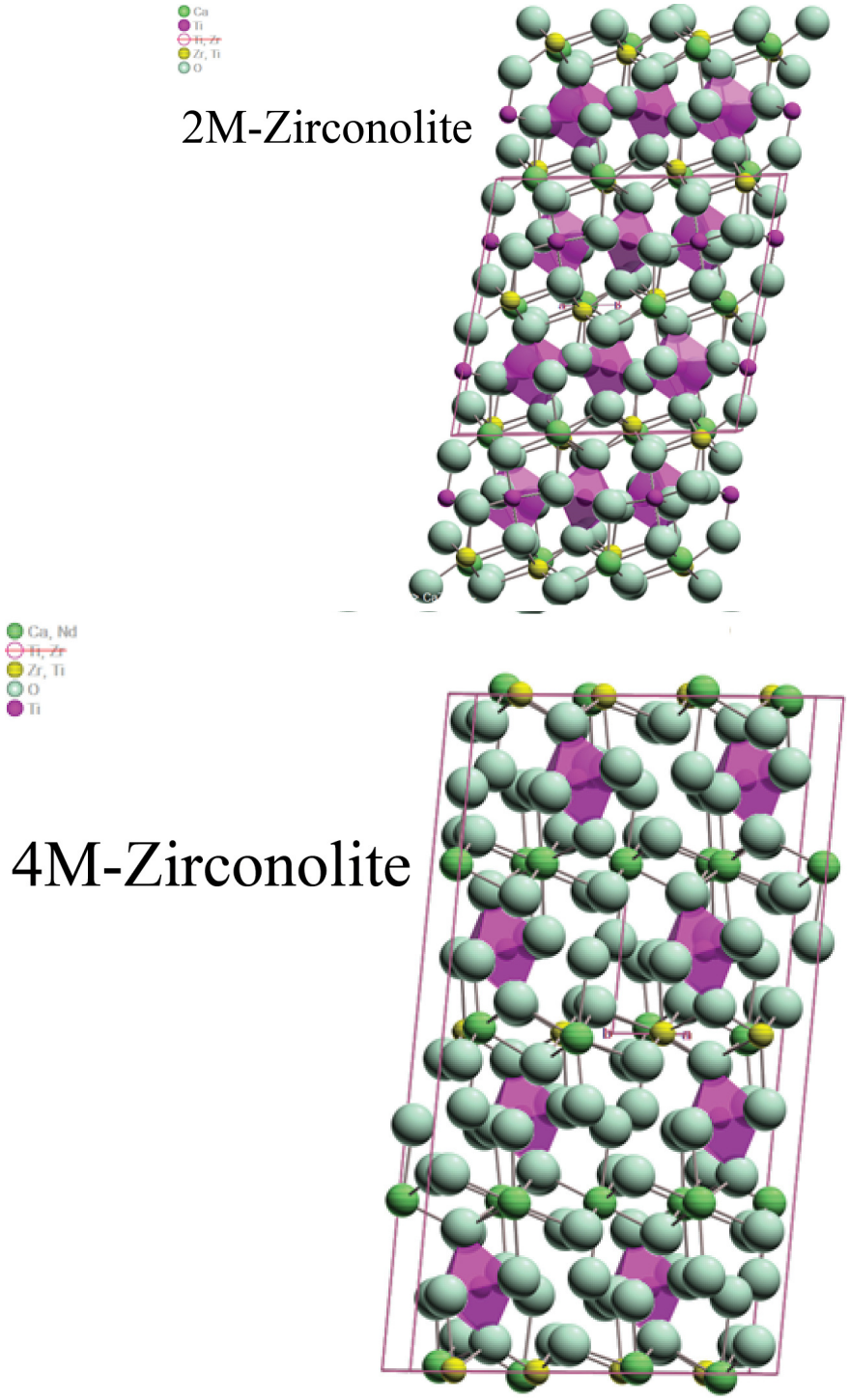

Figure 6-1. Structures of 2M zirconolite (Top) and 4M zirconolite (Bottom)

Solid-state synthesis of $CaZr_{1-x}Ce_xTi_2O_7$ and $Nd_{2-x}Ce_xTi_2O_7$ materials was performed. High purity oxide precursors of CaO, ZrO_2, Nd_2O_3, TiO_2 and CeO_2 (Alfa Aesar) were used in the experiments. The milling procedures for the zirconolite and pyrochlore materials were different due to the slow reaction rate of the zirconolite.

For zirconolite materials, the formula $CaZr_{1-x}Ce_xTi_2O_7$ was used with x = 0.1-0.5. The appropriate amount of precursor material was weighed and placed in a ZrO_2 milling jar with 2 mm YSZ milling media (Across International). The precursors were milled at 1,200 rpm using a mixture of ethanol and water as the milling medium in a VQ-N High Speed Ball Mill (Across International) for 15 min. The resulting slurry was separated from the media and dried on a hot plate. The dry powders were homogenized using a mortar and pestle and pressed into 20 mm diameter pellets using a hydraulic press and a steel die. The pellets were reacted in a furnace at 1375°C for 72 h, crushed into powder, milled for 5 min using the same procedure, dried and homogenized.

For pyrochlore materials, the formula $Nd_{2-x}Ce_xTi_2O_7$ with x = 0.1-0.5 was used. The weighed-out precursor powders were placed in a high-density polyethylene (HDPE) jar with 1/4 inch spherical alumina media and ethanol/water mixture. Milling was performed for one hour. The media was removed from the slurry and the slurry was dried. The powders were homogenized and pressed into pellets as above. The pellets were reacted in a furnace at 1400°C for 24 h, crushed, pelletized and reacted a second time at 1400°C for 24 h. The resulting pellets were crushed and homogenized for characterization. The synthesized powders were analysed using XRD (D2 Phaser, Bruker, Massachusetts, USA) for phase identification.

Figure 6-2 shows the XRD patterns of zirconolite samples with Ce substitution from x=0-0.5, targeting the zirconium site. The amount of 4M-zirconolite (compared to 2M-zirconolite) is seen to increase with greater Ce content. Rietveld analysis confirms this trend and the results are listed in Table 6-1. By x = 0.5, the zirconolite is present in the 4M polymorph. A small amount of perovskite is also seen in all the samples. This is most likely due to the substitution of Ce on the calcium sites, making excess calcium available to react contrary to the formulation.

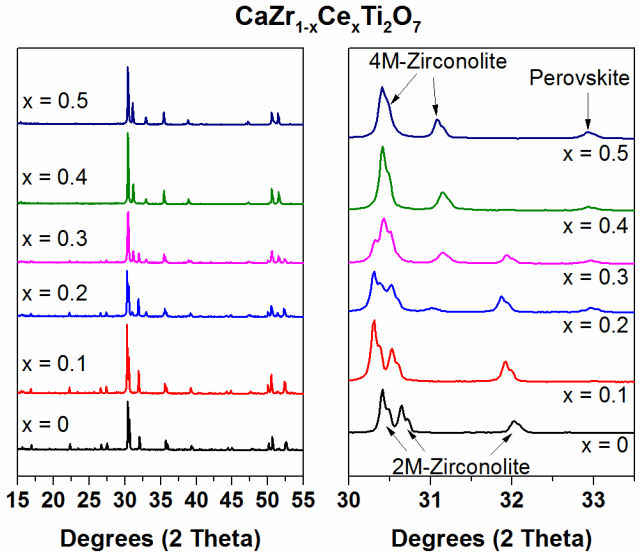

Figure 6-2. XRD patterns of Ce-zirconolites

Table 6-1. Percentages of phases present in zirconolite powder samples synthesized via solid-state sintering determined by Rietveld analysis

Sample	Zirconolite-2M	Zirconolite-4M	Perovskite
$CaZr_{0.9}Ce_{0.1}Ti_2O_7$	99.0(1) wt.%	0 wt.%	0.9(1) wt.%
$CaZr_{0.8}Ce_{0.2}Ti_2O_7$	74.5(3) wt.%	19.3(3) wt.%	6.2(1) wt.%
$CaZr_{0.7}Ce_{0.3}Ti_2O_7$	45.6(3) wt.%	49.0(3) wt.%	5.4(1) wt.%
$CaZr_{0.6}Ce_{0.4}Ti_2O_7$	3.6(3) wt.%	89.4(3) wt.%	6.9(2) wt.%
$CaZr_{0.5}Ce_{0.5}Ti_2O_7$	0 wt.%	95.6(4) wt.%	4.3(3) wt.%

A representative SEM image of synthesized $CaZr_{0.7}Ce_{0.3}Ti_2O_7$ taken in backscatter electron (BSE) mode is displayed in Figure 6-3. Two phases can clearly be distinguished and are evenly distributed, which agrees with XRD of roughly equal amounts of 2M- and 4M-zirconolite. The contrast in backscattered images suggests that the one polymorph contains a greater amount of Ce. This is confirmed with EDS, with roughly twice as much Ce content in the bright phase. The bright phase belongs to 4M-zirconolite because as the amount of substituted Ce increases, the amount of 4M-zirconolite also increases. Therefore, the darker phase belongs to 2M-zirconolite. The EDS also shows that the Ce is evenly distributed on the Ca and Zr sites in the 2M-zirconolite, while uneven splitting is seen in the 4M-zirconolite, with a greater amount partitioning on the Zr site.

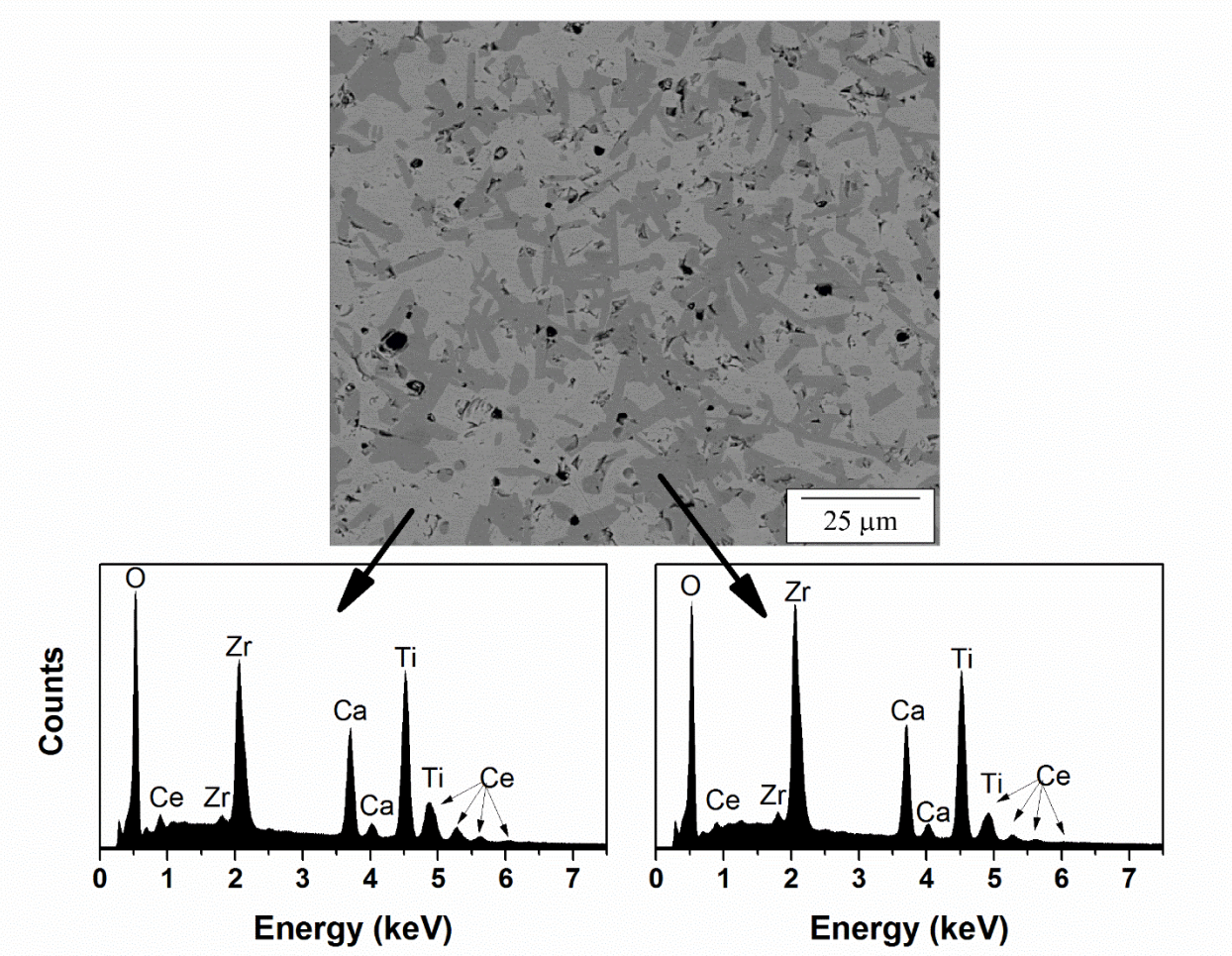

Figure 6-3. Representative BSE image of synthesized $CaZr_{0.7}Ce_{0.3}Ti_2O_7$ and corresponding EDS spectra from the two phases seen

X-ray absorption near edge spectroscopy (XANES) was performed on powdered samples of $CaZr_{0.5}Ce_{0.5}Ti_2O_7$ to detail the Ce valence state in these Ce zirconolites. The valence state of the Ce did not vary with composition. Therefore, only the x=0.5 composition results are shown. Figure 6-4 displays the XANES results from the standards, CeO_2 and $CePO_4$, and the synthesized powder. From the relationship between the edge energies, the synthesized powders contain about a 50/50 mix of tri- and tetravalent Ce. The presence of both tri- and tetravalent Ce demonstrates the ability of Ce to reduce at high temperatures in oxidizing atmospheres [89]. Trivalent Ce can co-substitute on both the Ca and Zr sites (as is seen in the 2M-zirconolite), and the tetravalent Ce can substitute for Zr (as in the 4M-zirconolite) without a need for a compensating ion. In zirconolite, this is often achieved by substituting Al for Ti [89, 92].

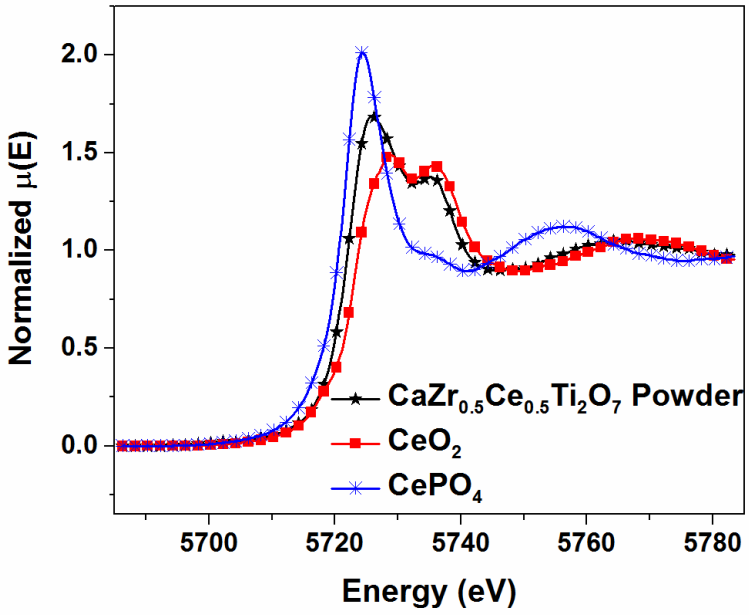

Figure 6-4. XANES results from standard materials and synthesized Ce-zirconolite powder

To consolidate the powder into monoliths, SPS was performed on the Ce-zirconolites. The sintering behavior of $CaZr_{0.9}Ce_{0.1}Ti_2O_7$ was very like single phase material, where rapid consolidation occurs immediately prior to reaching maximum temperature. XRD of the resulting pellet shows similar phases to starting powder with a small amount of perovskite phase (Figure 6-5). The sintering peak of $CaZr_{0.6}Ce_{0.4}Ti_2O_7$ was 'sharper' than the single-phase material, indicating more rapid sintering. XRD of the resulting pellet shows an increase of perovskite phase. The change in sintering behavior is attributed to the sintering of both zirconolite and perovskite. The sintering curve and XRD are also shown in Figure 6-5. The destabilization of 4M-zirconolite in favor of 2M-zirconolite after sintering should also be noted.

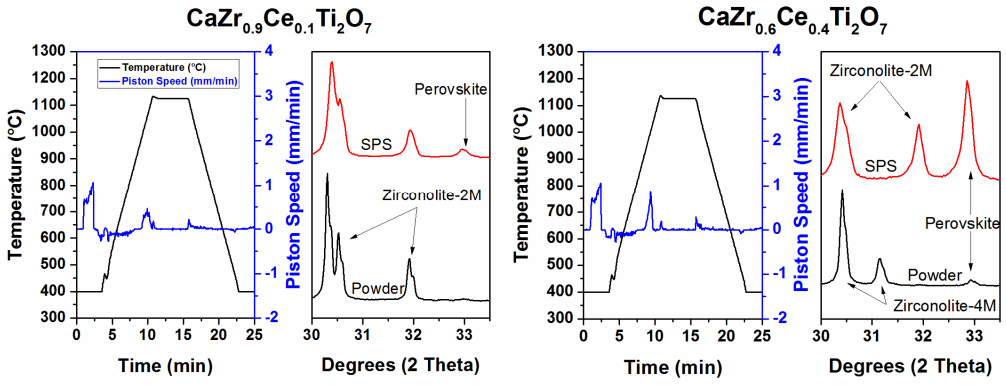

Figure 6-5. Temperature profile and piston speed during SPS of CaZr0.9Ce0.1Ti2O7 and CaZr0.6Ce0.4Ti2O7 including XRD comparison of the powder and resulting SPS pellet

This result demonstrates that the conversion to perovskite is a fast process and that it occurs below the sintering temperature of zirconolite. SPS was performed on the range of Ce-substituted zirconolites. It was found that the amount of perovskite formed during SPS increases as the amount of Ce in the material increases. A comparison of the XRD patterns of the sintered Ce-substituted zirconolites is shown in Figure 6-6. The stabilization of a perovskite phase from zirconolite in reducing conditions (as in the case of SPS) has been reported previously [31, 93]. XANES reveals that about 90% of the Ce is present in the trivalent state after SPS (Figure 6-6). Zirconolite transformation into perovskite is due to the partial reduction of Ti^{4+} to Ti^{3+} [93]. For charge compensation to occur in the zirconolite structure, Zr relocates to the Ca site, allowing excess Ca and Ti to react to form perovskite with the reduced Ce.

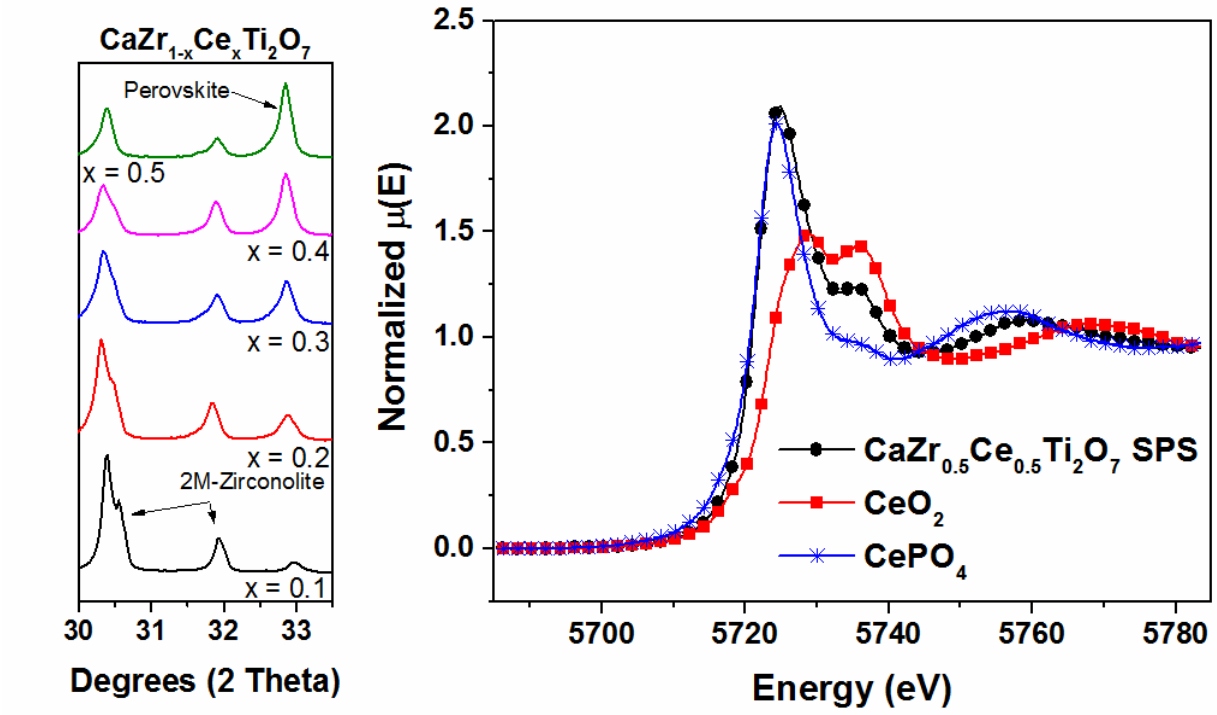

Figure 6-6. XRD comparison of SPS Ce-substituted zirconolites along with XANES results showing most trivalent Ce

The formation of perovskite during SPS is undesirable due to the superior chemical durability of zirconolite [94] compared to the perovskite phases. Thus, a heat treatment in air after SPS is required to convert the perovskite back into zirconolite. High temperature XRD (HTXRD) was used to monitor the phase conversion during heat treatment. Schedule 1 (Table 6-2) reveals that $CaCeTi_2O_7$ forms as an intermediate phase at temperatures up to 1300°C, as seen in the XRD patterns in Figure 6-7. 4M-zirconolite does not form in the $CaZr_{0.6}Ce_{0.4}Ti_2O_7$ sample during Schedule 1. No significant changes to the patterns were seen in the subsequent measurement at 1300°C.

Table 6-2. HTXRD schedules used to study phase conversion of Ce-zirconolite post-SPS

Schedule	Ramp Rate	Max Temperature	Hold Time (hr)	Scan Rate at T
1	30	1300	1	3
2	30	1350	6	2

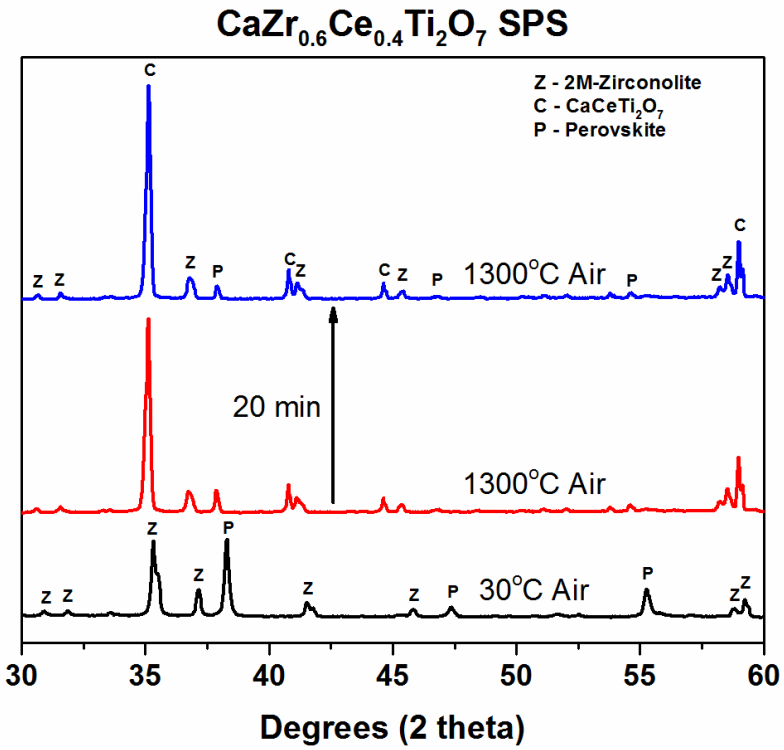

Figure 6-7. *in situ* XRD patterns of $CaZr_{0.6}Ce_{0.4}Ti_2O_7$ at 1300°C showing the conversion of perovskite into $CaCeTi_2O_7$

A second HTXRD schedule was performed to eliminate the $CaCeTi_2O_7$ that forms as an intermediate phase. At 1350°C, $CaCeTi_2O_7$ and 2M-ziconolite are converted into 4M-zirconolite (Figure 6-8). Rietveld analysis was performed on these patterns to determine the phase contents of the specimen during the 4M-zirconolite formation. Select diffraction patterns and the corresponding wt.% determined by Rietveld analysis are shown in Figure 6-8. It is seen that perovskite reacts to form $CaCeTi_2O_7$ at temperatures below 1350°C. During the 5 hour hold at 1350°C, the perovskite content reaches a plateau at around 9 wt.%. The $CaCeTi_2O_7$ and 2M-zirconolite react during the first 2 hours of the hold at 1350°C to form 4M-zirconolite which plateaus by around 3.5 hours. The reaction did not go to completion (100% 4M -zirconolite) during the HTXRD experiment.

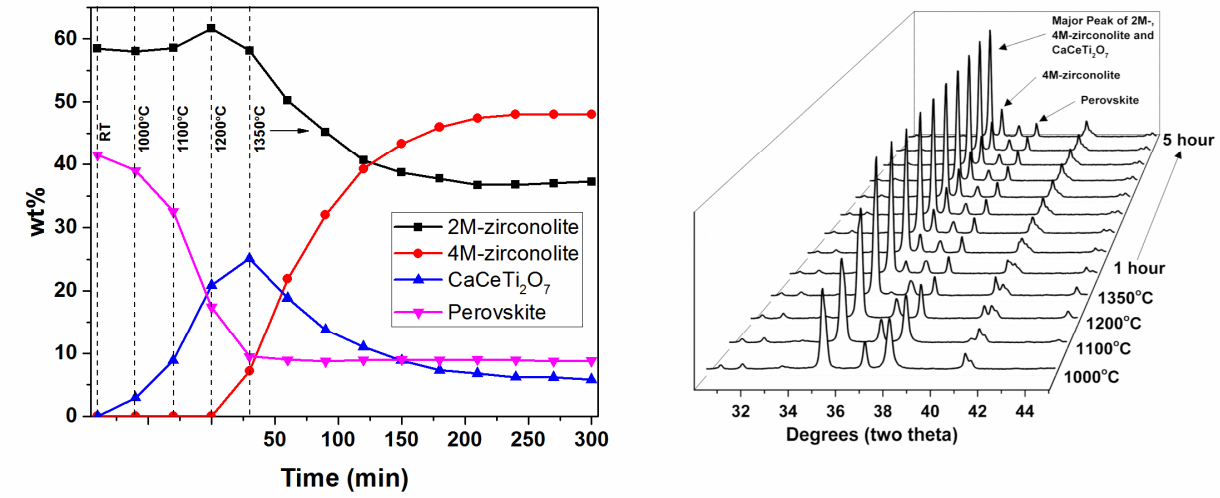

Figure 6-8. Phase amounts and corresponding XRD patterns during heating and isothermal hold at 1350°C of $CaZr_{0.6}Ce_{0.4}Ti_2O_7$

Conversion of the phases after SPS back to nearly the original phase composition was achieved by a furnace heat treatment at 1350°C for 24h. The longer heat treatment completes the conversion of $CaCeTi_2O_7$ into zirconolite (both 2M and 4M), which is desirable for the intended application. XRD patterns representing the phase changes are shown in Figure 6-9.

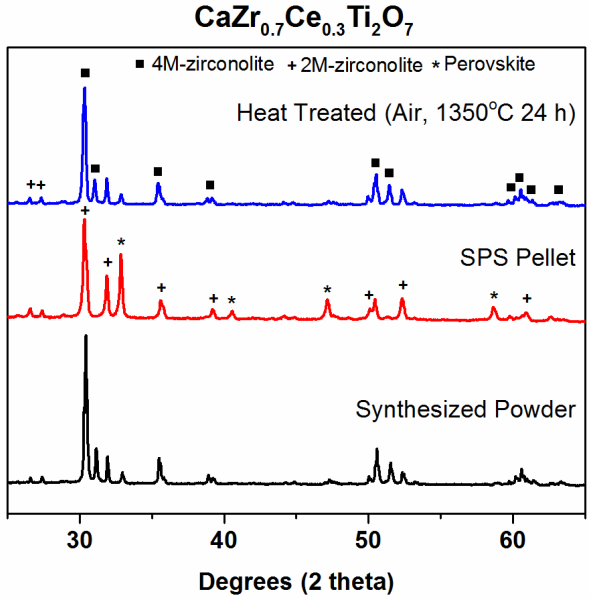

Figure 6-9. XRD patterns comparing the phase assemblage in CaZr0.7Ce0.3Ti2O7 under different processing conditions

Figure 6-10 shows the XRD patterns of Ce substituted pyrochlore. The materials remain single phase throughout the range of substitution. The substitution mechanism of Ce into this pyrochlore structure was investigated using the General Utility Lattice Program (GULP) and the results are summarized below. It was found that the most likely substitution mechanism was replacing the Nd^{3+} with Ce^{3+}. This mechanism seemed unlikely due to using CeO_2 as the Ce precursor. XANES was performed on $Nd_{1.5}Ce_{0.5}Ti_2O_7$ synthesized powders to determine the valence state of Ce in pyrochlore materials. The Ce reduces to the trivalent state during synthesis in air to fit within the structure. The XANES results are shown alongside the XRD in Figure 6-10.

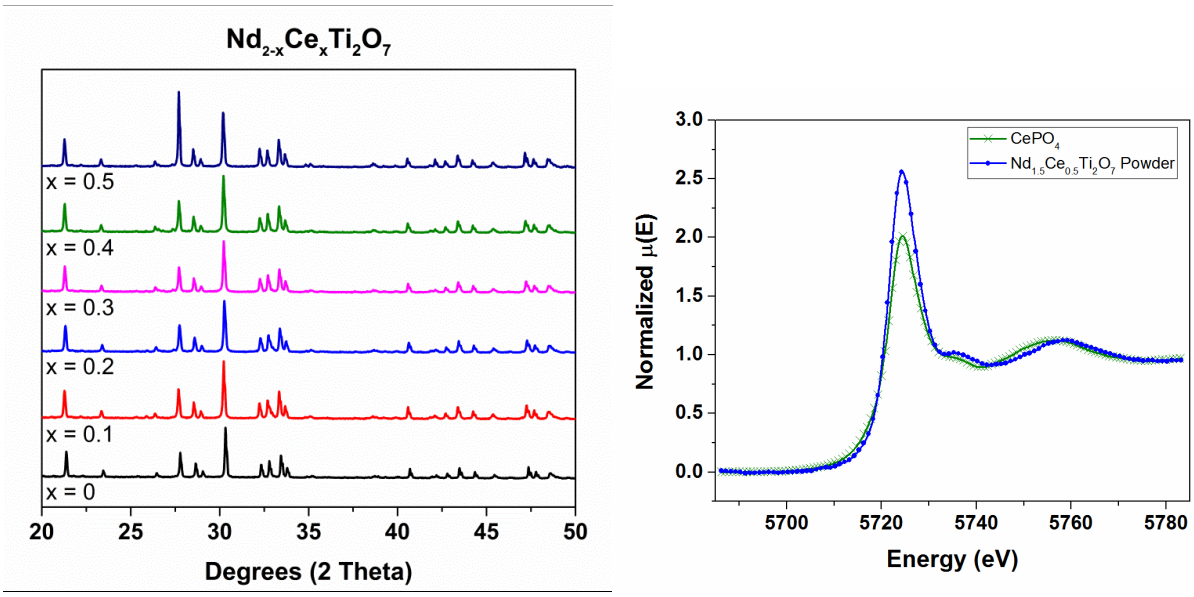

Figure 6-10. XRD patterns and XANES spectra of Ce substituted pyrochlore materials

Atomistic modeling can aid in the understanding of the Ce incorporation into materials for nuclear waste immobilization. Pyrochlore materials have been studied using different modeling methods [96]. In general, an energy minimization technique is used with Buckingham potentials to obtain a relaxed structure. One program that utilizes this technique is GULP. This program takes the internal energy (which is made up of columbic, polarizability, dispersion, etc.) and writes it as a Taylor series, calculates the derivative (g) and the second derivative (H), and uses the equation $\Delta x = -H^{-1}g$ to find the path towards the local minimum. The second derivative is in matrix form, and calculating the inverse of this matrix is the most time consuming step, and therefore is only done after a set number of calculations [97].

Defect calculations are then performed to find the defect energies of the Ce substitutions using the Mott-Littleton technique [98]. This technique utilizes two regions surrounding the defect to calculate the energy and is illustrated in Figure 6-10. The defect is in the center, or midpoint between multiple defects. Regions are specified by radii, to include an appropriate number of ions. Ions in Region I are strongly affected by the defect and are relaxed explicitly using energy minimization and force balance techniques. Ions in Region II are weakly perturbed and the atom positions are approximated. A larger Region I allows

for more complete relaxation around the defect. The defect energy is calculated by taking the difference in energy between perfect regions and the defective regions.

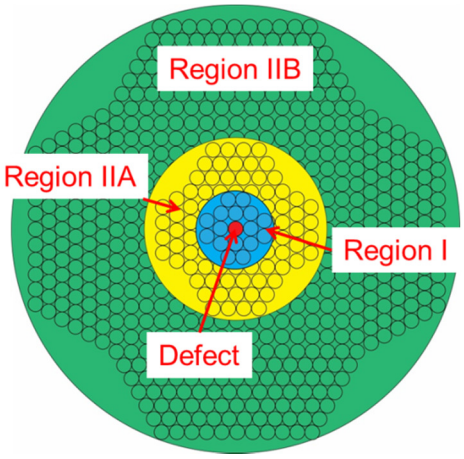

Figure 6-10. Illustration of the regions surrounding a defect in the Mott-Littleton technique

The structure was first relaxed using Buckingham potentials for the element-oxygen interactions found in the literature [99]. The values of the lattice constants and density from the literature and after relaxation using GULP are listed in Table 6-3.

Table 6-3. Values of lattice constants and densities for zirconolite and pyrochlore materials found in the literature and after structural relaxation using GULP

Property	**$Nd_2Ti_2O_7$**	
	Experimental [99]	**Calculated**
Lattice Volume (Å^3)	539.24	541.61 (4.4)
a (Å)	7.6747	7.56 (-1.5)
b (Å)	13.0025	13.21 (1.6)
c (Å)	5.640	5.47 (0.2)
β or γ (°)	98.517	98.2 (-0.3)
ρ (g/cm^3)	6.110	6.09 (-0.4)
*percent variation in parentheses		

The heat of solution was calculated by calculating the lattice energies of the structures and the energy of the defects in the equation. The lower the heat of solution, the more likely the substitution is to occur. Five possible substitution mechanisms for Ce into pyrochlore listed in Table 6-4. Note that different Buckingham potential parameters were used whether Ce was present as tri- or tetravalent. The most likely

substitutions per these defect calculations are trivalent Ce substitution on the Nd site. Defect energies were calculated for different combinations of atomic sites.

Table 6-4. Possible substitution mechanisms for Ce incorporation into Nd2Ti2O7. The highlighted rows indicate the most likely mechanisms

Substitution Mechanism	**Heat of Solution (eV)***			
$4CeO_2 \rightarrow 4Ce_{Nd} + V_{Ti} + 2Nd_2O_3 + TiO_2$	16.78	14.74	20.62	10.91
$CeO_2 \rightarrow Ce_{Ti} + TiO_2$	8.74		8.74	
$3CeO_2 \rightarrow 3Ce_{Nd} + V_{Nd} + 2Nd_2O_3$	6.59	5.85	10.25	2.183
$Ce_2O_3 \rightarrow 2Ce_{Nd} + Nd_2O_3$	2.22		-0.04	
$2CeO_2 + Al_2O_3 \rightarrow 2Ce_{Nd} + 2Al_{Ti} + 2TiO_2 + Nd_2O_3$	13.66	12.72	15.66	10.73

*various combinations of defects on atomic sites

The sintering of these materials by SPS was also investigated. No phase changes occur as a result of sintering. A blank was run to subtract the 'background' piston movement due to the graphite and foil. The sintering behavior is shown in Figure 6-11. All materials exhibit similar behavior indicating a similar sintering mechanism in play. An increase in Ce substitution did not seem to inhibit the sintering of the material.

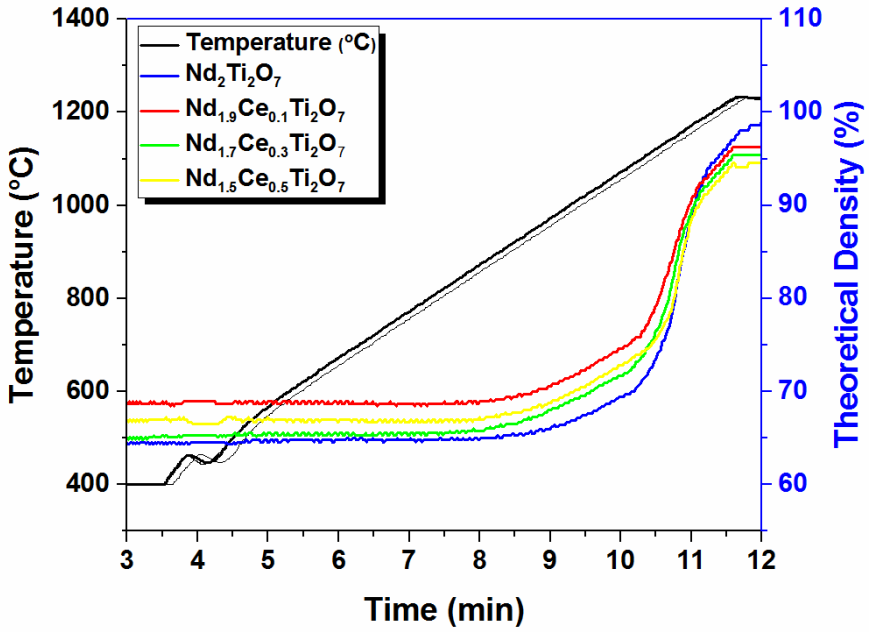

Figure 6-11. Sintering curves of Nd2-xCexTi2O7, x = 0, 0.1, 0.3, and 0.5

The sintering mechanism of $Nd_2Ti_2O_7$ was investigated using the modified hot-pressing equations proposed by Bernard-Granger and Guizard [100]. The thermodynamic driving force during sintering can be neglected due to the applied external load and the hot-pressing kinetic equation can be rewritten as:

$$\frac{1}{D}\frac{dD}{dt} = \frac{B\Phi\mu_{eff}b}{kT}\left(\frac{b}{G}\right)^{p}\left(\frac{\sigma_{eff}}{\mu_{eff}}\right)^{n} \quad (2)$$

where D is the instantaneous relative density, B is a constant, G is the grain size, Φ is the diffusion coefficient, b is the Burgers vector, k is the Boltzmann's constant, T is the absolute temperature, p is the grain size exponent, σ_{eff} is the instantaneous effective stress acting on the powder bed, μ_{eff} is the instantaneous shear modulus acting on the powder bed and n is the stress exponent.

The instantaneous effective stress can be written as follows according to [101]:

$$\sigma_{eff} = \frac{1-D_0}{D^2(D-D_0)}\sigma_{mac} \quad (3)$$

where D_0 is the starting green density and σ_{mac} is the macroscopic applied pressure. In addition, the instantaneous shear modulus can be written as:

$$\mu_{eff} = \frac{E_{th}}{2(1+\nu_{eff})}\frac{D-D_0}{1-D_0} \quad (4)$$

where E_{th} is the effective Young's modulus and ν_{eff} is the effective Poisson's ratio. When the grain size is constant throughout the soak time during sintering, the equation can be transformed to:

$$\frac{1}{\mu_{eff}}\frac{1}{D}\frac{dD}{dt} = K_0\frac{e^{-\frac{Q_d}{RT}}}{T}\left(\frac{\sigma_{eff}}{\mu_{eff}}\right)^{n} \quad (5)$$

where Q_d is the activation energy and K_0 is a constant. Assuming one mechanism, the value of Q_d is a constant and the equation can finally be written in a form to determine the n value:

$$\ln\left(\frac{1}{\mu_{eff}}\frac{1}{D}\frac{dD}{dt}\right) = n * \ln\left(\frac{\sigma_{eff}}{\mu_{eff}}\right) + K_1 \quad (6)$$

where K_1 is a constant for a fixed soak temperature. Based on the stress exponent, the densification mechanism can be extracted. Possible densification mechanisms are listed in Table 6-3.

Table 6-3. Densification mechanisms and the corresponding stress and grain size exponents

Densification Mechanism	Stress Exponent (n)	Grain Size Exponent (p)
Viscous Flow	1	0
Lattice Diffusion	1	2
Grain Boundary Diffusion	1	3
Liquid Phase Sintering	1	3
Grain Boundary Sliding	1-2	1
Dislocation Induced Plasticity	≥ 3	0

The equation above was applied to sintering displacement data of an $Nd_2Ti_2O_7$ sample sintered to 1050°C during the hold time of 5 min with an applied pressure of 54 MPa. The slope of the corresponding line is about 0.4, which does not match up with any of the given *n* values (Figure 6-1). We are further testing to confirm the mechanism.

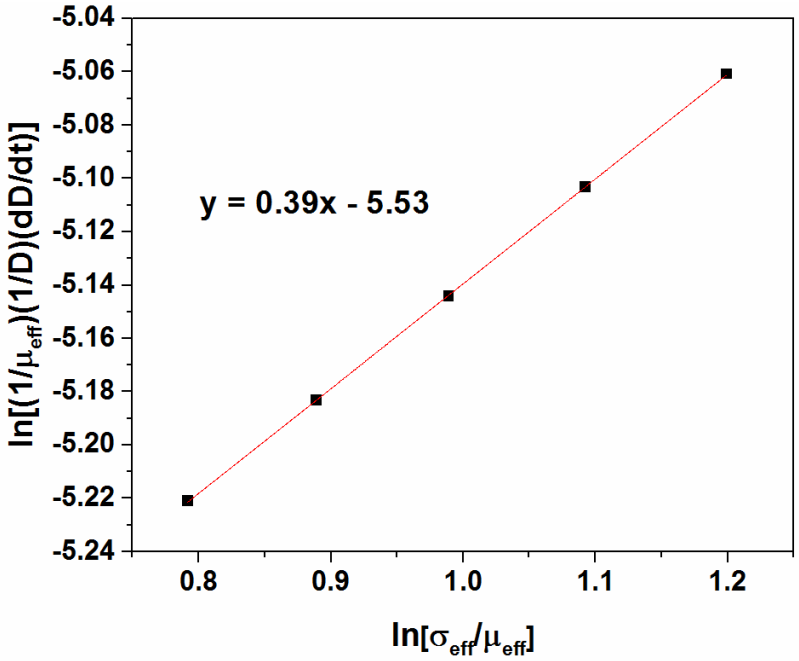

Figure 6-13. Effective stress exponent for Nd2Ti2O7 calculated for a sample sintered to 1050°C for 5 min

Ce-zirconolite and pyrochlore samples will be tested for stability under storage conditions. The radiation damage in samples will be simulated via ion implantation using Kr and He ions to simulate alpha recoils and alpha particles respectively. The experiments will be carried out at the Ion Beam Laboratory (IBL) at the University at Albany. The samples will be characterized with GIXRD and TEM to determine the radiation damage.

The chemical durability will be tested by subjecting 3 Ce-zirconolite and 3 Ce-pyrochlore samples to the PCT [102]. The leachates will be analyzed via inductively coupled plasma (ICP) for Ce release. The leaching mechanism will be investigated by subjecting monoliths of select compositions to testing via ASTM standard C1220 [103]. Monoliths will be suspended in water at 90°C for different lengths of time (1, 7, 28, and 42 days). The Ce leach rate can then be determined and the monoliths will be analyzed with GIXRD, SEM and EDS to determine the leaching mechanism.

7) Structural characterization and Cs retention of Ba-Cr hollandites (Task 5)

Our earlier studies [70] on Cs-substituted single-phase hollandites and the research done at SRNL [3] strongly indicated that barium hollandites with Cr^{3+} as a promising lattice for effective Cs retention. $Ba_{1.0}Cs_{0.3}Cr_{2.3}Ti_{5.7}O_{16}$ was observed to retain highest amount of Cs after PCT when compared to other

chemistries $Ba_{1.0}Cs_{0.3}M_{2.3}Ti_{5.7}O_{16}$ (*M*: Fe/Al) [3]. Also, (Ba,Cr)-hollandite could be easily formed, with no impurity phase, at lower temperatures [71]. This part of the project focusses on research to further analyze and validate $Ba_{1.15-x}Cs_{2x}Cr_{2.3}Ti_{5.7}O_{16}$ lattice as a potential Cs host. Series of compositions $Ba_{1.15-x}Cs_{2x}Cr_{2.3}Ti_{5.7}O_{16}$ with increased Cs loadings ($0 \leq x \leq 1.15$) have been prepared by sol-gel synthesis to determine Cs solubility. Structural parameters of different Cs-substituted hollandites are determined by powder XRD and neutron diffraction. Phase-pure compositions will subsequently be tested for Cs retention by PCT testing. The effects of structural parameters on Cs leachability, if any and the controlling factors for Cs retention will be investigated.

To obtain powders with homogeneous chemistry and minimum Cs losses, sol-gel method was chosen [84, 104]. Precursor materials and corresponding solutions used in this method are listed in Table 7-1. Solutions containing stoichiometric amounts of precursor solutes and corresponding solvents were mixed together resulting in a dark green solution with no agglomerates. Since the overall volume of the mixed precursor solution was high (~100ml/1g of required material), rotary evaporator is used to extract the solvent from the solution. The resultant homogeneous dry residue is used as precursor for further solid-state processing. Initial calcination of the as-obtained dry residue was done at 400˚C for 2h to remove all volatiles. Figure 7-1 shows the differential thermal analysis/thermogravimetric analysis (DTA/TGA) data of calcined powder for all compositions. Small exothermic event close to 900˚C (indicated in Figure 7-1(b)) is identified as the hollandite reaction temperature. Hence, calcined powders are further sintered at 1000˚C/3h to form hollandites.

TGA plots in Figure 7-1(a) show the corresponding weight loss at hollandite reaction temperature. In addition, the slopes weight loss curves at high temperatures show interesting features. At lower Cs levels ($x \leq 0.55$), the weight losses either tend to plateau or the slope of the curve is low. For compositions $x >$ 0.55, the slope is significantly higher implying the higher Cs loss from the material. This behavior can also be attributed to phase purity of the compositions as discussed below.

Table 7-1: Precursor materials used for sol-gel synthesis

Cation	**Precursor solution**	
	Solute	**Solvent**
Ba^{2+}	Barium acetate ($Ba(O_2H_3C_2)_2$)	Acetic acid
Cs^{+}	Cesium carbonate (Cs_2CO_3)	Acetic acid
Ti^{4+}	Titanium isopropoxide ($Ti(OC_3H_7)_4$)	Acetic acid + ethanol
Cr^{3+}	Chromium nitrate ($Cr(NO_3)_3.9H_2O$)	Isopropanol

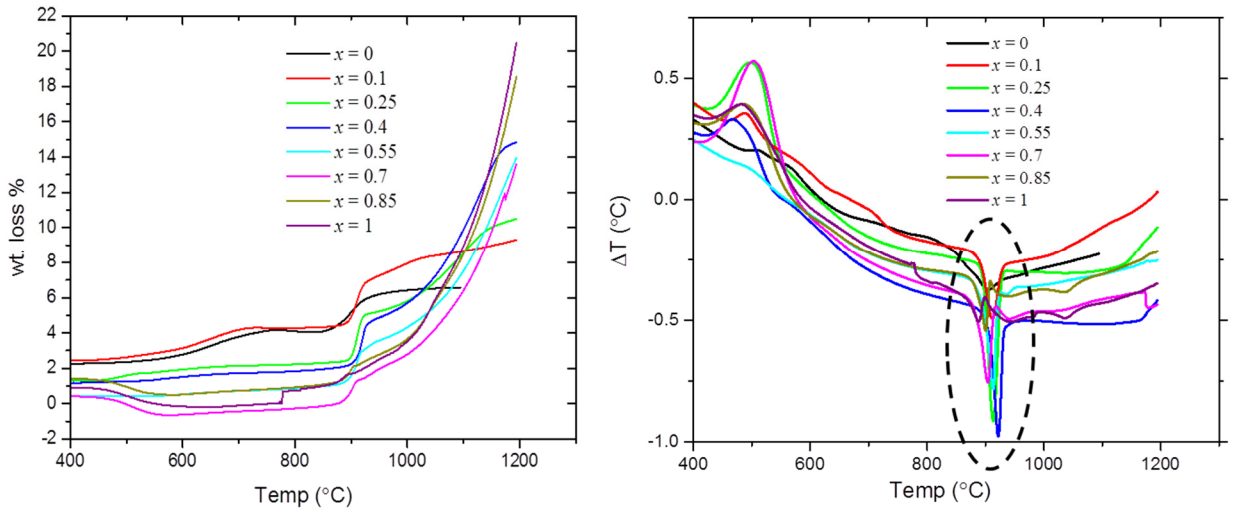

(a) (b)

Figure 7-1(a) TGA and (b) DTA plots for different compositions studied

Figure 7-2 compares the powder XRD patterns of the series of Cs-substituted hollandites. Phase-pure hollandite was observed for compositions $Ba_{1.15-x}Cs_{2x}Cr_{2.3}Ti_{5.7}O_{16}$ where $0 \leq x \leq 0.55$. Additional peaks appeared for compositions where more than 50% of Ba is substituted with Cs indicating that the maximum solubility of Cs in hollandite of $BaO\text{-}Cr_2O_3\text{-}TiO_2$ system is ~ 50%. Cross-sections of sintered pellets were observed using SEM. Back-scattered images showing the microstructural variations as a function of Cs loading are shown in Figure 7-3. Ba end member ($x = 0$) was observed to very fine equiaxed type of grain structure whereas the Cs end member ($x = 1.15$) had large rod-like grains. All intermediate compositions ($0 < x < 1.15$) had similar microstructures – elongated grains with a higher aspect ratio when compared to pure Ba hollandite. Preferential growth of hollandite was seen on substituting Ba with Cs in the compositions. No compositional contrast was observed in the back-scattered images for higher Cs compositions ($x > 0.55$) where powder XRD patterns differ from that of phase-pure hollandite. The results clearly indicate that the compositions with $x > 0.55$ adapted different structure or resulted in different phase(s). The slopes of TGA curves for compositions $x > 0.55$, as shown in Figure 7-1a, are relatively higher at high temperatures indicating increased Cs volatilization. This further suggests that the resultant phase(s) could not retain Cs and hence might not be pure hollandite. Since phase-pure hollandites are the focus of this study, compositions with $x > 0.55$ are not further studied.

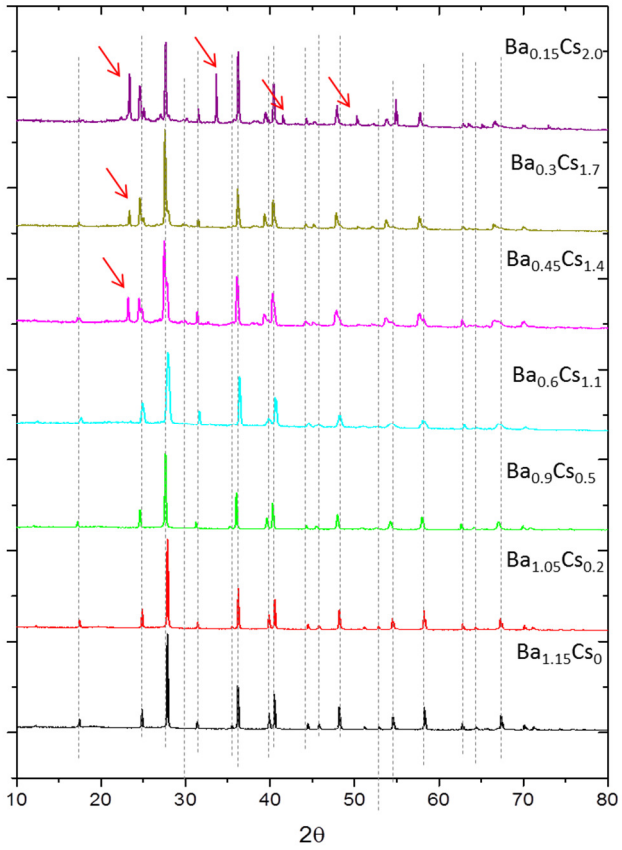

Figure 7-2: Powder XRD patterns of Ba1.15-xCs2xCr2.3Ti5.7O16. All dotted lines indicate peaks corresponding to hollandite phase. For x > 0.55, secondary peaks, labeled by red arrows, appeared.

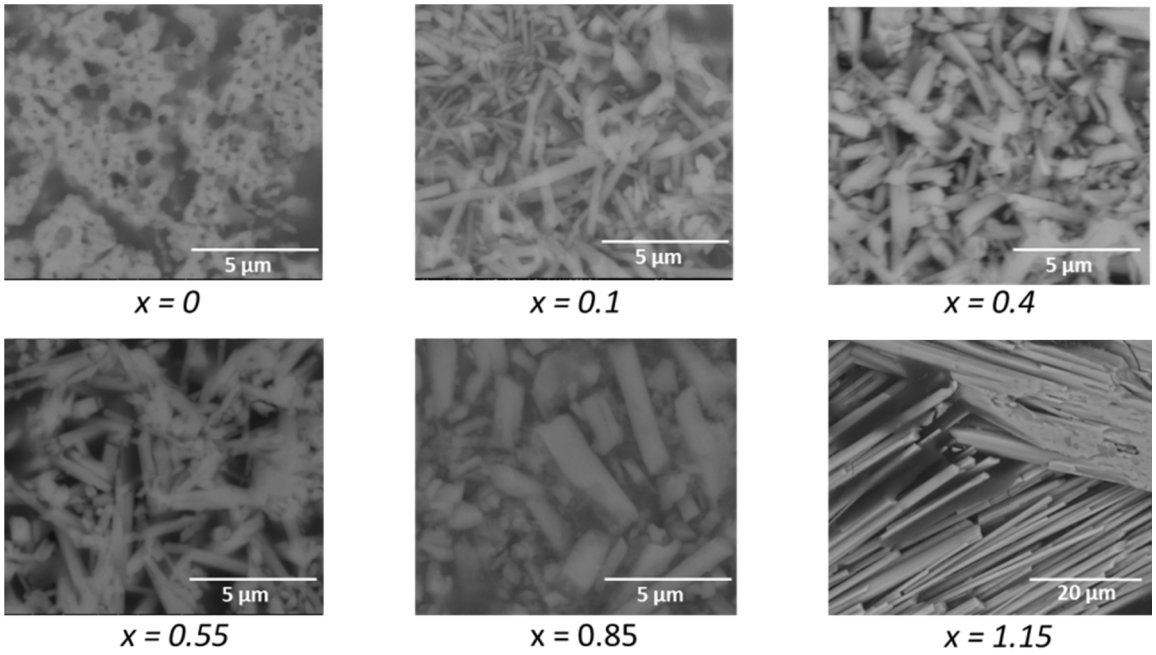

Figure 7-3: Back-scattered electron images of different compositions of Ba1.15-xCs2xCr2.3Ti5.7O16

7.1 Rietveld Analysis

Among different tetragonal (I4/m) and monoclinic (I2/m) models used for Rietveld refinement of powder XRD data, I2/m symmetry (PDF: 00-051-1900) yielded the best fit, in terms of 2θ peak positions and fit statistics, for all three compositions. Figure 7-4 shows a representative XRD refinement comparing the measured and calculated patterns. Although all peak positions are accounted for and the generated bond-lengths were found to be reasonable, there is a noticeable mismatch (weighted Rietveld parameter, R_{wp}: 12.7%) and the model is clearly inadequate to describe the unit cell.

As neutron scattering is more sensitive to oxygen sub-lattice than x-rays, neutron powder diffraction (NPD) data can help extract further structural information. For refinement of NPD data, corresponding I2/m structural models generated from XRD refinement were used as starting models. Figure 7-5 shows a standard I2/m hollandite unit cell with one tunnel site for Ba/Cs (*A* site), two distinct crystallographic octahedral sites for Cr/Ti (M_1 and M_2) and four distinct oxygen sites (O_1, O_2, O_3 and O_4). A typical refinement procedure is performed as follows. A Chebysvchev polynomial with 10 coefficients was used to describe the background and the peak profiles are described using a pseudo-Voight function. Occupancies/atomic positions are refined starting with strongest neutron scatterers to the weakest ones. All oxygen sites are assumed to have full occupancy and are only refined for positions followed by refinement of occupancies and positions of tunnel cation sites and octahedral sites (Figure 7-6). The sum of occupancies of Cr and Ti on each of the sites M_1 and M_2 is constrained to unity. Isotropic displacement parameters were applied for all sites except for Ba/Cs. Anisotropic displacement parameters (ADPs) were used for tunnel

cations to account for any disorder in their locations since they are located along one-dimensional tunnels in the structure.

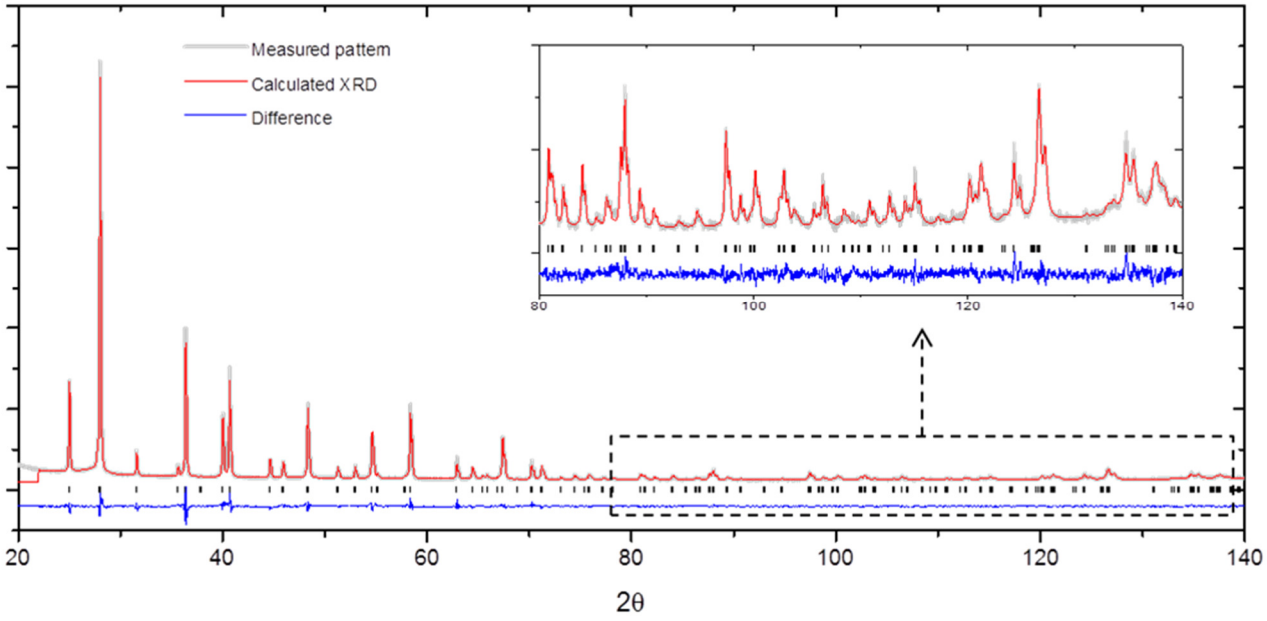

Figure 7-4: Rietveld refinement of powder XRD pattern for the composition Ba1.0Cs0.3Cr2.3Ti5.7O16.

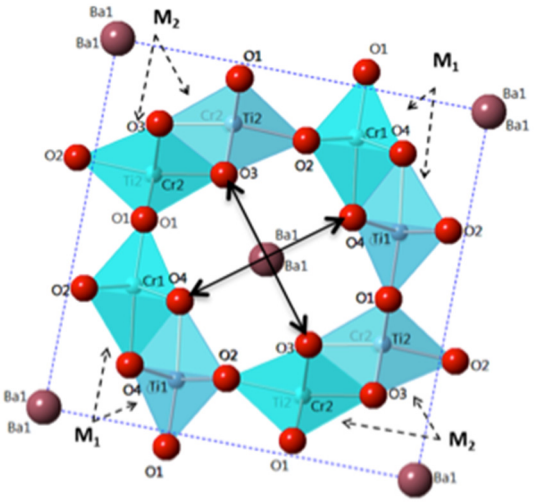

Figure 7-5: Hollandite unit cell with I2/m symmetry with all crystallographic sites labeled

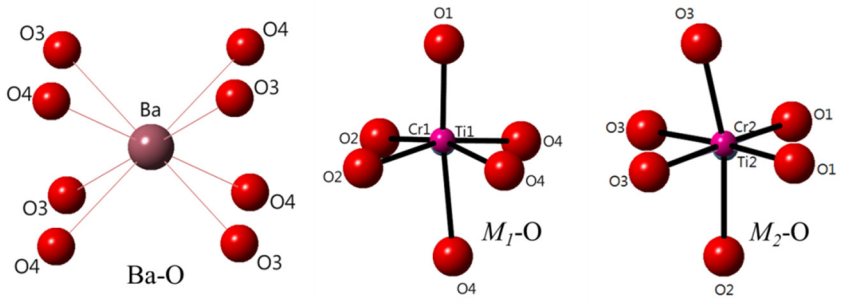

Figure 7-6. Illustrations of oxygen environments surrounding each cation site

Structure refinement of composition with no Cs was relatively straightforward and appropriate structural data was obtained, as discussed further. However, the initial refinement trials of Cs-substituted hollandites (x = 0.15 and 0.25) converged with unreasonably large e.s.ds (estimated standard deviations). Two adjustments needed to be done to get final structural models with realistic parameters and e.s.ds. Firstly, Ba was used as the only tunnel occupant. Considering similar neutron scattering lengths of Ba (5.1 fm) and Cs (5.4 fm), this is a rational assumption. The resultant refined compositions are presented in Table 7-2, and are primarily intended to show the increasing occupancy of the tunnels with x that further confirms that Cs is indeed taking the tunnel site in the lattice. Once this trend was established, refinements were performed for Cs compositions by constraining the Ba and Cs occupancies to the values measured by x-ray fluorescence. Secondly, the tunnel cations Ba and Cs were fixed at origin, (**x, y, z**) = (0, 0, 0). Since ADPs were used for tunnel cations, any disorder relative to the origin would be manifested in those values. Further remarks on this are discussed in Section 3.3.2. A typical NPD refinement with these considerations is shown in Figure 7-7.

Table 7-2: Comparison of target vs. refined compositions when only Ba was used as tunnel cation.

x	**Target composition**	**Refined composition**
0.0	$Ba_{1.15}Cr_{2.3}Ti_{5.7}O_{16}$	$Ba_{1.12}Cr_{2.2}Ti_{5.8}O_{16}$
0.15	$Ba_{1.0}Cs_{0.3}Cr_{2.3}Ti_{5.7}O_{16}$	$Ba_{1.18}Cr_{2.14}Ti_{5.86}O_{16}$
0.25	$Ba_{0.9}Cs_{0.5}Cr_{2.3}Ti_{5.7}O_{16}$	$Ba_{1.225}Cr_{2.08}Ti_{5.92}O_{16}$

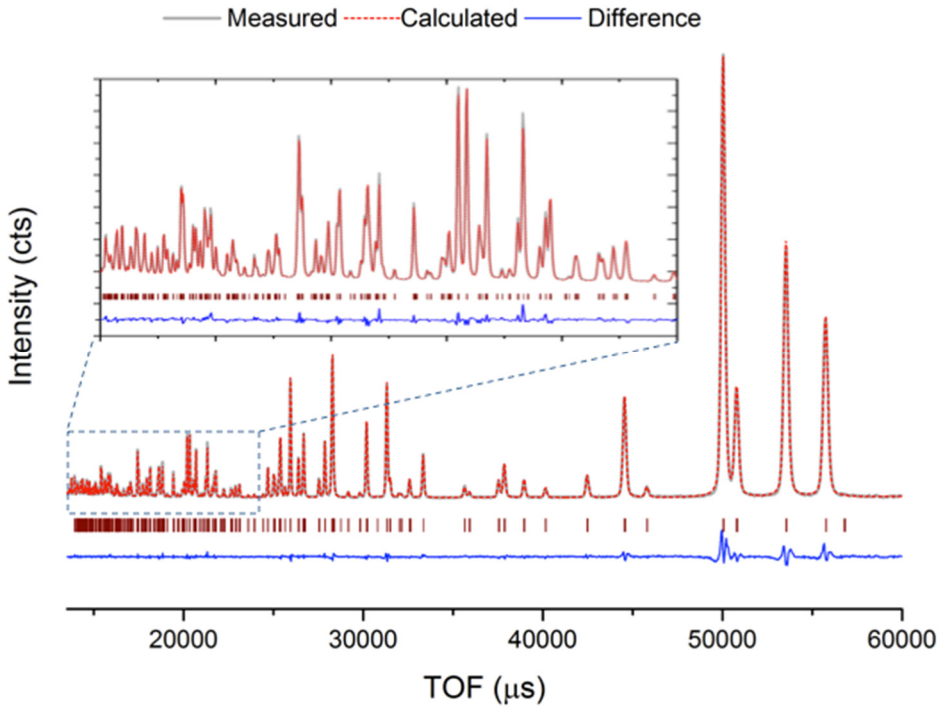

Figure 7-7. Rietveld refinement of NPD data for the composition $Ba_{1.0}Cs_{0.3}Cr_{2.3}Ti_{5.7}O_{16}$.

7.2 Structure of $Ba_{1.15-x}Cs_{2x}Cr_{2.3}Ti_{5.7}O_{16}$

The lattice parameters and fit parameters generated from NPD refinements are listed in Table 7-3. Except for the increase in the monoclinic nature (β), no specific trend was observed from the unit cell dimensions, *a*, *b* and *c*. In addition, the mean diagonal length of tunnel cross-section (*d*) reduced for lower Cs compositions but further increased at higher Cs loadings. This is counter intuitive to the idea that the tunnel/lattice parameters increase with the average size of the tunnel cations, and does not corroborate with other studies. We attribute this primarily to partial occupancy of tunnel sites. The fraction of vacant tunnel sites for compositions $x = 0$ and 0.15 are 42.5% and 35%, respectively. When Cs is introduced into the tunnel, the local expansion of the tunnel cavity is compensated by adjacent vacancies. Furthermore, the electrostatic attraction of Cs towards the oxygen ions surrounding the vacant sites would have intensified the shrinkage resulting in decreased lattice parameters.

The octahedral structural framework for all compositions was of typical monoclinic hollandite system, where only slight distortion from tetragonal symmetry would be observed, and the monoclinic nature (β) increased with the amount of Cs loading (Table 7-3). Final structural parameters for $Ba_{1.15}Cr_{2.3}Ti_{5.7}O_{16}$ are presented in Table 7-4 and selected bond lengths in Table 7-5. Assuming this as the base structure, the structural features and variations that reflect the effects of Cs loading in other compositions are discussed.

Table 7-3. Unit cell dimensions and fit parameters from Rietveld refinement of $Ba_{1.15-x}Cs_{2x}Cr_{2.3}Ti_{5.7}O_{16}$. R_{wp} is the weighted Rietveld parameter and χ^2 is the goodness-of-fit.

Composition		$x = 0$	$x = 0.15$	$x = 0.25$
Space group		I2/m	I2/m	I2/m
Unit cell parameters	*a, Å*	10.0847(3)	10.0244(6)	10.1917(13)
	b, Å	2.9590(1)	2.9333(2)	2.9776(4)
	c, Å	10.0746(3)	10.0075(6)	10.1590(13)
	β	90.032 (2)	90.058(2)	90.126(3)
	Volume, V, Å^3	300.627	298.953	303.343
	$d = (d_1 + d_2)/2$, Å	5.0965	5.0865	5.1790
Refinement parameters	R_{wp}, %	3.14	3.68	4.83
	χ^2	3.17	3.22	4.45

Table 7-4. Refined lattice parameters for the composition $Ba_{1.15}Cr_{2.3}Ti_{5.7}O_{16}$

		x	**y**	**z**	Occupancy	U_{iso}
	Ba^{2+}	0.0	0.0	0.0	0.563(20)	-
M_1	Ti^{4+}	0.329(2)	0.0	0.140(1)	0.755(14)	0.083(26)
	Cr^{3+}	0.330(6)	0.0	0.135(5)	0.245(14)	
M_2	Ti^{4+}	0.844(2)	0.0	0.337(1)	0.694(15)	0.032(50)
	Cr^{3+}	0.836(3)	0.0	0.335(2)	0.306(15)	
	O^{2-}	0.6625(2)	0.0	0.0410(2)	1	0.072(3)
	O^{2-}	0.0421(2)	0.0	0.3312(2)	1	0.077(5)
	O^{2-}	0.6533(2)	0.0	0.2995(2)	1	0.067(4)
	O^{2-}	0.2988(2)	0.0	0.3462(2)	1	0.074(6)

Table 7-5. Selected bond lengths obtained for the structure of Ba1.15Cr2.3Ti5.7O16. Different bond lengths listed below can be visualized from Figure 7-6.

Ba-O			M_1-O		M_2-O	
$Ba-O_3$	2.943	Equatorial	$Cr-O_2/Ti-O_2$	1.991/1.989	$Cr-O_3/Ti-O_3$	2.011/2.025
			$Cr-O_4/Ti-O_4$	1.979/1.967	$Cr-O_1/Ti-O_1$	1.934/1.920
$Ba-O_4$	2.950	Axial	$Cr-O_4/Ti-O_4$	2.153/2.095	$Cr-O_2/Ti-O_2$	2.074/1.999
			$Cr-O_1/Ti-O_1$	1.773/1.831	$Cr-O_3/Ti-O_3$	1.882/1.961

7.3 Framework Changes

Incorporation of Cs in the lattice was attained by redistribution of Ti and Cr on M_1 and M_2 sites and the corresponding octahedral distortions. For composition x=0, the ratio of Ti/Cr on M_1 site is clearly higher compared to that of M_2 (Table 7-4Table 7-4). On addition of Cs, the ratio decreases on M_1 site and increases on M_2 site i.e., part of Ti ions on M_1 site are substituted by Cr from M_2 site and vice-versa. Table 7-6 shows this trend. There is slight deviation in the refined total occupancy ratio Ti/Cr from the target values that is within the range of observed e.s.ds in all cases. All oxygen octahedra, $(Cr/Ti)O_6$, are severely distorted, as seen from different Cr/Ti-O bond lengths listed in Table 7-5. The effects of addition of Cs into the lattice are particularly seen on the octahedral axial bonds, M_1-O_1 and M_2-O_2, compared to equatorial bonds (Figure 7-6). Both M_1 and M_2 sites host Cr and Ti, which in turn have different lattice positions. Hence, the effects on individual bonds, Cr-O and Ti-O, could be examined on these sites. The corresponding bond lengths' comparison (Figure 7-8) shows that the Cr-O bond on either site has higher elongation compared to Ti-O bond. One of the characteristics of transition metal-oxygen octahedra is Jahn-Teller (JT) effect that could be linked to the overall octahedral distortion. To verify that the higher deformation of CrO_6 octahedra in our case is not due to JT effects, high-resolution x-ray photoelectron spectroscopy (XPS) experiments were performed on the powder samples. The XPS data confirmed the oxidation state of Cr as +3 in all compositions where the electronic configuration is not suitable to produce JT effects. The refinements hence indicate that addition of larger Cs preferentially stretches the Cr-O bond in the surrounding octahedra. This is further linked to the redistribution of Cr/Ti on M_1 and M_2 sites observed from the refined occupancies (Table 7-6). The refinements have stabilized the Cs containing structures by the enlargement of average M_1-O_1 and M_2-O_2 bonds, which necessitate adjusting the individual occupancies on M_1 and M_2.

Table 7-6. Occupancies of M1 and M2 sites showing the redistribution of Cr and Ti. Occupancies of Ba and Cs are constrained to the corresponding highlighted values.

x			x	y	z	Occupancy	U_{iso}
		Ba^{2+}/Cs^{+}	0.0	0.0	0.0	**0.50/0.15**	-
0.15	M_1	Ti^{4+}/Cr^{3+}	0.332(2)/0.336(4)	0.0	0.142(2)/0.137(5)	0.736/0.264	0.083(26)
	M_2	Ti^{4+}/Cr^{3+}	0.840(3)/0.830(2)	0.0	0.337(1)/0.334(2)	0.730/0.270	0.032(50)
		Ba^{2+}/Cs^{+}	0.0	0.0	0.0	**0.40/0.25**	-
0.25	M_1	Ti^{4+}/Cr^{3+}	0.332(21)/0.332(50)	0.0	0.147(20)/0.148(47)	0.714/0.286	0.083(26)
	M_2	Ti^{4+}/Cr^{3+}	0.826(4)/0.841 (2)	0.0	0.329(3)/0.333(1)	0.751/0.249	0.032(50)

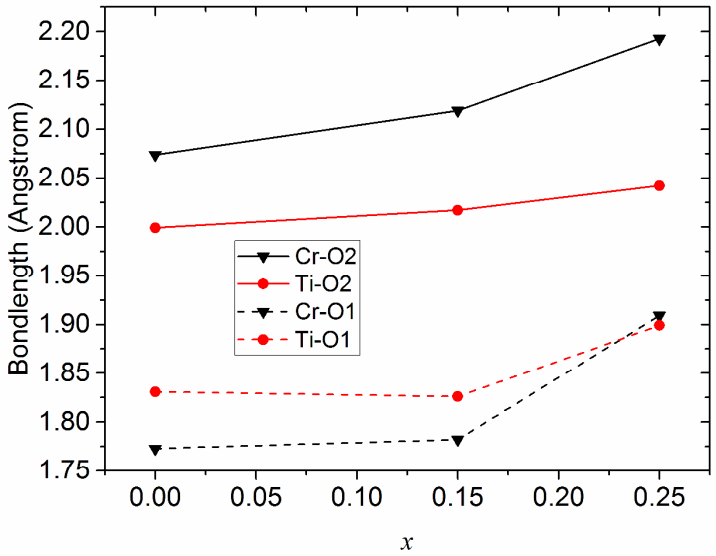

Figure 7-8. Variation of Cr-O and Ti-O bond lengths on M_1 (dotted line) and M_2 site (solid line). Error bars of all the data points are smaller than the corresponding data markers.

7.4 Tunnel Ion Order/Disorder

Table 7-7 shows the ADPs (U_{ij} - i,j = 1, 2, 3) obtained from the refinements. Compared to other components, U_{22} is significantly higher for all compositions. Large U_{22} denotes the uncertainty or disorder associated with the location of tunnel cation along the tunnel direction. This is illustrated in Figure 7-9, where the oblong ellipsoids represent the tunnel cation disorder. The presence of partially occupied tunnels giving rise to supercell structures has been mentioned in Section 1. In such cases, within each supercell, the tunnel ion sites relative to the corresponding

unit cells are not fixed. Hence, the high value of U_{22} component that represents the overall positional range within a supercell. In addition, a closer examination of the powder XRD patterns (Figure 7-10) reveals small diffuse satellite peaks at 2θ ~ 19.5˚. The formation of superstructures in Ba-hollandites is often evident from the presence of satellite reflections in XRD and electron diffraction patterns [64a-c,69]. Domains within the hollandite structure containing ordered tunnel cations/vacancies contribute to the diffuse reflections in XRD patterns [9]. Higher the degree of ordering, or larger the domain size, sharper are the satellite reflections. In the case of Cr-hollandites, with increasing Cs content, the satellite reflections tend to be more diffused (Figure 7-10). Substitution of one smaller Ba ($r_{Ba^{2+}}$ ~1.5$\dot{A}$) with two Cs ($r_{Cs^{+}}$ ~ 1.8$\dot{A}$) atoms may slow down the diffusion kinetics of Cs the tunnels resulting in relatively smaller degree of ordering. Collectively, the neutron and x-ray diffraction observations related to the positional order/disorder of Ba/Cs in the tunnel strongly suggest the presence of hollandite superstructures in our samples.

Table 7-7. Refined ADPs of tunnel cations, U12=U23=0 (by I2/m symmetry)

	U_{11}	U_{22}	U_{33}	U_{13}
$x = 0$	0.012(3)	**0.162(11)**	0.023(1)	-0.015(4)
$x = 0.15$	0.018(3)	**0.175(11)**	0.041(5)	-0.028(4)
$x = 0.25$	0.079(11)	**0.168(17)**	0.037(7)	0.052(7)

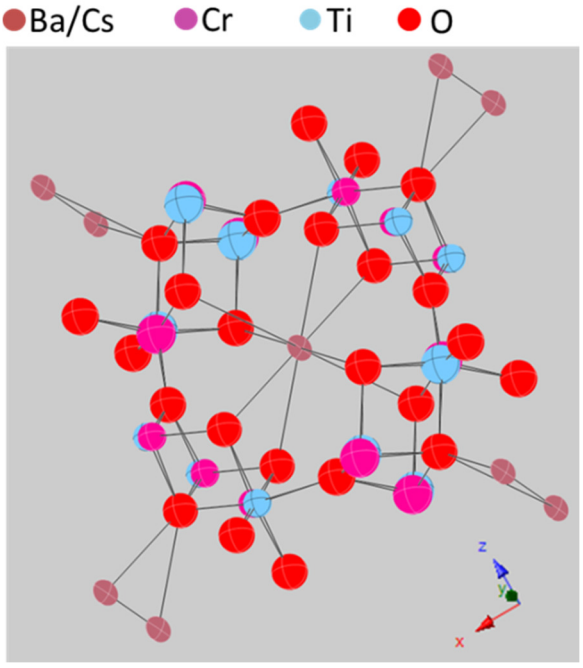

Figure 7-9. Elliptical thermal ellipsoids of tunnel sites show represent the large U_{22} displacement parameter for the composition $Ba_{1.15}Cr_{2.3}Ti_{5.7}O_{16}$

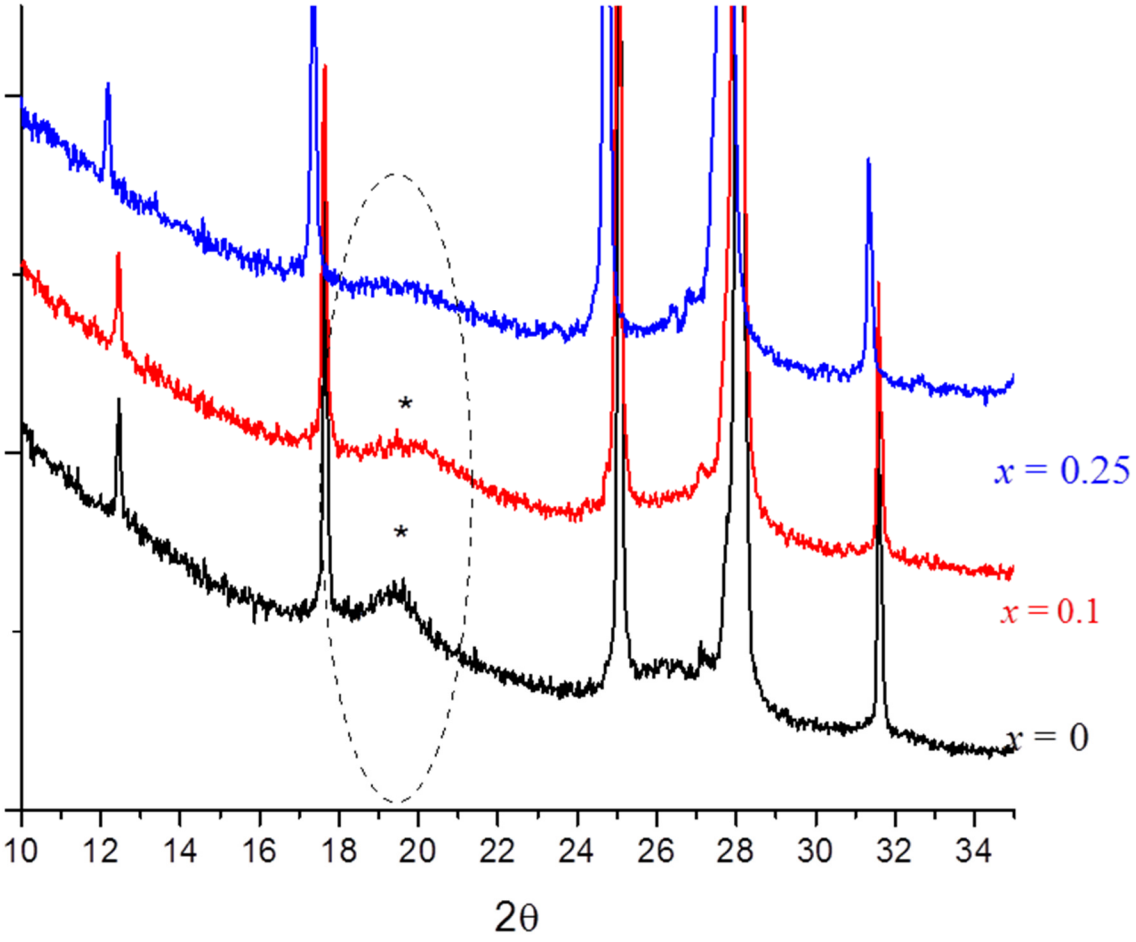

Figure 7-10. Powder XRD patterns showing the satellite reflections at low 2θ as indicated

7.5 Conclusion

The present study showed that in hollandite system $Ba_{1.15}Cr_{2.3}Ti_{5.7}O_{16}$, approximately ~35% of Ba can be replaced by Cs beyond which secondary phases were observed. Structural models of phase-pure compositions were developed by refinement of XRD and NPD data. Framework variations to accommodate Cs, relative to the base structure $Ba_{1.15}Cr_{2.3}Ti_{5.7}O_{16}$, are evident from the refined parameters and indicate that Cs sites are surrounded locally by CrO_6 octahedra. However, the overall superlattice structure is preserved as seen from the U_{22} parameters and with XRD satellite reflections.

8) References

[1] E. Vernaz, S. Gin, C. Veyer, in *Comprehensive Nuclear Materials*, DOI: http://dx.doi.org/10.1016/B978-0-08-056033-5.00107-5 (Ed: R. J. M. Konings), Elsevier, Oxford **2012**, p. 451.

[2] M. L. Carter, M. W. A. Stewart, S. H. F. Leung, M. Colella, E. R. Vance, *Ceramic Transactions* **1996**, 71, 491.

[3] J. Amoroso, J. Marra, S. D. Conradson, M. Tang, K. Brinkman, *Journal of Alloys and Compounds* **2014**, 584, 590.

[4] A. E. Osmanlioglu, *Waste Manage.* **2002**, 22, 481.

[5] a) G. R. Lumpkin, K. L. Smith, M. G. Blackford, *J. Nucl. Mater.* **1995**, 224, 31; b) T. Murakami, *Chem. Waste Man.* **1985**, 5, 269; c) A. E. Ringwood, S. E. Kesson, N. G. Ware, W. Hibberson, A. Major, *Nature* **1979**, 278, 219.

[6] a) A. L. Billings, K. Brinkman, K. M. Fox, J. C. Marra, M. Tang, K. E. Sickafus, *U.S. Department of Energy Report: FCRD-WAST-2010-000158, SRNL-STI-2010-00560* **2010**, Savannah River National Laboratory, Aiken, SC; b) K. Brinkman, K. M. Fox, M. Tang, *U.S. Department of Energy Report: FCRD-SWF-2011-000310, SRNL-STI-2011-00516* **2011**, Savannah River National Laboratory, Aiken, SC; c) K. Brinkman, K. Fox, J. C. Marra, M. Tang, *Report SRNL Technical Report SRNL-STI-2012-00281, FCRD-SWF-2012-000116* **2012**.

[7] M. L. Carter, E. R. Vance, H. Li, *Mater. Res. Soc. Symp. Proc.* **2003**, 807, 249.

[8] W. J. Buykx, D. M. Levins, R. S. Smart, K. L. Smith, G. T. Stevens, K. G. Watson, D. Weedon, T. J. White, *J. Am. Ceram. Soc.* **1990**, 73, 1201.

[9] V. Aubin-Chevaldonnet, D. Caurant, A. Dannoux, D. Gourier, T. Charpentier, L. Mazerolles, T. Advocat, *Journal of Nuclear Materials* **2007**, 366, 137.

[10] J. P. Guha, *J. Solid State Chem.* **1980**, 34, 17.

[11] C. J. Ball, J. L. Woolfrey, *J. Nucl. Mater.* **1983**, 118, 159.

[12] R. W. Cheary, J. Kwiatkowska, *J. Nucl. Mater.* **1984**, 125, 236.

[13] R. W. Cheary, *Mater. Sci. Forum* **1988**, 27/28, 397.

[14] M. L. Carter, *Mat. Res. Bull.* **2004**, 39, 1075.

[15] V. Aubin, D. Caurant, D. Gourier, N. Baffler, T. Advocat, F. Bart, G. Leturcq, J. M. Costantini, *MRS Proceedings* **2004**, 807, 315.

[16] M. L. Carter, R. L. Withers, *J. Solid State Chem.* **2005**, 178, 1903.

[17] A. Y. Leinekugel-le-Cocq, P. Deniard, S. Jobic, R. Cerny, F. Bart, H. Emerich, *J. Solid State Chem.* **2006**, 179, 3196.

[18] T. Suzuki-Muresan, J. Vandenborre, A. Abdelouas, B. Grambow, S. Utsunomiya, *J. Nucl. Mater.* **2011**, 419, 281.

[19] F. Angeli, P. McGlinn, P. Frugier, *J. Nucl. Mater.* **2008**, 380, 59.

[20] J. M. Montel, *Geoscience* **2011**, 343, 230.

[21] G. C. C. Costa, H. Xu, A. Navrotsky, *J. Am. Ceram. Soc.* **2013**, 96, 1554.

[22] a) M. M. Milanova, M. Kakihana, M. Arima, M. Yashima, M. Yoshimura, *J. Alloy. Compd.* **1996**, 242, 6; b) W. S. Kim, S. Ha, S. Yun, H. Park, *Thin Film Solids* **2002**, 420-421, 575; c) V. V. Atuchin, T. A. Gavrilova, J.-C. Grivel, V. G. Kesler, *Surface Science* **2008**, 602, 3095; d) Z. Shao, S. Saitzek, P. Roussel, M. Huve, R.Desfeux, O. Mentre, F. Abraham, *J. Cryst. Growth* **2009**, 311, 4134; e) R. V. Pai, S. K. Mukerjee, V.Venugopal, *Solid State Ionics* **2011**, 187, 85.

[23] K. B. Helean, S. V. Ushakov, C. E. Brown, A. Navrotsky, J. Lian, R. C. Ewing, J. M. Farmer, L. A. Boatner, *J. Solid State Chem.* **2004**, 177, 1858.

[24] J. Sloan, R. J. D. Tilley, *J. Solid State Chem.* **1996**, 121, 324.

[25] E. J. Harvey, K. R. Whittle, G. R. Lumpkin, R. I. Smith, S. A. T. Redfern, *J. Solid State Chem.* **2005**, 178, 800.

[26] W. Zhang, L. Zhang, H. Zhong, L. Lu, X. Yang, X. Wang, *Mater. Charact.* **2010**, 61, 154.

[27] K. B. Helean, A. Navrotsky, E. R. Vance, M. L. Carter, B. Ebbinghaus, O. Krikorian, J. Lian, L. M. Wang, J. G. Catalano, *Journal of Nuclear Materials* **2002**, 303, 226.

[28] D. M. Strachan, R. D. Scheele, E. C. Buck, J. P. Icenhower, A. E. Kozelisky, R. L. Sell, R. J. Elovich, W. C. Buchmiller, *J. Nucl. Mater.* **2005**, 345, 109.

[29] J. Lian, S. V. Yudintsev, S. V. Stefanovsky, L. M. Wang, R. C. Ewing, *Journal of Alloys and Compounds* **2007**, 444–445, 429.

[30] S. E. Kesson, W. J. Sinclair, A. E. Ringwood, *Nucl. Chem. Waste Man.* **1983**, 4, 259.

[31] E. R. Vance, B. D. Begg, R. A. Day, C. J. Ball, *MRS Proceedings* **1994**, 353, 767.

[32] B. D. Begg, E. R. Vance, S. D. Conradson, *Journal of Alloys and Compounds* **1998**, 271–273, 221.

[33] D. Caurant, P. Loiseau, I. Bardez, *Journal of Nuclear Materials* **2010**, 407, 88.

[34] a) D. Swenson, T. G. Nieh, J. H. Fournelle, *J. Am. Ceram. Soc.* **1998**, 81, 3249; b) D. Swenson, T. G. Nieh, J. H. Fournelle, *Mat. Res. Soc. Symp. Proc.* **1996**, 412, 337.

[35] E. R. Vance, D. J. Cassidy, C. J. Ball, G. J. Thorogood, *J. Nucl. Mater.* **1992**, 190, 295.

[36] a) R. Stevens, B. K. Hom, J. Boerio-Gates, B. F. Woodfield, R. L. Putnam, J. Gutierriez, A. Navrotsky, *J. Chem. Thermodyn.* **2001**, 33, 1441; b) H. Xu, Y. Wang, *J. Nucl. Mater.* **1999**, 275, 211; c) B. F. Woodfield, J. Boerio-Gates, J. L. Shapiro, R. L. Putnam, A. Navrotsky, *J. Chem. Thermodyn.* **1999**, 31, 245; d) R. L. Putnam, A. Navrotsky, B. F. Woodfield, J. Boerio-Gates, J. L. Shapiro, *J. Chem. Thermodyn.* **1999**, 31, 229.

[37] F. W. Clinard, D. L. Rohr, R. B. Roof, presented at Second International Conference on Radiation Effects in Insulators, Albuquerque, NM **1983**.

[38] K. L. Smith, N. J. Zaluzec, G. R. lumpkin, *J. Nucl. Mater.* **1997**, 250, 36.

[39] S. X. Wang, L. M. Wang, R. C. Ewing, G. S. Was, G. R. Lumpkin, *Nuclear Instruments and Methods in Physics Research Section B: Beam Interactions with Materials and Atoms* **1999**, 148, 704.

[40] C. Davoisne, M. C. Stennett, N. C. Hyatt, N. Peng, C. Jeynes, W. E. Lee, *Journal of Nuclear Materials* **2011**, 415, 67.

[41] G. Leturcq, P. J. McGlinn, C. Barbe, M. G. Blackford, K. S. Finnie, *Applied Geochemistry* **2005**, 20, 899.

[42] P. Poml, T. Geisler, J. Cobos-Sabate, T. Wiss, P. E. Raison, P. Schmid-Beurmann, X. Deschanels, C. Jegou, J. Heimink, A. Putnis, *J. Nucl. Mater.* **2011**, 410, 10.

[43] a) G. R. Lumpkin, K. L. Smith, M. G. Blackford, *J. Nucl. Mater.* **1995**, 224, 31; b) J. L. Woolfrey, K. D. Reeve, D. J. Cassidy, *J. Nucl. Mater.* **1982**, 108-109, 739.

[44] W. J. Buykx, D. J. Cassidy, C. E. Webb, J. L. Woolfrey, *Ceramic Bulletin* **1981**, 60, 1284.

[45] W. J. Buykx, *J. Nucl. Mater.* **1982**, 107, 78.

[46] W. Lutze, *Raioactive Waste Forms for the Future*, **1988**.

[47] A. Abdelouas, J. L. Crovisier, W. Lutze, B. Grambow, J. C. Dran, R. Muller, *J. Nucl. Mater.* **1997**, 240, 100.

[48] P. B. Rose, *Ph.D.* University of Sheffield, Sheffield, UK, **2008**.

[49] F. Bart, J. L. Dussossoy, C. Fillet, *Mater. Res. Soc. Symp. Proc.* **2001**, 663, 161.

[50] O. Menard, T. Advocat, J. P. Ambrosi, A. Michard, *Appl. Geochem.* **1998**, 13, 105.

[51] N. Henry, P. Deniard, S. Jobic, R. Brec, C. Fillet, F. Bart, A. Grandjean, O. Pinet, *J. Non-Cryst. Solids* **2004**, 333, 199.

[52] N. Chouard, D. Caurant, O. Majerus, J. L. Dussossoy, A. Ledieu, S. Peuget, R. Baddour-Hadjean, J. P. Pereira-Ramos, *J. Non-Cryst. Solids* **2011**, 357, 2752.

[53] G. Calas, M. L. Grand, L. Galoisy, D. Ghaleb, *J. Nucl. Mater.* **2003**, 322, 15.

[54] T. Hartmann, A. Alaniz, F. Poineau, P. F. Weck, J. A. Valdez, M. Tang, G. D. Jarvinen, K. R. Czerwinski, K. E. Sickafus, *J. Nucl. Mater.* **2011**, 411, 60.

[55] M. Tang, P. Fuierer, P. Dickens, *Phys. Stat. Sol.* **2013**, 10, 216.

[56] I. A. Sobolev, S. V. Stefanovsky, B. I. Omelianenko, S. V. Ioudintsev, E. R. Vance, A. Jostsons, *Mat. Res. Soc. Symp. Proc.* **1997**, 465, 371.

[57] S. Stefenovsky, A. G. Ptashkin, O. A. Knyazev, S. A. Dmitriev, S. V. Yudintsev, B. S. Nikono, *J. Alloy. Compd.* **2007**, 444, 438.

[58] M. Nygren, Z. Shen, in *Ceramics Science and Technology Vol. 3 Synthesis and Processing* (Eds: R. Riedel, I.-W. Chen), Wiley-VCH Verlag GmbH &Co. **2012**, Ch. 8, p. 189.

[59] B. M. Clark, P. Tumurugoti, S. K. Sundaram, J. W. Amoroso, J. C. Marra, K. S. Brinkman, *Metallurgical and Materials Transactions E* **2014**, 1, 341.

[60] P. Tumurugoti, B. M. Clark, D. J. Edwards, J. Amoroso, S. K. Sundaram, *Journal of Solid State Chemistry* **2017**, 246, 107.

[61] P. Tumurugoti, S. Sundaram, S. T. Misture, J. C. Marra, J. Amoroso, *Journal of Nuclear Materials* **2016**, 473, 178.

[62] R. W. Cheary, *Acta Crystallographica Section B: Structural Science* **1986**, 42, 229.

[63] a) M. De Graef, *Introduction to conventional transmission electron microscopy*, Cambridge University Press, **2003**; b) J. Van Landuyt, G. Van Tendeloo, S. Amelinckx, *Pure and Applied Chemistry* **1985**, 57, 1373.

[64] a) S. E. Kesson, T. J. White, *Proceedings of the Royal Society of London Series A* **1986**, 408, 295; b) M. L. Carter, R. L. Withers, *Journal of Solid State Chemistry* **2005**, 178, 1903; c) L. Bursill, G. Grzinic, *Acta Crystallographica Section B: Structural Science* **1980**, 36, 2902; d) L. Bursill, J. Kwiatkowska, *Journal of Solid State Chemistry* **1984**, 52, 45; e) F. Mijlhoff, D. Ijdo, H. Zandbergen, *Acta Crystallographica Section B: Structural Science* **1985**, 41, 98.

[65] a) D. M. Strachan, R. D. Scheele, E. C. Buck, A. E. Kozelisky, R. L. Sell, R. J. Elovich, W. C. Buchmiller, *Journal of Nuclear Materials* **2008**, 372, 16; b) E. Fanchon, J. Hodeau, J. Vicat, J. Watts, *Journal of Solid State Chemistry* **1991**, 92, 88.

[66] U. Kolb, K. Shankland, L. Meshi, A. Avilov, W. I. David, *Uniting Electron Crystallography and Powder Diffraction*, Springer, **2012**.

[67] a) V. Aubin-Chevaldonnet, D. Caurant, A. Dannoux, D. Gourier, T. Charpentier, L. Mazerolles, T. Advocat, *Journal of nuclear materials* **2007**, 366, 137; b) N. Sharma, J. Plevert, G. Subba Rao, B. Chowdari, T. White, *Chemistry of materials* **2005**, 17, 4700.

[68] A. Leinekugel-le-Cocq-Errien, P. Deniard, S. Jobic, E. Gautier, M. Evain, V. Aubin, F. Bart, *Journal of Solid State Chemistry* **2007**, 180, 322.

[69] a) R. Cheary, *Acta Crystallographica Section B: Structural Science* **1987**, 43, 28; b) R. W. Cheary, *Materials Science Forum* **1988**, 27, 397.

[70] P. Tumurugoti, S. K. Sundaram, K. S. Brinkman, J. W. Amoroso, K. M. Fox, *Ceramic Transactions* **2014**, 250, 205.

[71] W. J. Weber, R. C. Ewing, C. R. A. Catlow, T. D. Rubia, L. W. Hobbs, C. Kinoshita, H. Matzke, A. T. Motta, M. Nastasi, E. K. H. Salje, E. R. Vance, S. J. Zinkle, *J. Mater. Res.* **1998**, 13, 1434.

[72] J. Lian, L. M. Wang, R. C. Ewing, L. A. Boatner, *Nuclear Instruments and Methods in Physics Research Section B: Beam Interactions with Materials and Atoms* **2005**, 241, 365.

[73] M. Tang, A. Kossoy, G. Jarvinen, J. Crum, L. Turo, B. Riley, K. Brinkman, K. Fox, J. Amoroso, J. Marra, *Nuclear Instruments and Methods in Physics Research Section B: Beam Interactions with Materials and Atoms* **2014**, 326, 293.

[74] S. Thevuthasan, C. H. F. Peden, M. H. Engelhard, D. R. Baer, G. S. Herman, W. Jiang, Y. Liang, W. J. Weber, *Nuclear Instruments and Methods in Physics Research Section A: Accelerators, Spectrometers, Detectors and Associated Equipment* **1999**, 420, 81.

[75] R. C. Ewing, W. J. Weber, F. W. Clinard, *Progress In Nuclear Energy* **1995**, 29, 63.

[76] J. F. Ziegler, J. P. Biersack, U. Littmark, *The Stopping and Range of Ions in Matter*, Pergamon Press, New York **1985**.

[77] M. Tang, P. Tumurugoti, B. Clark, S. K. Sundaram, J. Amoroso, J. Marra, C. Sun, P. Lu, Y. Wang, Y. B. Jiang, *Journal of Solid State Chemistry* **2016**, 239, 58.

[78] K. Jin, Y. Zhang, H. Xue, Z. Zhu, W. J. Weber, *Nuclear Instruments and Methods in Physics Research Section B: Beam Interactions with Materials and Atoms* **2013**, 307, 65.

[79] a) ASTM, Vol. C1285-14, 2014; b) J. Amoroso, J. C. Marra, M. Tang, Y. Lin, F. Chen, D. Su, K. S. Brinkman, *Journal of Nuclear Materials* **2014**, 454, 12; c) K. Brinkman, K. Fox, J. Marra, J. Reppert, J. Crum, M. Tang, *Journal of Alloys and Compounds* **2013**, 551, 136.

[80] a) Y. Teng, S. Wang, Y. Huang, K. Zhang, *Journal of the European Ceramic Society* **2014**, 34, 985; b) D. M. Strachan, *Nuclear and Chemical Waste Management* **1983**, 4, 177; c) S. V. Stefanovsky, S. V. Yudintsev, S. A. Perevalov, I. V. Startseva, G. A. Varlakova, *Journal of Alloys and Compounds* **2007**, 444–445, 618.

[81] a) ASTM, Vol. C1663-09, 2009; b) C. Martin, I. Ribet, P. Frugier, S. Gin, *Journal of Nuclear Materials* **2007**, 366, 277; c) W. L. Gong, L. M. Wang, R. C. Ewing, E. Vernaz, J. K. Bates, W. L. Ebert, *Journal of Nuclear Materials* **1998**, 254, 249.

[82] S. E. Kesson, *Radioact. Waste Manage. Environ. Restor.* **1983**, 4, 53.

[83] D. K. Pham, S. Myhra, P. S. Turner, *J. Mater. Res.* **1994**, 9, 3174.

[84] F. Angeli, P. McGlinn, P. Frugier, *Journal of Nuclear Materials* **2008**, 380, 59.

[85] H. Xu, G. C. Costa, C. R. Stanek, A. Navrotsky, *J. Am. Ceram. Soc.* **2015**, 98, 255.

[86] K. Zhang, G. Wen, H. Zhang, Y. Teng, *Journal of the European Ceramic Society* **2015**, 35, 3085.

[87] C. W. Bjorklund, *J. Am. Chem. Soc.* **1957**, 79, 6347.

[88] a) J. C. Marra, A. D. Cozzi, R. A. Pierce, J. M. Pareiza, A. R. Jurgensen, D. M. Missimer, 2001; b) M. V. Zamoryanskaya, B. E. Burakov, *Mat. Res. Soc. Symp. Proc.* **2000**, 663, 301.

[89] B. D. Begg, E. R. Vance, *Mat. Res. Soc. Symp. Proc.* **1997**, 465, 333.

[90] H. J. Rossell, *J. Solid State Chem.* **1992**, 99, 52.

[91] A. A. Coelho, R. W. Cheary, K. L. Smith, *Journal of Solid State Chemistry* **1997**, 129, 346.

[92] X. Deschanels, A. M. Seydoux-Guillaume, V. Magnin, A. Mesbah, M. Tribet, M. P. Moloney, Y. Serruys, S. Peuget, *Journal of Nuclear Materials* **2014**, 448, 184.

[93] B. D. Begg, E. R. Vance, B. A. Hunter, J. V. Hanna, *Journal of Materials Research* **1998**, 13, 3181.

[94] K. L. Smith, G. R. Lumpkin, M. G. Blackford, R. A. Day, K. P. Hart, *Journal of Nuclear Materials* **1992**, 190, 287.

[95] a) M. Pirzada, R. W. Grimes, L. Minervini, J. F. Maguire, K. E. Sickafus, *Solid State Ionics* **2001**, 140, 201; b) L. Minervini, R. W. Grimes, Y. Tabira, R. L. Withers, K. E. Sickafus, *Phil. Mag. A* **2002**, 82, 123; c) P. J. Wilde, C. R. A. Catlow, *Solid State Ionics* **1998**, 112, 173.

[96] J. D. Gale, Version 3.4.

[97] N. F. Mott, M. J. Littleton, *Trans. Faraday Soc.* **1938**, 34, 485.

[98] L. Veiller, J.-P. Crocombette, D. Ghaleb, *J. Nucl. Mater.* **2002**, 306, 61.

[99] N. Ishizawa, K. Ninomiya, T. Sakakura, J. Wang, *Acta Cryst,* **2013**, E69, i19.

[100] G. Bernard-Granger, C. Guizard, *Acta Materialia* **2007**, 55, 3493.

[101] A. S. Helle, K. E. Easterling, M. F. Ashby, *Acta Metallurgica* **1985**, 33, 2163.

[102] A. C1285-14, Vol. C1285-14, 2014.

[103] A. C1220-10, Vol. C1220-10, 2010.

[104] H. Xu, L. Wu, J. Zhu, A. Navrotsky, *Journal of Nuclear Materials* **2015**, 459, 70.